博士論文

題目　Electronic structure of layered chalcogenide superconductors with orbital instability

(軌道不安定性を有する層状カルコゲナイド超伝導体の電子構造)

氏名　　杉本 拓也

DEPARTMENT OF COMPLEXITY SCIENCE AND ENGINEERING,
GRADUATE SCHOOL OF FRONTIER SCIENCES,
UNIVERSITY OF TOKYO

Electronic structure of layered chalcogenide superconductors with orbital instability

Takuya Sugimoto

A THESIS SUBMITTED IN ACCORDANCE
WITH THE REQUIREMENTS FOR THE DEGREE OF
DOCTOR OF PHILOSOPHY IN PHYSICS

DECEMBER 2016

ASSESSMENT COMMITTEE:

Visiting Professor Ryotaro Arita
First-principles Materials Science Research Team, RIKEN
Department of Complexity Science and Engineering, University of Tokyo

Professor Takashi Mizokawa
Department of Applied Physics, Waseda University

Project Associate Professor Kozo Okazaki
Institute for Solid State Physics, University of Tokyo

Professor Koichiro Saiki
Department of Complexity Science and Engineering, University of Tokyo

Professor Takehiko Sasaki
Department of Complexity Science and Engineering, University of Tokyo

"Poets say science takes away from the beauty of the stars - mere globs of gas atoms. I too can see the stars on a desert night, and feel them. But do I see less or more?"

Rechard P. Feynman

ACKNOWLEDGEMENTS

It is a great pleasure and honor for me to express my deep regards and special gratitude to the people who have supported the research during my PhD.

First, I would like to express my cordial gratitude to my academic supervisor, Prof. Takashi Mizokawa, who kindly accepted me to join his great research group as a graduate student. I am greatly thankful to him for giving me the opportunity to investigate many interesting systems including Fe-based and BiS_2-based superconductors, for giving me a lot of chances to go overseas for my research, and for continuous support.

Di tutte le persone importanti coinvolte nella mia tesi, sono particolarmente grato al Prof. Naurang Lal Saini di Universitá di Roma "*La Sapienza*", l'Italia. Da quando ho visitato per la prima volta La Sapienza nel 2013, lui mi ha introdotto al mondo dell' EXAFS, spieghandomi l'importanza dell'ordine/disordine su scala locale che è legato alla struttura elettronica. Vorrei anche ringraziare lui per avermi accettato come ricercatore in visita per un anno e mezzo durante il mio dottorato di ricerca. Non solo dal punto di vista della fisica, ma anche per la sua disponibilita nell'organizzazione dei miei viaggi a Roma. Inoltre, vorrei ringraziarlo per la sua grande ospitalità verso me e la mia famiglia durante la mia ultima visita.

I would like to express my gratitude as well to Prof. Kozo Okazaki of ISSP, University of Tokyo, for accepting me as a member of his group due to the transfer of my academic supervisor to Waseda University.

My cordial gratitude also goes to Dr. Daiki Ootsuki, a former member of Mizokawa group (currently Assistant Professor at Kyoto University), for continuous and encouraging support from my bachelor to doctorate degree over the past five years. I am deeply thankful to him for teaching me the experimental and theoretical methods for the research.

Il mio grande apprezzamento va anche al signor Eugenio Paris, un dottorando del Prof. Saini alla Sapienza, per avermi aiutato molto nella comprensione della tecnica EXAFS e per le proficue discussioni sul nostro tema di ricerca comune, i sistemi BiS_2. Abbiamo condiviso molti bei momenti a Roma, Giove, Trieste, Grenoble, Ginevra, Hiroshima, Kyoto e Tokyo per attività di ricerca e non solo. Vorrei ringraziare gli altri membri passati e presenti del suo gruppo di ricerca; Sig.

Yasin Hacisalihoglu, Dott. Antonella Iadecola, Dott. Boby Joseph e Dott. Markus Bendele per il supporto sperimentale e le fruttuose discussioni.

I would like to thank our secretaries; Ms. Ayako Fukuya, Ms. Sachiko Shinei, and Ms. Yoshie Kaneko, who always kindly help the documents, arrangements of my business trips, and taking charge of my budget for research provided by Japan Society for the Promotion of Science (JSPS).

I am thankful to the following people for the experimental support in Elettra, Syncrotone Trieste, Italy; Dr. Gulliana Aquilanti at XAFS beamline, and to Dr. Alexey Barinov and Mr. Viktor Kandyba at Spectromicroscopy beamline.

I am grateful to the following people for the the experimental support during our beamtime at European Synchrotron Radiation Facility; Dr. Murielle Salome at ID21, Dr. Olivier Mathon and Dr. Virginia Montesegruro at BM23, Dr. Eduardo Salas Colera, Dr. Aida Serrano Rubio, and Dr. Germàn R. Castro at BM25A, Dr. Dipanjan Banerjee and Dr. Alessandro Longo at BM26A, and Dr. Olivier Proux at BM30B.

I would like to thank Dr. Laura Simonelli and Dr. Carlo Marini of ALBA synchrotron in Barcelona for their experimental support at ESRF.

My appreciation also extends to Assistant Prof. Eike Fabian Schwier, Assistant Prof. Hideaki Iwasawa (currently Associate Beamline Scientist at Diamond Light Source, UK), and Prof. Kenya Shimada not only for the experimental support at BL-1 and laser-ARPES apparatus, Hiroshima Synchrotron Radiation Center, Hiroshima University, but also for the fruitful discussion and constructive/valuable comments on our manuscripts. I would like to deeply thank technical specialist Dr. Masashi Arita for the experimental support and detailed beamline-setups for us at BL-9A, Hiroshima Synchrotron Radiation Center, Hiroshima University.

I am greatly thankful to Assistant Prof. Takashi Noji and Prof. Yoji Koike of Tohoku Univeristy for providing us the high quality single crystals of Fe(Se,Te) and valuable comments on our manuscript.

I am deeply thankful to Mr. Joe Kajitani, Assistant Prof. Ryuji Higashinaka, Associate Prof. Tatsuma D. Matsuda, and Prof. Yuji Aoki of Tokyo Metropolitan University for providing us high-quality single crystals of BiS_2-based systems and for fruitful discussion on them. I would also like to thank Prof. Yoshikazu Mizuguchi of Tokyo Metropolitan University and Prof. Yoshihiko Takano of National Institute for Materials Science for providing us the high-quality polycrystalline RE(O,F)BiS_2 (RE=Ce, Nd, Sm) and fruitful discussion on the BiS_2-based systems.

I am indebted to Assistant Prof. Hidetomo Usui and Prof. Kazuhiro Kuroki of Osaka University for fruitful discussion on the orbital states of the BiS_2-based superconductors, and providing us the calculated orbital distribution of the Fermi surfaces using the minimal model at underdoped region.

I would like to thank Dr. Corentin Morice (currently Institut de Physique Théorique, CEA, Université Paris-Saclay), Prof. Emilio Artacho, and Prof. Siddharth S. Sax-

ena of the Cavendish Laboratory, Cambridge University, for fruitful discussion and providing us the *ab initio* calculation data of $CeO_{0.5}F_{0.5}BiS_2$.

My warmest thanks go to all the current and former members of Mizokawa group and some of Fujimori group, University of Tokyo; Mr. Makoto Fukuzawa, Ms. Miyoko Oiwake, Mr. Songfun Lee, Mr. Masafumi Horio, Mr. Yukio Takahashi, Mr. Kei Sawada, Mr. Tomohiro Noda, Mr. Yuichi Yokoyama. I had a great time with all of them during our study and in other activities.

I am deeply thankful to Prof. Tomohiko Saitoh of Tokyo Unviersity of Science for introducing me to the great world of solid state physics and photoemission spectroscopy when I was an undergraduate student. He had been giving me patient guidance and valuable, helpful, and encouraging advice not only through physics but also for my life.

I would like to acknowledge the support from JSPS research fellowship DC1 for both research budget and economical support during my PhD.

Last but not least, I send my sincere and deepest thanks with respect and gratitude to my family; my wife, daughter, father, mother, and brother for their continuous support, encouragement, and giving me this great opportunity and environment to study physics over the years.

Roma, dicembre MMXVI
Tak Sugimoto

LIST OF ABBREVIATIONS

AFM ..... antiferromagnetic or antiferromagnetism

ARPES ..... angle-resolved photoemission spectroscopy

BCS ..... Bardeen-Cooper-Schrieffer

BEC ..... Bose-Einstein condensation

DFT ..... density functional theory

EDC ..... energy distribution curve

EXAFS ..... extended x-ray absorption fine structure

FM ..... ferromagnetic or ferromagnetism

GGA ..... generalized gradient approximations

LDA ..... local density approximation

MDC ..... momentum distribution curve

PES ..... photoemission spectroscopy

PM ..... paramagnetic or paramagnetism

XANES ..... x-ray absorption near edge structure

XAS ..... x-ray absorption spectroscopy

CONTENTS

1

INTRODUCTION

We start with the introduction to the superconductivity from its historical progress including unconventional superconductors, and briefly take a look at basic properties of Fe-based and BiS_2-based systems. Overview of this thesis is also written in the end of this chapter.

1.1 Historical progress

Band theory

Wilson [1] and Bloch [2] had developed band theory, which explains why some materials behave like metallic and others insulating. In the band theory, electrons are treated as non-interacting particles by replacing all the interactions among electrons using one mean-field, *i.e.*, the many-body problem is reduced into a one-electron problem. Electrons are expressed by so-called Bloch electron. When the number of electron in a unit cell is odd (even) , the material is always metallic (insulator) within a scheme of the band theory since the band is partially (fully) occupied. Band theory is widely used from model calculation (such as tight-binding calculation) to first-principles. However, Boer and Verwey pointed out that the band theory does not work for a large number of insulating $3d$ transition metal compounds [3].

Discovery of superconductivity

In 1908, Heike Kamerlingh Onnes, a Dutch physicist, had firstly succeeded in liquefaction of helium gas. The history of superconductivity had begun in 1911 with the discovery of the sudden reduction to zero-resistivity of mercury below 4.2 K [4] using the liquid helium.

In 1957, Bardeen, Cooper, and Schrieffer proposed the first microscopic theory of superconductivity (so-called BCS theory), which described that superconductivity is caused by a condensation of Cooper pairs (electrons are paired in momentum space and becomes boson-like state) [5]. They received the Nobel Prize in Physics for this theory in 1972. The ground state is given by the superposition of normal electrons and Cooper pairs:

$$|\Psi^{\mathrm{BCS}}\rangle = \prod_k (u_k + v_k c^\dagger_{k\uparrow} c_{-k\downarrow})|0\rangle. \tag{1.1}$$

where $u_k = |u_k|$ and $v_k = |v_k|e^{i\phi}$, and they satisfy $|u_k|^2 + |v_k|^2 = 1$. In other words, all the pairs are added with the same phase; U(1) gauge symmetry is broken. The materials which can be explained by BCS theory (k-independent gap structure, s-wave pairing) are so called conventional superconductors.

Strong correlation and discovery of high-T_c cuperate

Where there is a strong correlation such as strong on-site Coulomb interaction, the internal degrees of freedom of electron appears, namely, spin, orbital, and charge degrees of freedom. Mott and Hubbard attributed the insulating behavior of some compounds to the electron-electron interaction, and it is called Mott insulator [6, 7]. Anderson meanwhile introduced superexchange interaction in a model with

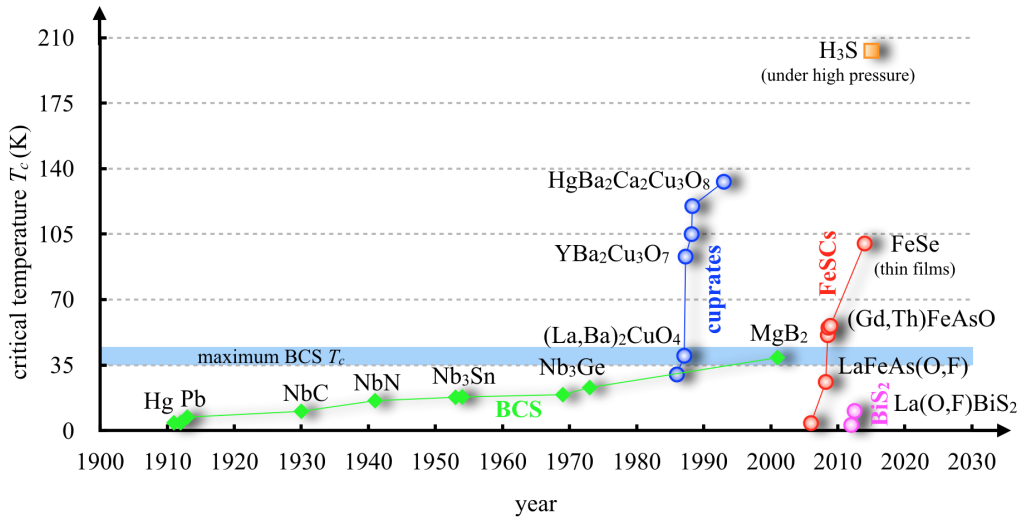

Figure 1.1: Historical progress of the transition temperature to the superconducting state (T_c) of some groups of materials; conventional BCS superconductors, cuprates, Fe-based superconductors (FeSCs), BiS_2-based superconductors, and H_3S.

the large d-d Coulomb interaction of localized d electrons, which is caused by the energy lowering via hopping [8, 9].

In 1986, J. Georg Bednorz and K. Alex Müller found that perovskite Cu oxide showed $T_c = 35$ K [10], and this finding followed an intensive research on Cu oxide superconductors (cuprates) including $HgBa_2Ca_2Cu_3O_8$ that showed $T_c = 133$ K. These high T_c cuprates are also classified in strongly correlated systems, and those phenomena could not be explained by the BCS theory; The gap structure is no more k-independent, and has $d_{x^2-y^2}$ symmetry. Anderson introduced a famous RBV state for the understanding of the cuprates [11]. The other approach was the AFM fluctuation [12, 13]. The hole-doped system is described by Zhang-Rice singlet [14], which is the starting point of t-J model [15].

1.2 Fe-based and BiS_2-based superconductors

In 2008, the first pnictide iron-based superconductor La(O,F)FeAs with $T_c = 26$ K was discovered by Hosono group [16]. Just several months after the discovery, T_c of 56 K was achieved in (Gd,Th)FeAsO [17], and the maximum T_c above 100 K was reported in FeSe thin films in 2014 [18].

Meanwhile, Mizuguchi *et al.* reported a new layered superconductors $Bi_4O_4S_3$ [19] and $La(O,F)BiS_2$ [20] in 2012. The crystal structure of latter system is quite similar to the La(O,F)FeAs system; instead of electronically active FeAs layers, BiS_2 layers are responsible for the conductivity.

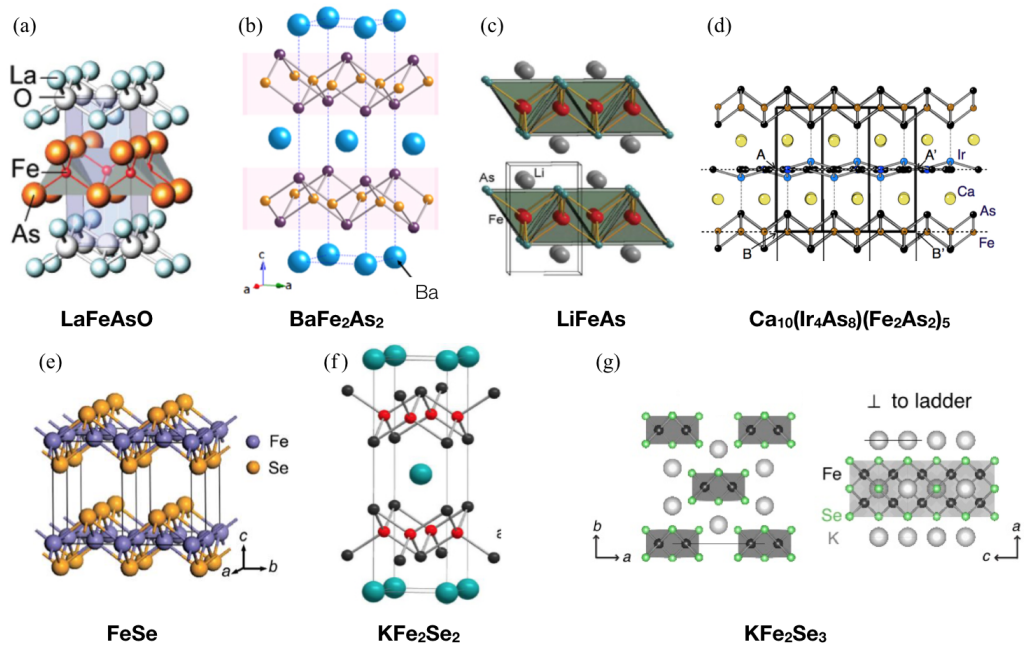

Figure 1.2: Crystal structures of Fe pnictides; (a) LaFeAsO, (b) $BaFe_2As_2$, (c) LiFeAs, and (d) $Ca_{10}(Ir_4As_8)(Fe_2As_2)_5$ and of Fe chalcogenides; (e) FeSe, (f) KFe_2Se_2, and (g) KFe_2Se_3.

Both Fe-based and BiS_2-based superconductors have layered structure. In a typical Fe-based system, the electronically active FeAs or FeSe layers are sandwiched by block layers whereas in a typical BiS_2-based system, the electronically active BiS_2 layers are sandwiched by block layers as well. The crystal structures of Fe-based and BiS_2-based superconductors are shown in Figs. 1.2 and 1.3, respectively.

1.3 Overview: structure of this thesis

In this thesis, Fe-based and BiS_2-based superconductors are investigated. The common physics besides the crystal structures are orbital instability and spin-orbit interaction, and they are explained in chapter 2. We studied these systems using model calculations, PES, and XAS experiments. Principles of calculations and experiments are explained in chapter 3 and 4, respectively. The detailed experimental setups are described in chapter 5. Finally, experimental and calculated results on Fe-based and BiS_2-based materials are shown in chapter 6 and 7, respectively. Each section has short abstract and small conclusion in chapter 6 and 7. Concluding

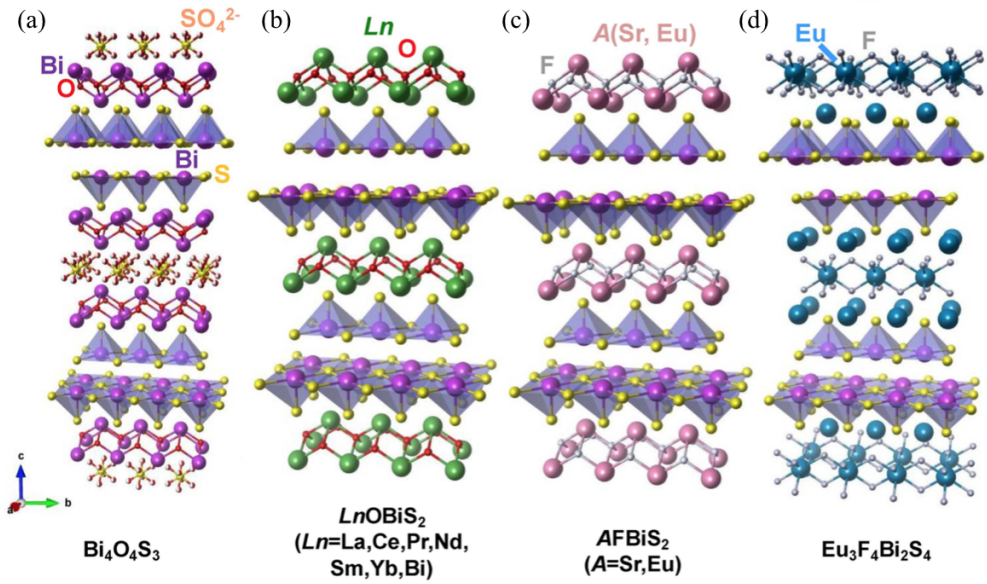

Figure 1.3: Crystal structures of BiS_2-based compounds; (a) $Bi_4O_4(SO_4)_{1-x}Bi_2S_4$ with $x = 0.5$, (b) LnOBiS$_2$ (Ln = La, Ce, Pr, Nd, Sm, Yb, and Bi), (c) AFBiS$_2$ (A = Sr, Eu), and (d) $Eu_3F_4Bi_2S_4$.

remarks of this thesis is finally summarized in chapter 8.

2

BACKGROUND AND MOTIVATION

We will take a look at characteristic features of the Fe-based and BiS_2-based superconductors; orbital instability and spin-orbit interaction, from brief introduction with toy models.

2.1 Orbital instability

Treatment and role of the orbital degrees of freedom

When internal degrees of freedom in electrons, spin and orbital degrees of freedom, become tangible, they have a large impact on physical properties of solids. Orbital degrees of freedom can be expressed by pseudo-spin operator; it can be treated like spin, and orbital and spin can be treated in parallel. As the spin shows phase transition with long-range order, orbital degrees of freedom also shows 'orders' of some sort, so-called orbital order. Let us introduce an example of two-orbital Hubbard Hamiltonian;

$$\begin{aligned}\mathscr{H} =& -t\sum_{\langle ij\rangle}\sum_{\sigma,\alpha=1,2}[c^\dagger_{i\sigma\alpha}c_{j\sigma\alpha}+\text{h.c.}]+u\sum_{i,\alpha}n_{i\alpha\uparrow}n_{i\alpha\downarrow}+u'\sum_{i,\alpha>\beta}n_{i\alpha}n_{i\beta}\\ &+j\sum_{i,\alpha>\beta}\sum_{\sigma,\sigma'}c^\dagger_{i\alpha\sigma}c_{i\beta\sigma}c^\dagger_{i\beta\sigma'}c_{i\alpha\sigma'}+j'\sum_{i,\alpha\neq\beta}c^\dagger_{i\alpha\uparrow}c_{i\beta\uparrow}c^\dagger_{i\alpha\downarrow}c_{i\beta\downarrow}\end{aligned} \tag{2.1}$$

where the parameters u, u', j, and j' are the Kanamori parameters, and the orbitals α and β are degenerate; four-fold degeneracy including spins. When the electron density is 1, take the kinetic term as a non-perturbed Hamiltonian, and the second-order perturbation can bring us the effective Hamiltonian as

$$\begin{aligned}\mathscr{H}^{\text{eff}} =& j_1\sum_{\langle ij\rangle}[\boldsymbol{s}_i\cdot\boldsymbol{s}_j+\frac{3}{4}][\boldsymbol{\tau}_i\cdot\boldsymbol{\tau}_j-\frac{1}{4}]+j_2\sum_{\langle ij\rangle}[\boldsymbol{s}_i\cdot\boldsymbol{s}_j-\frac{1}{4}][2\tau^y_i\cdot\tau^y_j+\frac{1}{2}]\\ &+j_3\sum_{\langle ij\rangle}[\boldsymbol{s}_i\cdot\boldsymbol{s}_j-\frac{1}{4}][\boldsymbol{\tau}_i\cdot\boldsymbol{\tau}_j+2\tau^y_i\cdot\tau^y_j+\frac{1}{4}]\end{aligned} \tag{2.2}$$

where the spin and pseudo-spin operators were defined by

$$\boldsymbol{s}_i=\frac{1}{2}\sum_{\alpha=1,2}\sum_{\sigma\sigma'}c^\dagger_{i\alpha\sigma}\sigma_{\sigma\sigma'}c_{i\alpha\sigma'},\quad \boldsymbol{\tau}_i=\frac{1}{2}\sum_{\alpha=1,2}\sum_{\sigma}c^\dagger_{i\alpha\sigma}\sigma_{\alpha\beta}c_{i\beta\sigma} \tag{2.3}$$

and the coefficients were described using $J=4t^2/u$ and $x=j/u$ as

$$j_1=\frac{J}{1-3x},\quad j_2=\frac{J}{1-x},\quad j_3=\frac{J}{1+x}. \tag{2.4}$$

Note that this perturbation is in the strong-correlation limit. From the effective Hamiltonian in Eq. (2.2), one can see that (ferro-spin,antiferro-orbital) or (antiferro-spin,ferro-orbital) pairs are energetically favorable. Moreover, the spin-spin correlation has SU(2) symmetry while the SU(2) is broken for the orbital-orbital correlation. Those concepts, also in the strong-correlation limit, were generalized by Kugel and Khomskii [21].

The orbital degrees of freedom is the freedom that orbital can occupy in spatially anisotropic wave functions. Therefore, the orbital order means that the specific

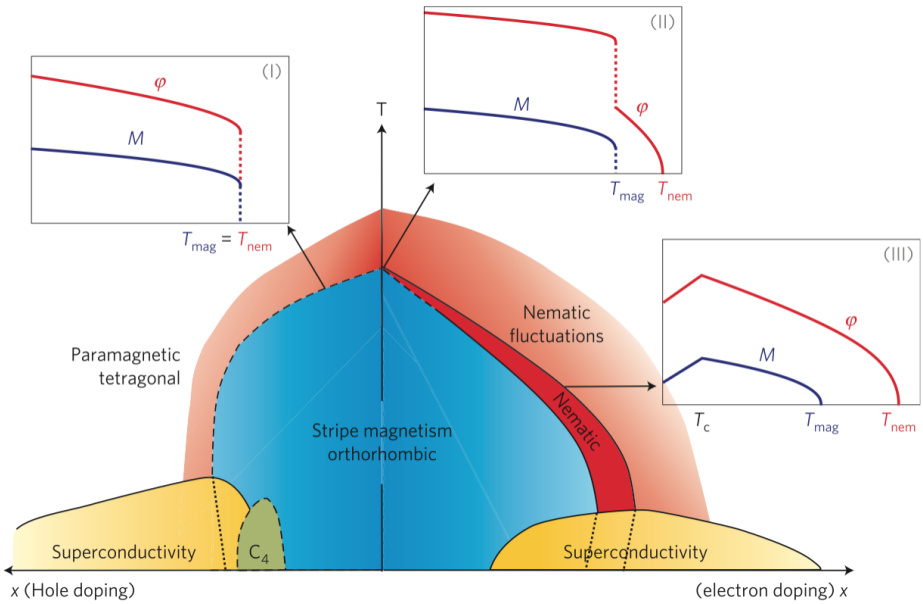

Figure 2.1: Schematic diagram of Fe-based pnictide $BaFe_2As_2$ family. Insets show the temperature dependence of magnetic and nematic order parameters (M and φ, respectively) [22].

wave function(s) regularly aligns. The anisotropic arrangement of wave functions directly affects on the properties of solids, *e.g.*, chemical bonds, conductivity, etc. The orbital order generally makes systems anisotropic electronically, and sometimes it reduces the effective dimensionality.

Orbital fluctuation

When superconducting state occurs, electrons are paired by exchanging bosons. In the BCS model, it is required that the matrix element of the potential $V_{kk'}$ is approximated by $-V$ near E_F and $V_{kk'} = 0$ for all the other energy eigenstates, and the boson is considered as phonon [23]. In unconventional superconductors, it is still controversial but instead of phonon, spin and/or orbital fluctuation can give rise to the superconducting state since in their phase diagram the superconducting state is next to the magnetic ordering state or orbital ordering state. Moreover, those fluctuation has higher energy scale compared with phonons, and therefore there are possibilities to induce higher critical transition temperature.

Orbital instability

Where there is an ordered phase, instability generally exists above the ordered phase. Note that the concepts of instability and fluctuation are different since there is always an ordered phase when the instability exists in a system (*e.g.* structural

instability, Fermi surface instability, etc.). In case of orbital, system can become stable states lowering the energy by resolving the orbital degeneracy, *i.e.*, orbital order. For instance, the Fe-based $BaFe_2As_2$ family shows a nematic phase as in the phase diagram shown in Fig. 2.1, namely, the system has an orbital instability.

The Fe-based and BiS_2-based superconductors have the orbital instability of Fe $3d\ yz/zx$ and Bi $6p_x/6p_y$ near E_F, respectively.

2.2 Spin-orbit interaction

The spin-orbit interaction, also called spin-orbit effect or spin-orbit coupling, is a relativistic interaction of an electron's spin with its orbital motion; the orbital degrees of freedom directly related to this interaction.

Since this interaction is relativistic, it is naturally introduced using Dirac equation [24, 25] by taking the non-relativistic limit. Time-dependent Dirac equation is given by

$$(i\hbar\partial\!\!\!/ - mc)\psi = 0. \tag{2.5}$$

We will take the non-relativistic limit under the stationary states and therefore one can re-write the Dirac equation with a potential $V = -Ze^2/r$ as

$$(c\boldsymbol{\alpha}\cdot\boldsymbol{P} + \beta mc^2 + V)|\psi\rangle = \varepsilon|\psi\rangle \tag{2.6}$$

where the spinor $|\psi\rangle$ is $|\psi\rangle = (\chi, \Phi)^T$. Then the Dirac equation becomes

$$\begin{bmatrix} \varepsilon - V - mc^2 & -c\boldsymbol{\sigma}\cdot\boldsymbol{P} \\ -c\boldsymbol{\sigma}\cdot\boldsymbol{P} & \varepsilon - V + mc^2 \end{bmatrix} \begin{bmatrix} \chi \\ \Phi \end{bmatrix} = \begin{bmatrix} 0 \\ 0 \end{bmatrix}, \tag{2.7}$$

and eliminating Φ follows

$$(\varepsilon - V - mc^2)\chi = c\boldsymbol{\sigma}\cdot\boldsymbol{P}[\frac{1}{\varepsilon - V + mc^2}]c\boldsymbol{\sigma}\cdot\boldsymbol{P}\chi. \tag{2.8}$$

Let us introduce non-relativistic energy to the first order as $\varepsilon_{\mathrm{NR}}^{(1)} = \varepsilon - mc^2$. Taking non-relativistic approximation of Eq. (2.8) to the first order as

$$\begin{aligned} \frac{1}{\varepsilon - V + mc^2} = \frac{1}{2mc^2 + \varepsilon_{\mathrm{NR}}^{(1)} - V} &= \frac{1}{2mc^2}(1 + \frac{\varepsilon_{\mathrm{NR}}^{(1)} - V}{2mc^2})^{-1} \\ &\approx \frac{1}{2mc^2}(1 - \frac{\varepsilon_{\mathrm{NR}}^{(1)} - V}{2mc^2}), \end{aligned} \tag{2.9}$$

then Eq. (2.8) becomes

$$[\frac{P^2}{2m} + V - \frac{\boldsymbol{\sigma}\cdot\boldsymbol{P}(\varepsilon_{\mathrm{NR}}^{(1)} - V)\boldsymbol{\sigma}\cdot\boldsymbol{P}}{4m^2c^2}]\chi = \varepsilon_{\mathrm{NR}}^{(1)}\chi. \tag{2.10}$$

One can expand LHS as follows in order to get rid of $\varepsilon_{\text{NR}}^{(1)}$;

$$\begin{aligned}(\varepsilon_{\text{NR}}^{(1)} - V)\boldsymbol{\sigma}\cdot\boldsymbol{P}\chi &= \boldsymbol{\sigma}\cdot\boldsymbol{P}(\varepsilon_{\text{NR}}^{(1)} - V) + \boldsymbol{\sigma}\cdot[\varepsilon_{\text{NR}}^{(1)} - V, \boldsymbol{P}]\chi \\ &= (\boldsymbol{\sigma}\cdot\boldsymbol{P})\frac{P^2}{2m}\chi + \boldsymbol{\sigma}\cdot[\boldsymbol{P}, V]\chi. \end{aligned} \tag{2.11}$$

Then we obtain

$$\begin{aligned}\varepsilon_{\text{NR}}^{(1)}\cdot\chi &= [\frac{P^2}{2m} + V - \frac{P^4}{8m^3c^2} - \frac{(\boldsymbol{\sigma}\cdot\boldsymbol{P})\cdot(\boldsymbol{\sigma}\cdot[\boldsymbol{P}, V])}{4m^2c^2}]\cdot\chi \\ &= [\frac{P^2}{2m} + V - \frac{P^4}{8m^3c^2} - \frac{i\boldsymbol{\sigma}\cdot\boldsymbol{P}\times[\boldsymbol{P}, V]}{4m^2c^2} - \frac{\boldsymbol{P}\cdot[\boldsymbol{P}, V]}{4m^2c^2}]\cdot\chi. \end{aligned} \tag{2.12}$$

The commutation relation $[\boldsymbol{P}, V]$ can be calculated as

$$\begin{aligned}[\boldsymbol{P}, V]|\phi\rangle &= (i\hbar\nabla\frac{Ze^2}{r} - \frac{Ze^2}{r}i\hbar\nabla)|\phi\rangle \\ &= i\hbar e^2[(\nabla\frac{1}{r})|\phi\rangle + \frac{1}{r}\nabla|\phi\rangle - \frac{1}{r}\nabla|\phi\rangle] = -i\hbar e^2\frac{\boldsymbol{r}}{r^3}|\phi\rangle \end{aligned} \tag{2.13}$$

and therefore the fourth term of Eq. (2.12) is

$$-\frac{i\boldsymbol{\sigma}\cdot\boldsymbol{P}\times[\boldsymbol{P}, V]}{4m^2c^2} = \frac{Ze^2}{2m^2c^2r^3}(\frac{\hbar}{2}\boldsymbol{\sigma})\cdot(\boldsymbol{r}\times\boldsymbol{P}) = \frac{Ze^2}{2m^2c^2r^3}\boldsymbol{S}\cdot\boldsymbol{L}. \tag{2.14}$$

Finally Eq. (2.12) becomes

$$\begin{aligned}\varepsilon_{\text{NR}}^{(1)}\cdot\chi &= [\frac{P^2}{2m} + V - \frac{P^4}{8m^3c^2} + \frac{1}{2m^2c^2}\frac{Ze^2}{r^3}\boldsymbol{S}\cdot\boldsymbol{L} + \frac{\hbar^2Ze^2}{8m^2c^2}\cdot 4\pi\delta(\boldsymbol{r})]\cdot\chi \\ &= [\mathscr{H}_{\text{NR}}^{(0)} + \mathscr{H}_{\text{MV}} + \mathscr{H}_{\text{SO}} + \mathscr{H}_{\text{D}}]\cdot\chi \end{aligned} \tag{2.15}$$

where $\mathscr{H}_{\text{NR}}^{(0)} = (P^2/2m) + V$, $\mathscr{H}_{\text{MV}}$ is the mass-velocity correction, $\mathscr{H}_{\text{SO}}$ is the spin-orbit interaction, and $\mathscr{H}_{\text{D}}$ is the Darwinian term. Note that if we approximate just up to zeroth order, Eq. (2.8) becomes Schrödinger equation.

When we take $\mathscr{H}_{\text{SO}}$ as perturbed Hamiltonian, spin and orbital operators are no longer good quantum numbers while the total angular momentum $\boldsymbol{J}$ is a good quantum number. The dot product $\boldsymbol{S}\cdot\boldsymbol{L}$ can be expressed as

$$\boldsymbol{S}\cdot\boldsymbol{L} = \frac{1}{2}[\boldsymbol{J}^2 - \boldsymbol{S}^2 - \boldsymbol{L}^2] \tag{2.16}$$

and therefore the states will be split into $J = L + (1/2)$ and $J = L - (1/2)$ if degenerate. The larger the angular momentum L is (*e.g.* heavy elements), the larger this splitting will be. Not only resolving the degeneracies, but also this interaction plays an important role, for instance, in topological insulators [26–28], heavy elements such as iridates [29, 30], spin-anisotropic system such as Ru oxides [31], and etc.

3

PRINCIPLE OF CALCULATIONS

In this chapter, we briefly take a look at methods of model calculations (unrestricted Hartree-Fock calculation and Anderson's impurity model calculation) as well as the first-principles.

3.1 Unrestricted Hartree-Fock approximation

In a scheme of restricted Hartree-Fock (HF) approximation, the expected values of the number of electron ($\langle d^\dagger_{m\sigma} d_{m\sigma}\rangle$ where m and σ denote orbital and spin) is the same for $\sigma =\uparrow$ and $\sigma =\downarrow$ sites. Besides, if there is an orbital degeneracy, $\langle d^\dagger_{m\sigma} d_{m\sigma}\rangle$ is the same for all m. In other words, $\langle d^\dagger_{m\sigma} d_{m\sigma}\rangle$ is restricted at the same value as long as electrons are in the same orbital (or the degenerate orbital).

On the other hand, unrestricted Hartree-Fock approximation removes this restriction, where the name *unrestricted* is come from. Since the unrestricted Hartree-Fock approximation has the spin/orbital degrees of freedom, electrons can occupy differently in the same orbital of spin up and down sites. The unrestricted Hartree-Fock approximation therefore allows antiferromagnetic solutions. Since the exchange interaction can be precisely taken into account, the unrestricted Hartree-Fock calculation enables to obtain a solution like Mott insulator in a broad sense. Note that the number of electron here does not have to be odd, and it can be considered as a Mott insulator as long as the system has a strong on-site Coulomb interaction, which opens its band gap.

3.1.1 Model Hamiltonian: multi-orbital *d*-*p* type Hamiltonian

In valence bands of Fe-based superconductors, there are electrons in Fe d-orbitals and chalcogen p-orbitals. Therefore, it is reasonable to take these electrons in a model. The model is called multi-orbital d-p type Hamiltonian where full degeneracy of the Fe d orbitals and chalcogen p orbitals is taken into account. The Hamiltonian consists of p-electron term, d-electron term, and p-d hopping term. The specific form of the Hamiltonian is as follows.

$$
\begin{aligned}
\hat{\mathscr{H}} =& \hat{\mathscr{H}}_p + \hat{\mathscr{H}}_d + \hat{\mathscr{H}}_{pd} \qquad (3.1)\\
\hat{\mathscr{H}}_p =& \sum_{kl\sigma} \epsilon^p_k p^\dagger_{kl\sigma} p_{kl\sigma} + \sum_{kll'\sigma} (V^{pp}_{kll'} p^\dagger_{kl\sigma} p_{kl'\sigma} + \text{h.c.})\\
\hat{\mathscr{H}}_d =& \epsilon^0_d \sum_{i\alpha m\sigma} d^\dagger_{i\alpha m\sigma} d_{i\alpha m\sigma} + \sum_{i\alpha mm'\sigma\sigma'} h_{mm'\sigma\sigma'} d^\dagger_{i\alpha m\sigma} d_{i\alpha m'\sigma'}\\
&+ u \sum_{i\alpha m} d^\dagger_{i\alpha m\uparrow} d_{i\alpha m\uparrow} d^\dagger_{i\alpha m\downarrow} d_{i\alpha m\downarrow} + u' \sum_{i\alpha mm'} d^\dagger_{i\alpha m\uparrow} d_{i\alpha m\uparrow} d^\dagger_{i\alpha m'\downarrow} d_{i\alpha m'\downarrow}\\
&+ (u' - j) \sum_{i\alpha mm'\sigma} d^\dagger_{i\alpha m\sigma} d_{i\alpha m\sigma} d^\dagger_{i\alpha m'\sigma} d_{i\alpha m'\sigma}\\
&+ j \sum_{i\alpha mm'} d^\dagger_{i\alpha m\uparrow} d_{i\alpha m'\uparrow} d^\dagger_{i\alpha m'\downarrow} d_{i\alpha m\downarrow} + j' \sum_{i\alpha mm'} d^\dagger_{i\alpha m\uparrow} d_{i\alpha m'\uparrow} d^\dagger_{i\alpha m\downarrow} d_{i\alpha m'\downarrow}\\
\hat{\mathscr{H}}_{pd} =& \sum_{kml\sigma} (V^{pd}_{kml} d^\dagger_{km\sigma} p_{kl\sigma} + \text{h.c.})
\end{aligned}
$$

Here, $d^\dagger_{i\alpha m\sigma}$ are creation operators for the Fe d electrons at site α of the ith unit cell,

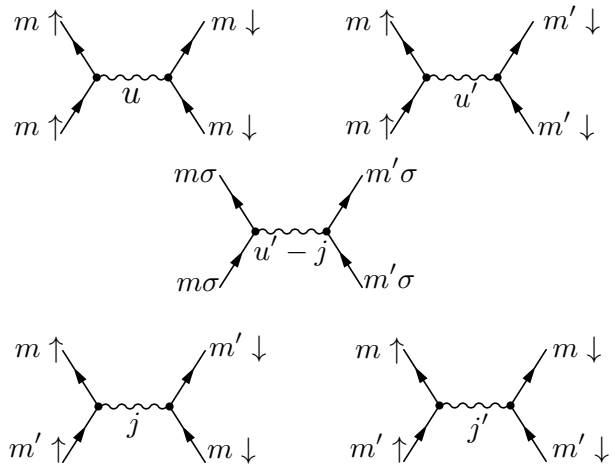

Figure 3.1: Diagrammatic representation of Kanamori parameters.

$d^\dagger_{km\sigma}$ and $p^\dagger_{kl\sigma}$ are creation operators for Bloch electrons constructed from the mth component of the d orbitals and from the lth component of the chalcogen p orbitals, respectively, with wave vector $\boldsymbol{k}$, and h.c. denotes the Hermitian conjugate. The matrix $h_{mm'\sigma\sigma'}$ denotes the spin-orbit interaction and the effects of crystal field splitting. The transfer integrals between the chalcogen p orbitals $V^{pp}_{kll'}$ are given by Slater-Koster parameters $(pp\sigma)$ and $(pp\pi)$. The transfer integrals between the Fe d and chalcogen p orbitals V^{pd}_{kml} are represented by $(pd\pi)$ and $(pd\sigma)$. The transfer integrals are scaled by Harrison's rule [32]. The parameters u, u', j, and j' are Kanamori parameters [33], and their diagrammatic representation is shown in Fig. 3.1. The charge-transfer energy Δ is defined by $\epsilon_d - \epsilon_p + nU$, where ϵ_d and ϵ_p are the energies of the bare Fe d and chalcogen p orbitals, $U[= u - (20/9)j]$ is the multiplet-averaged d-d Coulomb interaction, and $n = 6$ is the number of Fe d electrons.

3.1.2 Mean-field treatment

When treating a many-body system, it is usually quite difficult to take its interaction of many-body effects into account. Instead of taking all the effects, they can be regarded as an averaged effect within the mean-field scheme. One can deduce the self-consistent equation using the averaged interaction, and solve the equation to obtain its solution. Note that this approximation can be applied to the system with small fluctuation (which is equivalent to the difference from the average).

In the multi-orbital d-p type Hamiltonian, the Hartree-Fock mean-field treatment is applied to the two-body part in $\hat{\mathscr{H}}_d$ by replacing its average values [34], i.e. the mean-field Hamiltonian is consequently given by

$$
\begin{aligned}
\hat{\mathscr{H}}^{\mathrm{HF}} =& \hat{\mathscr{H}}_p + \hat{\mathscr{H}}^{\mathrm{HF}}{}_d + \hat{\mathscr{H}}_{pd} \qquad (3.2)\\
\hat{\mathscr{H}}_p =& \sum_{kl\sigma} \epsilon_k^p p_{kl\sigma}^\dagger p_{kl\sigma} + \sum_{kll'\sigma} (V_{kll'}^{pp} p_{kl\sigma}^\dagger p_{kl'\sigma} + \text{h.c.})\\
\hat{\mathscr{H}}^{\mathrm{HF}}{}_d =& \epsilon_d^0 \sum_{i\alpha m\sigma} d_{i\alpha m\sigma}^\dagger d_{i\alpha m\sigma} + \sum_{i\alpha} \sum_{mm'\sigma\sigma'} h_{mm'\sigma\sigma'} d_{i\alpha m\sigma}^\dagger d_{i\alpha m'\sigma'}\\
&+ u \sum_{i\alpha m} \langle d_{i\alpha m\uparrow}^\dagger d_{i\alpha m\uparrow}\rangle d_{i\alpha m\downarrow}^\dagger d_{i\alpha m\downarrow} + u \sum_{i\alpha m} d_{i\alpha m\uparrow}^\dagger d_{i\alpha m\uparrow} \langle d_{i\alpha m\downarrow}^\dagger d_{i\alpha m\downarrow}\rangle\\
&- u \sum_{i\alpha m} \langle d_{i\alpha m\uparrow}^\dagger d_{i\alpha m\uparrow}\rangle \langle d_{i\alpha m\downarrow}^\dagger d_{i\alpha m\downarrow}\rangle + u' \sum_{i\alpha mm'} \langle d_{i\alpha m\uparrow}^\dagger d_{i\alpha m\uparrow}\rangle d_{i\alpha m'\downarrow}^\dagger d_{i\alpha m'\downarrow}\\
&+ u' \sum_{i\alpha mm'} d_{i\alpha m\uparrow}^\dagger d_{i\alpha m\uparrow} \langle d_{i\alpha m'\downarrow}^\dagger d_{i\alpha m'\downarrow}\rangle - u' \sum_{i\alpha mm'} \langle d_{i\alpha m\uparrow}^\dagger d_{i\alpha m\uparrow}\rangle \langle d_{i\alpha m'\downarrow}^\dagger d_{i\alpha m'\downarrow}\rangle\\
&+ (u' - j) \sum_{i\alpha} \sum_{mm'\sigma} \langle d_{i\alpha m\sigma}^\dagger d_{i\alpha m\sigma}\rangle d_{i\alpha m'\sigma}^\dagger d_{i\alpha m'\sigma}\\
&+ (u' - j) \sum_{i\alpha} \sum_{mm'\sigma} d_{i\alpha m\sigma}^\dagger d_{i\alpha m\sigma} \langle d_{i\alpha m'\sigma}^\dagger d_{i\alpha m'\sigma}\rangle\\
&- (u' - j) \sum_{i\alpha} \sum_{mm'\sigma} \langle d_{i\alpha m\sigma}^\dagger d_{i\alpha m\sigma}\rangle \langle d_{i\alpha m'\sigma}^\dagger d_{i\alpha m'\sigma}\rangle\\
&+ j \sum_{i\alpha mm'} \langle d_{i\alpha m\uparrow}^\dagger d_{i\alpha m'\uparrow}\rangle d_{i\alpha m'\downarrow}^\dagger d_{i\alpha m\downarrow} + j \sum_{i\alpha mm'} d_{i\alpha m\uparrow}^\dagger d_{i\alpha m'\uparrow} \langle d_{i\alpha m'\downarrow}^\dagger d_{i\alpha m\downarrow}\rangle\\
&- j \sum_{i\alpha mm'} \langle d_{i\alpha m\uparrow}^\dagger d_{i\alpha m'\uparrow}\rangle \langle d_{i\alpha m'\downarrow}^\dagger d_{i\alpha m\downarrow}\rangle + j' \sum_{i\alpha mm'} \langle d_{i\alpha m\uparrow}^\dagger d_{i\alpha m'\uparrow}\rangle d_{i\alpha m\downarrow}^\dagger d_{i\alpha m'\downarrow}\\
&+ j' \sum_{i\alpha mm'} d_{i\alpha m\uparrow}^\dagger d_{i\alpha m'\uparrow} \langle d_{i\alpha m\downarrow}^\dagger d_{i\alpha m'\downarrow}\rangle - j' \sum_{i\alpha mm'} \langle d_{i\alpha m\uparrow}^\dagger d_{i\alpha m'\uparrow}\rangle \langle d_{i\alpha m\downarrow}^\dagger d_{i\alpha m'\downarrow}\rangle\\
\hat{\mathscr{H}}_{pd} =& \sum_{kml\sigma} (V_{kml}^{pd} d_{km\sigma}^\dagger p_{kl\sigma} + \text{h.c.}). \qquad (3.3)
\end{aligned}
$$

In this Hartree-Fock calculation, we input the initial values of the order parameters such as$\langle d^\dagger d\rangle$ and diagonalize the mean-field Hamiltonian to get a set of eigen functions. Then the order parameters can be calculated using the obtained eigen functions. This self-consistency cycle is iterated until the successive difference of all the order parameters converge less than 10^{-4}.

Non-orthogonality of basis

Atomic orbitals on adjacent sites are not orthogonal and they have finite overlap (whereas the the orbitals on the same sites are orthogonal). In this thesis, the finite overlaps can be seen due to the ligand (chalcogen) p orbitals and Fe d orbitals in $FeCh_4$ tetrahedra:

$$S_{\alpha\beta} = \langle L_\alpha | d_\beta \rangle \qquad (3.4)$$

where α and β are the symmetries of each orbital. In order to make these basis orthogonal, one can re-take the molecular orbitals as

$$|L'_\alpha\rangle = |L_\alpha\rangle \tag{3.5}$$

$$|d'_\beta\rangle = |d_\beta\rangle + \sum_\alpha |L_\alpha\rangle S_{\beta\alpha}. \tag{3.6}$$

This form eliminates the non-orthogonality of p and d orbitals to first order of overlap S

$$\langle d'_\beta|L'_\alpha\rangle \approx S_{\beta\alpha} - S_{\beta\alpha} = 0 \tag{3.7}$$

then the energy eigenvalue of $\langle d'_\beta|\hat{\mathscr{H}}|d'_\beta\rangle/\langle d'_\beta|d'_\beta\rangle$ is

$$\frac{\langle d'_\beta|\hat{\mathscr{H}}|d'_\beta\rangle}{\langle d'_\beta|d'_\beta\rangle} = \frac{\epsilon_\beta - \sum_\alpha(S_{\alpha\beta}\mathscr{H}_{\beta\alpha} + \mathscr{H}_{\beta\alpha}S_{\alpha\beta}) + \sum_\alpha \epsilon_\alpha S_{\beta\alpha}S_{\alpha\beta}}{1 - \sum_\alpha S_{\beta\alpha}S_{\alpha\beta}}. \tag{3.8}$$

Taking the first order of S in the equation above, ϵ'_β becomes

$$\epsilon'_\beta = \epsilon_\beta - 2\sum_\alpha S_{\beta\alpha}\mathscr{H}_{\alpha\beta} \tag{3.9}$$

In the tetrahedral $FeCh_4$ cluster, d orbitals are reduced into the orbitals with t_{2g} and e_g symmetries, and its energy difference is described by $10Dq$. Here we can evaluate the $10Dq$, which is due to this non-orthogonality. Using the equation above, one can describe $10Dq$ as

$$\begin{aligned} 10Dq &= -2\sum_\alpha S_{\beta\alpha}\mathscr{H}_{\alpha\beta} \\ &= -2(S_eV_e - S_{t2}V_{t2}) \end{aligned} \tag{3.10}$$

where S and V are the overlap integrals and transfer integrals described by Fe d and ligand p orbitals with t_{2g} and e_g symmetries as below.

$$\begin{aligned} S_{t2} &= \langle L_{yz}|d_{yz}\rangle = \langle L_{zx}|d_{zx}\rangle = \langle L_{xy}|d_{xy}\rangle = 2S_\pi \\ V_{t2} &= \langle L_{yz}|\mathscr{H}_{pd}|d_{yz}\rangle = \langle L_{zx}|\mathscr{H}_{pd}|d_{zx}\rangle = \langle L_{xy}|\mathscr{H}_{pd}|d_{xy}\rangle = 2(pd\pi) \\ S_e &= \langle L_{x^2-y^2}|d_{x^2-y^2}\rangle = \langle L_{3z^2-r^2}|d_{3z^2-r^2}\rangle = -\sqrt{3}S_\sigma \\ V_e &= \langle L_{x^2-y^2}|\mathscr{H}_{pd}|d_{x^2-y^2}\rangle = \langle L_{3z^2-r^2}|\mathscr{H}_{pd}|d_{3z^2-r^2}\rangle = -\sqrt{3}(pd\sigma) \end{aligned} \tag{3.11}$$

Using these relations, $10Dq$ can be described as

$$10Dq = 2(-4S_\pi(pd\pi) + 3S_\sigma(pd\sigma)). \tag{3.12}$$

3.2 Anderson's impurity model calculation

3.2.1 Anderson Hamiltonian

On-site Coulomb interaction U plays an important role in other class of phenomena, for instance, Kondo [35–37] and heavy Fermion phenomena. Anderson has introduced a model Hamiltonian, so-called *Anderson Hamiltonian*, in order to address these phenomena [38]. The standard Anderson Hamiltonian includes conduction electrons and localized f electrons as below.

$$\mathscr{H}_{\mathrm{A}} = \sum_{\boldsymbol{k}\sigma} \varepsilon_{\boldsymbol{k}} c^{\dagger}_{\boldsymbol{k}\sigma} c_{\boldsymbol{k}\sigma} + \sum_{\sigma} \epsilon_f f^{\dagger}_{\sigma} f_{\sigma} + \sum_{\boldsymbol{k}\sigma} (V_{\boldsymbol{k}} f^{\dagger}_{\sigma} c_{\boldsymbol{k}\sigma} + \mathrm{h.c.}) + \frac{1}{2} U \sum_{\sigma \neq \bar{\sigma}} f^{\dagger}_{\sigma} f_{\sigma} f^{\dagger}_{\bar{\sigma}} f_{\bar{\sigma}} \quad (3.13)$$

In the limit of large U, the Anderson Hamiltonian is transformed to the Kondo Hamiltonian [9, 39].

3.2.2 Property of Anderson Hamiltonian

In order to see the property of this model Hamiltonian, we shall deduce the Green's function under the mean-field. When $U = 0$, the Green's function is used for unpertubed Hamiltonian in DMFT.

Mean-field approximation

First of all, we apply the mean-field approximation to the two-body part of the Hamiltonian as

$$\begin{aligned} U n_{f\uparrow} n_{f\downarrow} =& U\{\langle n_{f\uparrow}\rangle + (n_{f\uparrow} - \langle n_{f\uparrow}\rangle)\}\{\langle n_{f\downarrow}\rangle + (n_{f\downarrow} - \langle n_{f\downarrow}\rangle)\} \\ =& U\{\langle n_{f\uparrow}\rangle\langle n_{f\downarrow}\rangle + \langle n_{f\uparrow}\rangle n_{f\downarrow} - \langle n_{f\uparrow}\rangle\langle n_{f\downarrow}\rangle + n_{f\uparrow}\langle n_{f\downarrow}\rangle \\ & - \langle n_{f\uparrow}\rangle\langle n_{f\downarrow}\rangle - (n_{f\uparrow} - \langle n_{f\uparrow}\rangle)(n_{f\downarrow} - \langle n_{f\downarrow}\rangle)\} \\ \sim& U \sum_{\sigma} \langle n_{f\bar{\sigma}}\rangle n_{f\sigma} - U\langle n_{f\uparrow}\rangle\langle n_{f\downarrow}\rangle \end{aligned} \quad (3.14)$$

then the mean-field Anderson Hamiltonian has the form of

$$\begin{aligned} \mathscr{H}^{\mathrm{HF}}_{\mathrm{A}} &= \sum_{\boldsymbol{k}\sigma} \varepsilon_{\boldsymbol{k}} c^{\dagger}_{\boldsymbol{k}\sigma} c_{\boldsymbol{k}\sigma} + \sum_{\boldsymbol{k}\sigma} (V_{\boldsymbol{k}} f^{\dagger}_{\sigma} c_{\boldsymbol{k}\sigma} + \mathrm{h.c.}) + \sum_{\sigma} \epsilon_f f^{\dagger}_{\sigma} f_{\sigma} + U \sum_{\sigma} \langle f^{\dagger}_{\bar{\sigma}} f_{\bar{\sigma}}\rangle f^{\dagger}_{\sigma} f_{\sigma} \\ &= \sum_{\boldsymbol{k}\sigma} \varepsilon_{\boldsymbol{k}} c^{\dagger}_{\boldsymbol{k}\sigma} c_{\boldsymbol{k}\sigma} + \sum_{\boldsymbol{k}\sigma} (V_{\boldsymbol{k}} f^{\dagger}_{\sigma} c_{\boldsymbol{k}\sigma} + \mathrm{h.c.}) + \sum_{\sigma} (\epsilon_f + U\langle n_{f\bar{\sigma}}\rangle) f^{\dagger}_{\sigma} f_{\sigma} \\ &= \sum_{\boldsymbol{k}\sigma} \varepsilon_{\boldsymbol{k}} c^{\dagger}_{\boldsymbol{k}\sigma} c_{\boldsymbol{k}\sigma} + \sum_{\boldsymbol{k}\sigma} (V_{\boldsymbol{k}} f^{\dagger}_{\sigma} c_{\boldsymbol{k}\sigma} + \mathrm{h.c.}) + \sum_{\sigma} \tilde{\epsilon}_{f\sigma} f^{\dagger}_{\sigma} f_{\sigma} \end{aligned} \quad (3.15)$$

where $\tilde{\epsilon}_{f\sigma} \equiv \epsilon_f + U\langle n_{f\bar{\sigma}}\rangle$. This Hamiltonian has already been reduced to a one-body problem due to the mean-field treatment, *i.e.*, it can be diagonalized. In a

matrix representation, one can write using $\mathscr{H}_{\mathrm{A}}^{\mathrm{HF}} = \sum_\sigma \mathcal{H}_\sigma$ as

$$\mathcal{H}_\sigma = \begin{bmatrix} f_\sigma^\dagger & c_{\boldsymbol{k}_1\sigma}^\dagger & \dots & c_{\boldsymbol{k}_N\sigma}^\dagger \end{bmatrix} \begin{bmatrix} \tilde{\epsilon}_{f\sigma} & V_{\boldsymbol{k}_1}^* & \dots & V_{\boldsymbol{k}_N}^* \\ V_{\boldsymbol{k}_1} & \varepsilon_{\boldsymbol{k}_1} & & O \\ \vdots & & \ddots & \\ V_{\boldsymbol{k}_N} & O & & \varepsilon_{\boldsymbol{k}_N} \end{bmatrix} \begin{bmatrix} f_\sigma \\ c_{\boldsymbol{k}_1\sigma} \\ \vdots \\ c_{\boldsymbol{k}_N\sigma} \end{bmatrix} \tag{3.16}$$

which has the form of $\boldsymbol{a}_\sigma^\dagger \hat{\mathcal{H}}_\sigma \boldsymbol{a}_\sigma$; one can numerically diagonalize this Hamiltonian or find $\boldsymbol{\alpha}_\sigma$ that satisfies $\boldsymbol{a}_\sigma^\dagger \hat{\mathcal{H}}_\sigma \boldsymbol{a}_\sigma = \boldsymbol{\alpha}_\sigma^\dagger \hat{\mathcal{E}}_\sigma \boldsymbol{\alpha}_\sigma$ just like the Bogoliubov transformation in superconductivity.

Green's function method

The Green's function of f electron part can be calculated as

$$G_{ff,\sigma}(\varepsilon) = [\varepsilon - \tilde{\epsilon}_{f\sigma} - \sum_k \frac{|V_k|^2}{\varepsilon - \varepsilon_k}]^{-1}. \tag{3.17}$$

The last term of RHS can be re-written as

$$\begin{aligned} \sum_k \frac{|V_k|^2}{\varepsilon - \varepsilon_k} &= \int d\varepsilon' \frac{\sum_k |V_k|^2 \delta(\varepsilon' - \varepsilon_k)}{\varepsilon - \varepsilon' + i\delta} \sim \int d\varepsilon' \frac{|V|^2 \rho_c(\varepsilon')}{\varepsilon - \varepsilon' + i\delta} \\ &= \mathcal{P} \int d\varepsilon' \frac{|V|^2 \rho_c(\varepsilon')}{\varepsilon - \varepsilon'} - i\pi \int d\varepsilon' |V|^2 \rho_c(\varepsilon') \delta(\varepsilon - \varepsilon') \\ &= |V|^2 \mathcal{P} \int d\varepsilon' \frac{\rho_c(\varepsilon')}{\varepsilon - \varepsilon'} - i\pi |V|^2 \rho_c(\varepsilon) \end{aligned} \tag{3.18}$$

under the assumption that $|V_k|^2 = |V|^2$, and ρ_c denotes the DOS of conduction electrons. Suppose that the band width of conduction electron is W and the energy dependence of DOS of conduction electrons inside the band width is not so strong, one can approximate $\rho_c(\varepsilon) \sim \rho_c =$(const.). Then the Eq. (3.18) becomes

$$\begin{aligned} \sum_k \frac{|V_k|^2}{\varepsilon - \varepsilon_k} &\sim |V|^2 \mathcal{P} \int_{-W/2}^{W/2} d\varepsilon' \frac{\rho_c(\varepsilon')}{\varepsilon - \varepsilon'} - i\pi |V|^2 \rho_c \\ &= |V|^2 \rho_c \log \frac{\varepsilon + (W/2)}{\varepsilon - (W/2)} - i\Delta \sim -i\Delta. \end{aligned} \tag{3.19}$$

Finally, the Green's function and DOS of f electrons become

$$\begin{aligned} G_{ff,\sigma}(\varepsilon) &\sim \frac{1}{\varepsilon - \tilde{\epsilon}_{f\sigma} + i\Delta} \\ \rho_{ff,\sigma}(\varepsilon) &= -\frac{1}{\pi} \Im m[G_{ff,\sigma}(\varepsilon)] \sim \frac{\Delta}{\pi} \frac{1}{(\varepsilon - \tilde{\epsilon}_{f\sigma})^2 + \Delta^2}. \end{aligned} \tag{3.20}$$

The Green's function indicates that the f electrons have finite lifetime; when one electron is wandering in the 'sea' of the conduction electron, it would be trapped by the impurity about the duration of $1/\Delta$. The DOS of f electrons is the Lorentz shape centered at $\varepsilon = \tilde{\epsilon}_{f\sigma}$.

3.3 First-principles calculation

First-principles calculation is the band-structure calculation using only the crystal structure and its elements, namely, without using empirical and/or experimental facts. In this section, we briefly take a look at how it works. In order to obtain the electronic structure, it is required to solve the Schrödinger equation of a crystal. The Hamiltonian of a crystal contains electron-term, nuclear-term, and electron-nuclear interaction. Applying the Born-Oppenheimer approximation, the nuclear terms can be neglected as

$$\begin{aligned}\mathscr{H} =& T + U + V_{\text{ext}} + T_n + U_n \\ =& -\frac{1}{2}\sum_i \nabla_i^2 + \frac{1}{2}\sum_{i\neq j}\frac{1}{|\boldsymbol{r}_i - \boldsymbol{r}_j|} - \frac{1}{2}\sum_{i,n}\frac{Z_n}{|\boldsymbol{r}_i - \boldsymbol{R}_n|} \\ & -\sum_I \frac{1}{2M_I}\nabla_I^2 + \frac{1}{2}\sum_{I\neq J}\frac{Z_I Z_J}{|\boldsymbol{R}_I - \boldsymbol{R}_J|} \qquad (3.21) \\ \sim& T + U + V_{\text{ext}} \qquad (3.22)\end{aligned}$$

which contains the kinetic term of electron, electron-electron Coulomb interaction, and electron-nucleus Coulomb interaction. The Hamiltonian here is written in Hartree unit.

Hohenberg-Kohn method

In order to approach to the many-body problem in the first-principles, density functional theory (DFT) is widely used. General concept of DFT is based on the assumption that any interacting many-body systems can be treated as a functional of ground state particle density n_0. The formalism of the DFT was originated in the work by Hohenberg and Kohn in 1964 [40], which proved that the one-particle density at ground state energy played an important role in many-body systems as in the following theorems.

theorem 1 *Existence; the ground state energy E_g is uniquely determined by one-electron density $n_0(\boldsymbol{r})$. The density $n_0(\boldsymbol{r})$ is derived from the Schrödinger equation with an external potential $V_{ext}(\boldsymbol{r}_i)$ except constant potential.*

theorem 2 *Variational method; the ground state energy $E_g[n]$ is given by the density $n(\boldsymbol{r})$, and its minimal value is given if and only if the input density $n_0(\boldsymbol{r})$ is the ground state density , i.e., $E_g[n_0(\boldsymbol{r})] < E_g[n(\boldsymbol{r})]$.*

The Hamiltonian and total energy within the Hohenberg-Kohn method are given by

$$\mathscr{H}^{\mathrm{HK}} = \sum_{i=1}[-\frac{1}{2}\nabla_i^2 + V_{\mathrm{ext}}(\boldsymbol{r}_i)] + \frac{1}{2}\sum_{r_i \neq r_j}\frac{1}{|\boldsymbol{r}_i - \boldsymbol{r}_j|} \tag{3.23}$$

$$E^{\mathrm{HK}}[n] = T[n] + \int d\boldsymbol{r} V_{\mathrm{ext}}(\boldsymbol{r})n(\boldsymbol{r}) + E_{\mathrm{int}}[n]. \tag{3.24}$$

Once the external potential $V_{\mathrm{ext}}(\boldsymbol{r}_i)$is determined, the corresponding ground state wave function can be uniquely determined as well.

Kohn-Sham method

The energy calculation using only electron density combined with Thomas-Fermi approximation [41,42] was challenging in terms of numerical precision. Therefore, Kohn and Sham introduced a set of wave function (so-called Kohn-Sham orbital) to the DFT with the following assumptions [43].

assumption 1 *The exact density of ground state can be expressed by the density of the ground state in a fictious non-interacting system.*

assumption 2 *The Hamiltonian of the fictious system,* Kohn-Sham auxiliary system*, consists of normal kinetic term and effective potential V^{KS}.*

Under the assumptions above, Kohn-Sham equation is given by

$$\mathscr{H}^{\mathrm{KS}}\phi_i(\boldsymbol{r}) = [-\frac{1}{2}\nabla_i^2 + V^{\mathrm{KS}}]\phi_i(\boldsymbol{r}) = \varepsilon_i\phi_i(\boldsymbol{r}) \tag{3.25}$$

where n_0 satisfies

$$n_0(r) = \sum_{i=1}|\phi_i(\boldsymbol{r})|^2 \tag{3.26}$$

The Kohn-Sham kinetic term and classical Coulomb interaction (Hatree energy) can be respectively defined by

$$T^{\mathrm{KS}} = -\frac{1}{2}\sum_i\langle\phi_i|\nabla^2|\phi_i\rangle,\ E^{\mathrm{H}} = \frac{1}{2}\int d\boldsymbol{r}d\boldsymbol{r'}\frac{n(\boldsymbol{r})n(\boldsymbol{r'})}{|\boldsymbol{r} - \boldsymbol{r'}|}. \tag{3.27}$$

The total energy of the Kohn-Sham system can be expressed as

$$E^{\mathrm{KS}}[n] = T^{\mathrm{KS}}[n] + \int d\boldsymbol{r} V_{\mathrm{ext}}(\boldsymbol{r})n(\boldsymbol{r}) + E^{\mathrm{H}}[n] + E^{\mathrm{xc}}[n] \tag{3.28}$$

where $E^{\mathrm{xc}}[n]$ is so-called exchange-correlation energy, which is defined by the energy difference between the interacting Hohenberg-Kohn system and non-interacting Kohn-Sham system expressed as

$$\begin{aligned} E^{\mathrm{xc}}[n] &= E^{\mathrm{HK}}[n] - E^{\mathrm{KS}}[n] \\ &= (T[n] - T^{\mathrm{KS}}[n]) + (E_{\mathrm{int}}[n] - E^{\mathrm{H}}[n]) \end{aligned} \tag{3.29}$$

and it is often approximated by LDA or GGA;

$$E^{\text{xc}}_{\text{LDA}} = \int d\boldsymbol{r}\ n(\boldsymbol{r})\varepsilon^{\text{xc}}_{\text{gas}}(n) \tag{3.30}$$

$$E^{\text{xc}}_{\text{GGA}} = \int d\boldsymbol{r}\ n(\boldsymbol{r})\varepsilon^{\text{xc}}_{\text{gas}}(n, \nabla n, \cdots) \tag{3.31}$$

where $\varepsilon^{\text{xc}}_{\text{gas}}$ is the one-electron exchange-correlation energy of interacting homogeneous electron gas. Once the exchange-correlation term is determined, the exact ground state energy and electrons density of many-body system can be deduced by solving the Kohn-Sham equation. Using the variational method on $E^{\text{KS}}[n]$ with respect to the Kohn-Sham orbital, one can obtain

$$\begin{aligned}\mathscr{H}^{\text{KS}} &= -\frac{1}{2}\nabla_i^2 + V^{\text{KS}}(\boldsymbol{r}) \\ &= -\frac{1}{2}\nabla_i^2 + V_{\text{ext}} + \frac{\delta E^{\text{H}}[n]}{\delta n} + \frac{\delta E^{\text{xc}}[n]}{\delta n} \\ &= -\frac{1}{2}\nabla_i^2 + V_{\text{ext}} + V^{\text{H}} + V^{\text{xc}}\end{aligned} \tag{3.32}$$

and the total energy using the Kohn-Sham levels (ε_i) can be

$$E = \sum_i \varepsilon_i - E^{\text{H}}[n] + E^{\text{xc}}[n] - \int d\boldsymbol{r}\frac{\delta E^{\text{H}}[n]}{\delta n(\boldsymbol{r})}. \tag{3.33}$$

Since the Kohn-Sham system is a fictious system, the eigen energies in Kohn-Sham equation have no physical meaning in principle. However, the following relation

$$\frac{\partial E}{\partial n_i} = \varepsilon_i, \tag{3.34}$$

so-called Janak theorem, was confirmed [44]. The orbital energy is given by the differential while in Koopmans' theorem (see details in 4.2.3, section 4) it is given by the difference ($E^N - E^{N-1}$) for large N within Hartree-Fock scheme. When the difference between 'differential' and 'difference' is small, it is possible to regard ε_i as ionization energy. When the Kohn-Sham levels have physical meaning such as ionization energy, it is possible to compare with experimental results such as photoemission spectroscopy.

4

PRINCIPLE OF EXPERIMENT

Photoemission and absorption spectroscopy have been used in order to investigate the electronic structures of Fe-based and BiS_2-based systems. In this chapter, therefore, we shall see the principle and theoretical description of them.

4.1 Introduction

In the experimental techniques of photoemission and photon absorption spectroscopy, we use light (photon) to excite electrons in solids, *i.e.*, the electron-photon interaction and its quantum transition probability are important. Therefore, we will take a look at these phenomena in the first section, and then will see the principles of photoemission and photon absorption spectroscopy.

4.1.1 Electron-photon interaction

The second-quantized vector potential operator $\boldsymbol{A}(\boldsymbol{r},t)$ is given by

$$\boldsymbol{A}(\boldsymbol{r},t) = \frac{1}{\sqrt{V}}\sum_{\boldsymbol{k}}\sum_{\alpha=1,2}\sqrt{\frac{\hbar}{2\varepsilon_0\omega}}(\hat{a}_{\boldsymbol{k}\alpha}e^{i\boldsymbol{k}\cdot\boldsymbol{r}-i\omega t}\boldsymbol{\varepsilon}^{\alpha} + \hat{a}^{\dagger}_{\boldsymbol{k}\alpha}e^{-i\boldsymbol{k}\cdot\boldsymbol{r}+i\omega t}\boldsymbol{\varepsilon}^{\alpha}) \tag{4.1}$$

where $\hat{a}^{\dagger}_{\boldsymbol{k}\alpha}$ is an creation operator of photon polarized in the direction α with wave number $\boldsymbol{k}$, and $\boldsymbol{\varepsilon}^{\alpha}$ is a polarization vector in the direction α. Now we consider the electron-photon interaction in an N-electron system. The energy eigenstate of the N-electron system interacting with the electromagnetic wave given by the vector potential operator $\boldsymbol{A}(\boldsymbol{r},t)$ is described by the Shrödinger equation as below

$$i\hbar\frac{d}{dt}|\boldsymbol{r}_1,\boldsymbol{r}_2,\cdots,\boldsymbol{r}_N,t\rangle = \hat{\mathscr{H}}|\boldsymbol{r}_1,\boldsymbol{r}_2,\cdots,\boldsymbol{r}_N,t\rangle \tag{4.2}$$

where the Hamiltonian is given by

$$\begin{aligned}\hat{\mathscr{H}} &= \sum_i \frac{\{\boldsymbol{p}_i + e\boldsymbol{A}(\boldsymbol{r}_i,t)\}^2}{2m} \\ &= \sum_i \frac{\boldsymbol{p}_i^2}{2m} + \sum_i[\frac{e}{2m}\{\boldsymbol{p}_i\cdot\boldsymbol{A}(\boldsymbol{r}_i,t) + \boldsymbol{A}(\boldsymbol{r}_i,t)\cdot\boldsymbol{p}_i\} + \frac{e^2}{2m}\boldsymbol{A}(\boldsymbol{r}_i,t)^2].\end{aligned} \tag{4.3}$$

When we take the first term as an unperturbed Hamiltonian $\hat{\mathscr{H}}_0$, the interaction part can be defined as

$$\hat{\mathscr{H}}_{\text{int}} = \sum_i[\frac{e}{2m}\{\boldsymbol{p}_i\cdot\boldsymbol{A}(\boldsymbol{r}_i,t) + \boldsymbol{A}(\boldsymbol{r}_i,t)\cdot\boldsymbol{p}_i\} + \frac{e^2}{2m}\boldsymbol{A}(\boldsymbol{r}_i,t)^2] \tag{4.4}$$

where the first and second terms correspond to the photon absorption and emission processes, respectively, and the the third term represents the scattering process. One can evaluate the transition probabilities of these processes by the first-order perturbation theory as in the next subsection (transition probability).

4.1.2 Transition probability

The (quantum mechanical) transition probability describes the transition rate from one energy eigenstate to a continuum energy eigenstate due to the first-order perturbation on the electron-photon interaction term. It corresponds to the photoionized transition and the dipole ($E1$) transition in photoemission and absorption experiment, respectively.

The time-dependent perturbation theory is a starting point to gain the transition probability. When the Hamiltonian is given by equation (4.3), the Shrödinger equation also can be

$$(\hat{\mathscr{H}}_0 + \hat{\mathscr{H}}_{\text{int}})|\Psi(t)\rangle = i\hbar\frac{\partial}{\partial t}|\Psi(t)\rangle \tag{4.5}$$

Then $|\Psi(t)\rangle$ can be expanded as a linear combination of the eigenstates $|n(t)\rangle$ which satisfies $\hat{\mathscr{H}}_0|n(t)\rangle = E_n|n(t)\rangle$

$$|\Psi(t)\rangle = \sum_n |n(t)\rangle\langle n(t)|\Psi(t)\rangle \equiv \sum_n c_n(t)e^{-i\hat{\mathscr{H}}_0 t/\hbar}|n\rangle \tag{4.6}$$

where $c_n(t)$ is a coefficient of eigenstate $|n(t)\rangle$, and this coefficient gives the transition probability amplitude. Plugging this expanded eigenstate into the Shrödinger equation and we obtain

$$\begin{aligned}(\hat{\mathscr{H}}_0 + \hat{\mathscr{H}}_{\text{int}})\sum_n c_n(t)e^{-i\hat{\mathscr{H}}_0 t/\hbar}|n\rangle &= i\hbar\frac{\partial}{\partial t}\sum_n c_n(t)e^{-i\hat{\mathscr{H}}_0 t/\hbar}|n\rangle \\ \therefore \quad \sum_n [i\hbar\frac{\partial c_n(t)}{\partial t} - c_n(t)\hat{\mathscr{H}}_{\text{int}}]e^{-i\hat{\mathscr{H}}_0 t/\hbar}|n\rangle &= 0.\end{aligned} \tag{4.7}$$

Multiplying the eigenstate $\langle m|$ from the left and changing the labels as $m \to n, n \to k$, one can obtain

$$\frac{\partial c_n(t)}{\partial t} = \frac{1}{i\hbar}\sum_k c_k(t)\langle n|\hat{\mathscr{H}}_{\text{int}}|k\rangle e^{-i(E_k - E_n)t/\hbar} \tag{4.8}$$

Consequently, $c_n(t)$ is

$$c_n(t) = c_n^{(0)} + \frac{1}{i\hbar}\int_0^t \sum_k c_k(t')\langle n|\hat{\mathscr{H}}_{\text{int}}|k\rangle e^{-i(E_k - E_n)t'/\hbar}dt' \tag{4.9}$$

By repeatedly substituting this expression for $c_n(t)$ back into right hand side, we get an iterative solution with the form of

$$c_n(t) = c_n^{(0)} + c_n^{(1)} + c_n^{(2)} + \cdots \tag{4.10}$$

where the first term is given by

$$c_n^{(1)} = \frac{1}{i\hbar}\int_0^t \sum_k c_k^{(0)}\langle n|\hat{\mathscr{H}}_{\text{int}}|k\rangle e^{-i(E_k - E_n)t'/\hbar}dt'. \tag{4.11}$$

Taking $|k\rangle$ as the initial state with $n_{\boldsymbol{k}\alpha}$ photons $|i, n_{\boldsymbol{k}\alpha}\rangle$ and $|n\rangle$ as the final state with $(n_{\boldsymbol{k}\alpha} - 1)$ photons $|f, n_{\boldsymbol{k}\alpha} - 1\rangle$, the photon absorption process (the first term of equation (4.4)) can be calculated within the first-order perturbation as

$$\begin{aligned}
&\langle f, n_{\boldsymbol{k}\alpha} - 1|\hat{\mathscr{H}}_{\text{int}}|i, n_{\boldsymbol{k}\alpha}\rangle \\
&\qquad = \frac{e}{m}\sum_i \langle f, n_{\boldsymbol{k}\alpha} - 1|\boldsymbol{p}_i \cdot \sqrt{\frac{\hbar}{2\varepsilon_0\omega V}}(\hat{a}_{\boldsymbol{k}\alpha}e^{i\boldsymbol{k}\cdot\boldsymbol{r}_i - i\omega t}\boldsymbol{\varepsilon}^\alpha)|i, n_{\boldsymbol{k}\alpha}\rangle \\
&\qquad = \frac{e}{m}\sqrt{\frac{n_{\boldsymbol{k}\alpha}\hbar}{2\varepsilon_0\omega V}}\sum_i \langle f|\boldsymbol{p}_i \cdot \boldsymbol{\varepsilon}^\alpha e^{i\boldsymbol{k}\cdot\boldsymbol{r}}|i\rangle e^{-i\omega t}. \qquad (4.12)
\end{aligned}$$

When the absorption occurs spontaneously in the case of single electron, we can omit the summation of i, thus we can obtain the transition probability amplitude as

$$c_{i\to f}^{(1,\text{abs})}(t) = \frac{1}{i\hbar}\int_0^t \frac{e}{m}\sqrt{\frac{n_{\boldsymbol{k}\alpha}\hbar}{2\varepsilon_0\omega V}}\langle f|\boldsymbol{p}_i \cdot \boldsymbol{\varepsilon}^\alpha e^{i\boldsymbol{k}\cdot\boldsymbol{r}}|i\rangle e^{i(E_f - E_i - \hbar\omega)t'}dt'. \qquad (4.13)$$

In order to obtain the transition probability, one needs to take a square of the quantity $c_{i\to f}(t)$ since this is just an amplitude. Taking a square of the equation above follows

$$|c_{i\to f}^{(1,\text{abs})}(t)|^2 = \frac{\pi e^2}{m^2\varepsilon_0\omega V}|\langle f|\boldsymbol{p}_i \cdot \boldsymbol{\varepsilon}^\alpha e^{i\boldsymbol{k}\cdot\boldsymbol{r}}|i\rangle|^2 t\delta(E_f - E_i - \hbar\omega). \qquad (4.14)$$

Then the transition probability per unit time in a solid angle (so called *differential cross-section*) using *dipole approximation* is described by

$$\begin{aligned}
\frac{dw}{d\Omega} &= \int \frac{|c_{i\to f}^{(\text{abs})}(t)|^2}{t}\frac{V\omega^2}{(2\pi)^3\hbar c^3}d(\hbar\omega) \\
&= \frac{e^2\omega}{8\pi^2\varepsilon_0 m^2\hbar c^3}|\langle f|\boldsymbol{p} \cdot \boldsymbol{\varepsilon}^\alpha e^{-i\boldsymbol{k}\cdot\boldsymbol{r}}|i\rangle|^2 \\
&= \frac{e^2\omega}{8\pi^2\varepsilon_0 m^2\hbar c^3}|\langle f|\boldsymbol{p}(1 - i\boldsymbol{k}\cdot\boldsymbol{r} + \cdots)|i\rangle \cdot \boldsymbol{\varepsilon}^\alpha|^2 \\
&\simeq \frac{e^2\omega}{8\pi^2\varepsilon_0 m^2\hbar c^3}|\langle f|\boldsymbol{p}|i\rangle \cdot \boldsymbol{\varepsilon}^\alpha|^2 \quad (\leftarrow \text{dipole approximation}) \\
&= \frac{e^2\omega}{8\pi^2\varepsilon_0 m^2\hbar c^3}|\langle f|\frac{im}{\hbar}[\hat{\mathscr{H}}, \boldsymbol{r}]|i\rangle \cdot \boldsymbol{\varepsilon}^\alpha|^2 \\
&= \frac{e^2\omega}{8\pi^2\varepsilon_0 m^2\hbar c^3}|\langle f|\frac{im}{\hbar}(E_f - E_i)\boldsymbol{r}|i\rangle \cdot \boldsymbol{\varepsilon}^\alpha|^2 \\
&= \frac{e\omega^3}{8\pi^2\varepsilon_0\hbar c^3}|\langle f|e\boldsymbol{r} \cdot \boldsymbol{\varepsilon}^\alpha|i\rangle|^2 \\
&\equiv \frac{e\omega^3}{8\pi^2\varepsilon_0\hbar c^3}|T_{fi}|^2 \qquad (4.15)
\end{aligned}$$

where T_{fi} is the matrix element of dipole operator between one-particle states $|f\rangle$ and $|i\rangle$. In general, there are several final states, and therefore one can define a

photoexcitaiton operator M_i using the matrix element of dipole operator as

$$M_i = \sum_f T_{fi} c_f^\dagger c_i. \tag{4.16}$$

As for the second term of equation (4.4) (photon emission process), we can also similarly calculate the probability amplitude $c_{i\to f}^{(1,\text{ems})}(t)$ using the perturbation theory and its differential cross-section as we just performed above.

4.2 Photoemission spectroscopy

The phenomenon of photoelectric effect was firstly detected by a German physicist, H. R. Hertz, in 1887, and was formulated as light quantum theory by A. Einstein [45]. This discovery led to the quantum revolution in physics and earned Einstein the Nobel Prize in Physics in 1921. The principle of photoemission spectroscopy (PES) is based on light quantum theory. Experimental method of PES is analyzing the energy distribution of photoelectrons, which are excited by photons from a light source.

4.2.1 General formulation

The technique of photoemission spectroscopy has been widely used as one of the most powerful tool to investigate the electronic structure of solids. When an electron in a solid absorbs a photon of sufficiently high energy, it is emitted as a photoelectron. Schematic diagram of the experimental principle is shown in Figure 4.1. From the energy conservation law, the kinetic energy of the photoelectron can be written as

$$E_{\text{kin}}^{\text{vac}} = h\nu - E_B - \Phi \tag{4.17}$$

where, $E_{\text{kin}}^{\text{vac}}$ is the kinetic energy measured from the vacuum level (E^{vac}), Φ is the work function of the sample, and E_B is the binding energy with respect to the Fermi level (E_F) or chemical potential μ. In an actual experiment, the kinetic energy ($E_{\text{kin}} = E_{\text{kin}}^{\text{vac}} + \Phi$) is measured with respect to E_F. Hence, it is convenient to use the equation

$$E_{\text{kin}} = h\nu - E_B. \tag{4.18}$$

The electronic structure of the occupied states such as core levels and the valence band can be obtained by measuring the energy spectrum of photoelectrons. From this relation, the binding energy of photoelectrons can be measured, and the intensity of photoemission spectrum is proportional to the density of states (DOS) of the occupied states, *i.e.*, PES is an experimental method to investigate the occupied electronic states below the Fermi level [46].

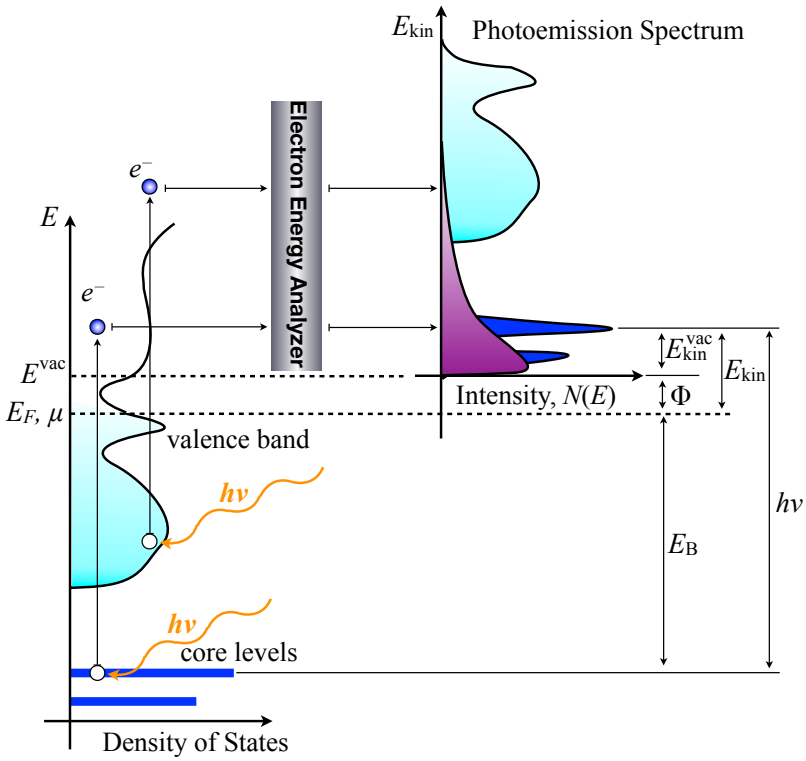

Figure 4.1: Schematic diagrams of the principle of photoemission spectroscopy.

4.2.2 Frank-Condon principle

In the photoemission process, one can treat as if the lattice (atoms) is frozen and there is no interaction between photoelectron and remaining system. This is so-called Frank-Condon principle, also known as Born-Oppenheimer approximation. The timescales of the optical excitation and emission of photoelectron are about 10^{-15} seconds while that of movement of crystal lattice is around 10^{-12} seconds. Note that this approximation is good for the high-energy photoelectron limit (10 - 1000 eV photons).

Since the photoelectron and remaining system can be separately treated, let us divide the wave functions of the initial ground and final states into photoelectron and the remaining$(N-1)$-electron-system.

$$
\begin{aligned}
|\Psi_g^N\rangle &= \hat{\mathscr{A}}|i\rangle \otimes |\Psi_i^{N-1}\rangle \\
|\Psi_f^N\rangle &= \hat{\mathscr{A}}|f\rangle \otimes |\Psi_f^{N-1}\rangle
\end{aligned}
\tag{4.19}
$$

Here, $\hat{\mathscr{A}}$ is an operator to antisymmetrize the entire wave function , $|i\rangle$ ($|f\rangle$) is the initial (final) state of the photoelectron, and $|\Psi_i^{N-1}\rangle$ ($|\Psi_f^{N-1}\rangle$) the initial (final) state of $(N-1)$-electron system. Therefore, transition probability from $|\Psi_i^N\rangle$ to $|\Psi_f^N\rangle$

can be calculated as

$$
\begin{aligned}
||\langle\Psi_f^N|\hat{\mathscr{H}}_{\text{int}}|\Psi_g^N\rangle||^2 &= ||\langle f|\hat{\mathscr{H}}_{\text{int}}|i\rangle\langle\Psi_f^{N-1}|\Psi_i^{N-1}\rangle||^2 \\
&= |T_{fi}|^2 \cdot ||\langle\Psi_f^{N-1}|\Psi_i^{N-1}\rangle||^2 \propto |T_{fi}|^2. \qquad (4.20)
\end{aligned}
$$

4.2.3 Koopmans' theorem

The eigenvalue $\epsilon_{\boldsymbol{k}\sigma}$ of Hartree-Fock equation is the expectation value of Hartree-Fock operator with one-electron state $\phi_{\boldsymbol{k}\sigma}$, as follows.

$$
\begin{aligned}
\epsilon_{\boldsymbol{k}\sigma} &= \langle\phi_{\boldsymbol{k}\sigma}|\hat{h}^{\text{HF}}|\phi_{\boldsymbol{k}\sigma}\rangle \\
&= \langle\phi_{\boldsymbol{k}\sigma}|\hat{h}|\phi_{\boldsymbol{k}\sigma}\rangle + \sum_{\boldsymbol{k}'\sigma'}^{\boldsymbol{k}^{(N)}}[U_{\boldsymbol{k}\sigma\boldsymbol{k}'\sigma'} - J_{\boldsymbol{k}\sigma\boldsymbol{k}'\sigma'}\delta_{\sigma\sigma'}] \\
&= \langle\phi_{\boldsymbol{k}\sigma}|\hat{h}|\phi_{\boldsymbol{k}\sigma}\rangle + \sum_{\boldsymbol{k}'\sigma'}^{\boldsymbol{k}^{(L)}}[U_{\boldsymbol{k}\sigma\boldsymbol{k}'\sigma'} - J_{\boldsymbol{k}\sigma\boldsymbol{k}'\sigma'}\delta_{\sigma\sigma'}]\langle n_{\boldsymbol{k}'\sigma'}\rangle \qquad (4.21)
\end{aligned}
$$

where

$$
\begin{aligned}
U_{\boldsymbol{k}\sigma\boldsymbol{k}'\sigma'} &= \iint d\boldsymbol{x}_1 d\boldsymbol{x}_2 \Psi_{k\sigma}^*(\boldsymbol{r}_1)\Psi_{k'\sigma'}^*(\boldsymbol{r}_2)\frac{e^2}{r_{12}}\Psi_{k\sigma}(\boldsymbol{r}_1)\Psi_{k'\sigma'}(\boldsymbol{r}_2) \\
J_{\boldsymbol{k}\sigma\boldsymbol{k}'\sigma'} &= \iint d\boldsymbol{x}_1 d\boldsymbol{x}_2 \Psi_{k'\sigma'}^*(\boldsymbol{r}_1)\Psi_{k\sigma}^*(\boldsymbol{r}_2)\frac{e^2}{r_{12}}\Psi_{k\sigma}(\boldsymbol{r}_1)\Psi_{k'\sigma'}(\boldsymbol{r}_2)
\end{aligned}
$$

The first term of Eq. (4.21) denotes the energy of one-electron, and the second term represents the summation of Coulomb and exchange integral.

As for the first line of Eq. (4.21), the summation was taken up to the Fermi level (the highest occupied states). As for the second line, the summation was taken for all the states including unoccupied states. The quantity $\langle n_{\boldsymbol{k}'}\rangle$ is the expectation value of number of electron that occupies the one-electron state $\phi^{\boldsymbol{k}}$, *i.e.* $\langle n_{\boldsymbol{k}'}\rangle = 0$ or 1. The total energy of N-electron system E_N^{HF} is given by

$$
\begin{aligned}
E_N^{\text{HF}} &= \langle\Psi_N^{\text{HF}}|\hat{\mathscr{H}}_N|\Psi_N^{\text{HF}}\rangle \\
&= \sum_{\boldsymbol{k}\sigma}^{\boldsymbol{k}^{(N)}}\epsilon_{\boldsymbol{k}\sigma} - \frac{1}{2}\sum_{\boldsymbol{k}\sigma\boldsymbol{k}'\sigma'}^{\boldsymbol{k}^{(N)}}[U_{\boldsymbol{k}\sigma\boldsymbol{k}'\sigma'} - J_{\boldsymbol{k}\sigma\boldsymbol{k}'\sigma'}\delta_{\sigma\sigma'}] \\
&= \sum_{\boldsymbol{k}\sigma}^{\boldsymbol{k}^{(L)}}\epsilon_{\boldsymbol{k}\sigma}\langle n_{\boldsymbol{k}\sigma}\rangle - \frac{1}{2}\sum_{\boldsymbol{k}\sigma\boldsymbol{k}'\sigma'}^{\boldsymbol{k}^{(L)}}[U_{\boldsymbol{k}\sigma\boldsymbol{k}'\sigma'} - J_{\boldsymbol{k}\sigma\boldsymbol{k}'\sigma'}\delta_{\sigma\sigma'}]\langle n_{\boldsymbol{k}\sigma}\rangle\langle n_{\boldsymbol{k}'\sigma'}\rangle \qquad (4.22)
\end{aligned}
$$

The factor (1/2) in front of the second term is a correction for double count. Here we can calculate the energy difference between the state $|\Psi_N^{\text{HF}}\rangle$ and $|\Psi_{N-1,k}^{\text{HF}}\rangle$, where $|\Psi_{N-1,k}^{\text{HF}}\rangle$ is the wave function of the remaining $(N-1)$-electron system without photoelectron $|\phi_f^{\boldsymbol{k}}\rangle$.

$$
\langle\Psi_{N-1,\boldsymbol{k}\sigma}^{\text{HF}}|\hat{\mathscr{H}}_{N-1}|\Psi_{N-1,\boldsymbol{k}\sigma}^{\text{HF}}\rangle - \langle\Psi_N^{\text{HF}}|\hat{\mathscr{H}}_N|\Psi_N^{\text{HF}}\rangle = -\epsilon_{\boldsymbol{k}\sigma} \qquad (4.23)
$$

The equation above indicates

$$E_B = -\epsilon_{\boldsymbol{k\sigma}}, \tag{4.24}$$

namely, the energy $-\epsilon_{\boldsymbol{k}\sigma}$ is necessary in order to eject an electron whose state is in $|\phi^{\boldsymbol{k\sigma}}\rangle$ from the N-electron system. This is called *Koopmans' theorem* [47]. Here we suppose that the remaining $(N-1)$ one-electron wavefunctions do not change due to this photoemission process (Frank-Condon principle).

4.2.4 Photoemission spectrum

The energy distribution of photoelectrons is called photoemission spectrum, and it can be expressed by the transition probability from Ψ_g^N to Ψ_f^N that satisfies the energy conservation ($E_g^N - E_n^{N-1} = \varepsilon$, *i.e.*, $\varepsilon + E_n^{N-1} - E_g^N = 0$):

$$\begin{aligned}
\rho^{\text{PES}}(\varepsilon) &= \sum_{n,l} ||\langle\Psi_f^N|\sum_k T_{lk}c_l^\dagger c_k|\Psi_g^N\rangle||^2\delta(\varepsilon + E_n^{N-1} - E_g^N) \\
&= \sum_{n,l} ||\langle\Psi_n^{N-1}|\otimes\langle l|\sum_k T_{lk}c_l^\dagger c_k|\Psi_g^N\rangle||^2\delta(\varepsilon + E_n^{N-1} - E_g^N) \\
&\propto \sum_{n,k} ||\langle\Psi_n^{N-1}|c_k|\Psi_g^N\rangle||^2\delta(\varepsilon + E_n^{N-1} - E_g^N)
\end{aligned} \tag{4.25}$$

when the index dependent of $T_l k$ is neglected. The ground state wave function $|\Psi_g^N\rangle$ includes the photoelectron subspace as in Eq. (4.19). The photoemission spectrum can be generally expressed by spectral function, which is an imaginary part of a single-particle Green's function.

Green's function and spectral function

The time- and spatial evolution of N-electron system can be described by Green's function. Let us define the retarded Green's function $G^R(\boldsymbol{k}, t)$ as below

$$G^R(\boldsymbol{k}, t) = \frac{1}{i\hbar}\theta(t)\langle\Psi_g^N|\hat{\mathscr{T}}[\hat{c}_{\boldsymbol{k}}(t)\hat{c}_{\boldsymbol{k}}^\dagger]|\Psi_g^N\rangle. \tag{4.26}$$

Here, $\hat{c}_{\boldsymbol{k}}^\dagger$ is a creation operator of electron with momentum $\boldsymbol{k}$, $\theta(t)$ denotes the Heaviside step function, $A(t) = e^{-\mathscr{H}t/i\hbar}Ae^{\mathscr{H}t/i\hbar}$, and $\hat{\mathscr{T}}$ represents *Wick's chronological product*.

In order to analyze the mathematical properties of this Green's function, it is convenient in many-body calculations to use the *spectral function* as we discussed, which contains 'renormalized' propagators. The spectral decomposition of a time-dependent function into the sum of its components at various frequencies consequently gives the form of

$$G^R(\boldsymbol{k}, t) = \frac{1}{i\hbar}\theta(t)\int_0^\infty d\varepsilon A^+(\boldsymbol{k}, \varepsilon)e^{-\frac{i}{\hbar}(\varepsilon+\mu)t} - \frac{1}{i\hbar}\theta(-t)\int_0^\infty d\varepsilon A^-(\boldsymbol{k}, \varepsilon)e^{+\frac{i}{\hbar}(\varepsilon-\mu)t} \tag{4.27}$$

where μ is the chemical potential ($\mu = E_0^N - E_0^{N-1}$). Then the Fourier transformation yields

$$G^R(\boldsymbol{k},\varepsilon) = \int_0^\infty d\varepsilon' \{\frac{A^+(\boldsymbol{k},\varepsilon)}{\varepsilon - \varepsilon' - \mu + i\delta} + \frac{A^-(\boldsymbol{k},\varepsilon)}{\varepsilon + \varepsilon' - \mu - i\delta}\} \tag{4.28}$$

where $A^\pm(\boldsymbol{k},\varepsilon) \geq 0$ and $A^\pm(\boldsymbol{k},\varepsilon) \in \mathbb{R}$. This form is called *Lehman representation*. These spectral functions satisfy the following relation, so-called *sum rule*.

$$\int_0^\infty \{A^+(\boldsymbol{k},\varepsilon') + A^-(\boldsymbol{k},\varepsilon')\} d\varepsilon' = 1 \tag{4.29}$$

Using the relation $1/(x \mp i0^+) = \mathcal{P}(1/x) \pm i\pi\delta(x)$, one can finally obtain the relaiton:

$$\begin{aligned} A^+(\boldsymbol{k},\varepsilon-\mu) &= -\frac{1}{\pi}\Im m[G(\boldsymbol{k},\varepsilon)] \\ A^-(\boldsymbol{k},\mu-\varepsilon) &= +\frac{1}{\pi}\Im m[G(\boldsymbol{k},\varepsilon)], \end{aligned} \tag{4.30}$$

i.e., in condensed matter physics, we can interpret that $A^+(\boldsymbol{k},\varepsilon-\mu)$ is the spectral function of electron and $A^-(\boldsymbol{k},\mu-\varepsilon)$ is that of hole.

Here we focus on the electron's spectral function. Let us get back to the form of the Green's function in Eq. (4.26). In order to separate the contribution of creation and annihilation processes, one can decompose the Green's function using the completeness as well as the orthonormality of eigenvectors $\sum_n |\Psi_n^{N-1}\rangle\langle\Psi_n^{N-1}| = 1$ and $\sum_n |\Psi_n^{N+1}\rangle\langle\Psi_n^{N+1}| = 1$ as

$$\begin{aligned} G^R(\boldsymbol{k},t) &= \frac{1}{i\hbar}\theta(t)\sum_n \langle\Psi_g^N|\hat{c}_{\boldsymbol{k}}(t)|\Psi_n^{N+1}\rangle\langle\Psi_n^{N+1}|\hat{c}_{\boldsymbol{k}}^\dagger|\Psi_g^N\rangle \\ &\quad + \frac{1}{i\hbar}\theta(t)\sum_n \langle\Psi_g^N|\hat{c}_{\boldsymbol{k}}^\dagger|\Psi_n^{N-1}\rangle\langle\Psi_n^{N-1}|\hat{c}_{\boldsymbol{k}}(t)|\Psi_g^N\rangle \\ &= \frac{1}{i\hbar}\theta(t)\sum_n \langle\Psi_g^N|e^{-\mathscr{H}t/i\hbar}\hat{c}_{\boldsymbol{k}}e^{\mathscr{H}t/i\hbar}|\Psi_n^{N+1}\rangle\langle\Psi_n^{N+1}|\hat{c}_{\boldsymbol{k}}^\dagger|\Psi_g^N\rangle \\ &\quad + \frac{1}{i\hbar}\theta(t)\sum_n \langle\Psi_g^N|\hat{c}_{\boldsymbol{k}}^\dagger|\Psi_n^{N-1}\rangle\langle\Psi_n^{N-1}|e^{-\mathscr{H}t/i\hbar}\hat{c}_{\boldsymbol{k}}e^{\mathscr{H}t/i\hbar}|\Psi_g^N\rangle \\ &= \frac{1}{i\hbar}\theta(t)\sum_n \left|\langle\Psi_n^{N+1}|\hat{c}_{\boldsymbol{k}}^\dagger|\Psi_g^N\rangle\right|^2 e^{-E_g^N t/i\hbar}e^{E_n^{N+1}t/i\hbar} \\ &\quad + \frac{1}{i\hbar}\theta(t)\sum_n \left|\langle\Psi_n^{N-1}|\hat{c}_{\boldsymbol{k}}^\dagger|\Psi_g^N\rangle\right|^2 e^{-E_g^N t/i\hbar}e^{E_n^{N-1}t/i\hbar} \end{aligned} \tag{4.31}$$

where $\mathscr{H}$ is the Hamiltonian of the system. By Fourier transformation with respect

to t, the Green's function would be

$$
\begin{aligned}
G^R(\boldsymbol{k},\varepsilon) &= \frac{1}{i\hbar}\int_0^\infty dt \langle \Psi_g^N | \hat{\mathscr{T}}[\hat{c}_{\boldsymbol{k}}(t)\hat{c}_{\boldsymbol{k}}^\dagger] | \Psi_g^N \rangle e^{i(\varepsilon+Ei0^+)t/\hbar} \\
&= \frac{1}{i\hbar}\sum_n \left|\langle \Psi_n^{N+1}|\hat{c}_{\boldsymbol{k}}^\dagger|\Psi_g^N\rangle\right|^2 \int_0^\infty dt e^{-E_n^{N+1}t/i\hbar} e^{E_g^N t/i\hbar} e^{i(\varepsilon+Ei0^+)t/\hbar} \\
&\qquad + \frac{1}{i\hbar}\sum_n \left|\langle \Psi_n^{N-1}|\hat{c}_{\boldsymbol{k}}|\Psi_g^N\rangle\right|^2 \int_0^\infty dt e^{-E_n^{N-1}t/i\hbar} e^{E_g^N t/i\hbar} e^{i(\varepsilon+Ei0^+)t/\hbar} \\
&= \sum_n \frac{\left|\langle \Psi_n^{N+1}|\hat{c}_{\boldsymbol{k}}^\dagger|\Psi_g^N\rangle\right|^2}{\varepsilon + i0^+ - E_n^{N+1} + E_g^N} + \sum_n \frac{\left|\langle \Psi_n^{N-1}|\hat{c}_{\boldsymbol{k}}|\Psi_g^N\rangle\right|^2}{\varepsilon + i0^+ + E_n^{N-1} - E_g^N} \\
&= \sum_n \left|\langle \Psi_n^{N+1}|\hat{c}_{\boldsymbol{k}}^\dagger|\Psi_g^N\rangle\right|^2 \left\{ \frac{\mathcal{P}}{\varepsilon - E_n^{N+1} + E_g^N} - i\pi\delta(\varepsilon - E_n^{N+1} + E_g^N) \right\} \\
&\qquad + \sum_n \left|\langle \Psi_n^{N-1}|\hat{c}_{\boldsymbol{k}}|\Psi_g^N\rangle\right|^2 \left\{ \frac{\mathcal{P}}{\varepsilon + E_n^{N-1} - E_g^N} - i\pi\delta(\varepsilon + E_n^{N-1} - E_g^N) \right\}
\end{aligned}
\tag{4.32}
$$

where, $\mathcal{P}$ denotes the Cauchy's principal value, and the relation $1/(x \mp i0^+) = \mathcal{P}(1/x) \pm i\pi\delta(x)$ is utilized on the calculations above. Then, the single-particle spectral function $A(\boldsymbol{k},\epsilon)$ is given by taking the imaginary part of the Green's function as below.

$$
\begin{aligned}
A^+(\boldsymbol{k},\varepsilon) &= -\frac{1}{\pi}\Im m[G^R(\boldsymbol{k},\varepsilon)] \\
&= \sum_n |\langle \Psi_n^{N+1}|\hat{c}_{\boldsymbol{k}}^\dagger|\Psi_g^N\rangle|^2 \delta(\varepsilon - E_n^{N+1} + E_g^N) \\
&\qquad + \sum_n |\langle \Psi_n^{N-1}|\hat{c}_{\boldsymbol{k}}|\Psi_g^N\rangle|^2 \delta(\varepsilon + E_n^{N-1} - E_g^N) \\
&= A^{\varepsilon \geq E_F}(\boldsymbol{k},\varepsilon) + A^{\varepsilon \leq E_F}(\boldsymbol{k},\varepsilon)
\end{aligned}
\tag{4.33}
$$

The first term corresponds to the spectral function of the angle-resolved inverse photoemission (IPES) spectrum, whereas the second term does the spectral function of angle-resolved photoemission (ARPES) spectrum.

Self-energy

The temperature Green's function (also known as Matsubara Green's function) $\mathscr{G}_\sigma(\boldsymbol{k},\tau)$ is defined by

$$
\mathscr{G}_\sigma(\boldsymbol{k},\tau) = -\langle \hat{\mathscr{T}}_\tau[c_{\boldsymbol{k}\sigma}(\tau)c_{\boldsymbol{k}\sigma}^\dagger]\rangle^{\mathrm{GC}} \tag{4.34}
$$

where τ is the imaginary time, $A(\tau) = e^{\mathscr{H}\tau}Ae^{-\mathscr{H}\tau}$ with $\hat{\mathscr{H}} = \hat{\mathscr{H}}_0 + \hat{\mathscr{H}}_{\mathrm{int}}$, and $\langle\cdots\rangle^{\mathrm{GC}}$ is the grand canonical average. The advantage of this Green's function is

that the perturbation calculation can be simplified due to the Bloch-De Dominics theorem. Taking the partial derivative with respect to τ, one can obtain

$$\frac{\partial}{\partial\tau}\mathscr{G}(\boldsymbol{k},\tau) = -\xi_k\mathscr{G}(\boldsymbol{k},\tau) - \langle\hat{\mathscr{T}}_\tau[\hat{\mathscr{H}}_{\text{int}}, c_{\boldsymbol{k}\sigma}(\tau)]c^\dagger_{\boldsymbol{k}\sigma}]\rangle^{\text{GC}} - \delta(\tau) \tag{4.35}$$

where $\xi_k = \varepsilon_k - \mu$. When $\hat{\mathscr{H}}_{\text{int}} = 0$, Fourier transformation with respect to τ follows

$$\mathscr{G}_0(\boldsymbol{k}, i\omega_l) = \frac{1}{i\omega_l - \xi_k}. \tag{4.36}$$

The retarded Green's function can be deduced by analytic continuation in complex frequency plane as

$$G^R(\boldsymbol{k},\omega) = \mathscr{G}(\boldsymbol{k}, i\omega_l \to \varepsilon + i0^+) \tag{4.37}$$

and therefore the spectral function can be obtained by

$$A^+(\boldsymbol{k},\varepsilon) = -\frac{1}{\pi}\Im m[\mathscr{G}_0(\boldsymbol{k}, i\omega_l \to \varepsilon + i0^+)] = \delta(\varepsilon - \xi_{\boldsymbol{k}}), \tag{4.38}$$

and this is Koopmans theorem itself.

On the other hand, when we take non-zero $\hat{\mathscr{H}}_{\text{int}}$ into account, we first define the self-energy $\Sigma(\boldsymbol{k}, \tau - \tau')$ as

$$\langle\hat{\mathscr{T}}_\tau[\hat{\mathscr{H}}_{\text{int}}, c_{\boldsymbol{k}\sigma}(\tau)]c^\dagger_{\boldsymbol{k}\sigma}]\rangle^{\text{GC}} \equiv \int_0^\beta d\tau'\Sigma(\boldsymbol{k},\tau-\tau')\mathscr{G}(\boldsymbol{k},\tau'). \tag{4.39}$$

Substituting this self-energy into Eq. (4.35), the equation of motion of the Green's function becomes

$$\int_0^\beta d\tau'[\delta(\tau-\tau')(-\frac{\partial}{\partial\tau'} - \xi_k) - \Sigma(\boldsymbol{k},\tau-\tau')]\mathscr{G}(\boldsymbol{k},\tau') = \delta(\tau). \tag{4.40}$$

Fourier transformation of the equation above with respect to τ follows

$$\mathscr{G}(\boldsymbol{k}, i\omega_l) = \frac{1}{i\omega_l - (\xi_k + \Sigma(\boldsymbol{k}, i\omega_l))}, \tag{4.41}$$

that has the same form as non-interacting system as in Eq. (4.36) but with the energy correction by self-energy. Equation (4.41) is called *Dyson's equation*, and its diagrammatic representation is shown in Figure 4.2 (a). All the irreducible diagrams are included in the self-energy part Σ, $\varepsilon_{\boldsymbol{k}}$ denotes the bare-particle energy with momentum $\boldsymbol{k}$. Evaluating the self-energy is equivalent to solving the many-body Schrödinger equation. The corresponding spectral function can be deduced in a similar manner as

$$\begin{aligned} A^+(\boldsymbol{k},\varepsilon) &= -\frac{1}{\pi}\Im m[\mathscr{G}(\boldsymbol{k}, i\omega_l \to \varepsilon + i0^+)] \\ &= -\frac{1}{\pi}\frac{\Im m[\Sigma(\boldsymbol{k},\varepsilon)]}{\{\varepsilon - \xi_{\boldsymbol{k}} - \Re e[\Sigma(\boldsymbol{k},\varepsilon)]\}^2 + \{\Im m[\Sigma(\boldsymbol{k},\varepsilon)]\}^2} \end{aligned} \tag{4.42}$$

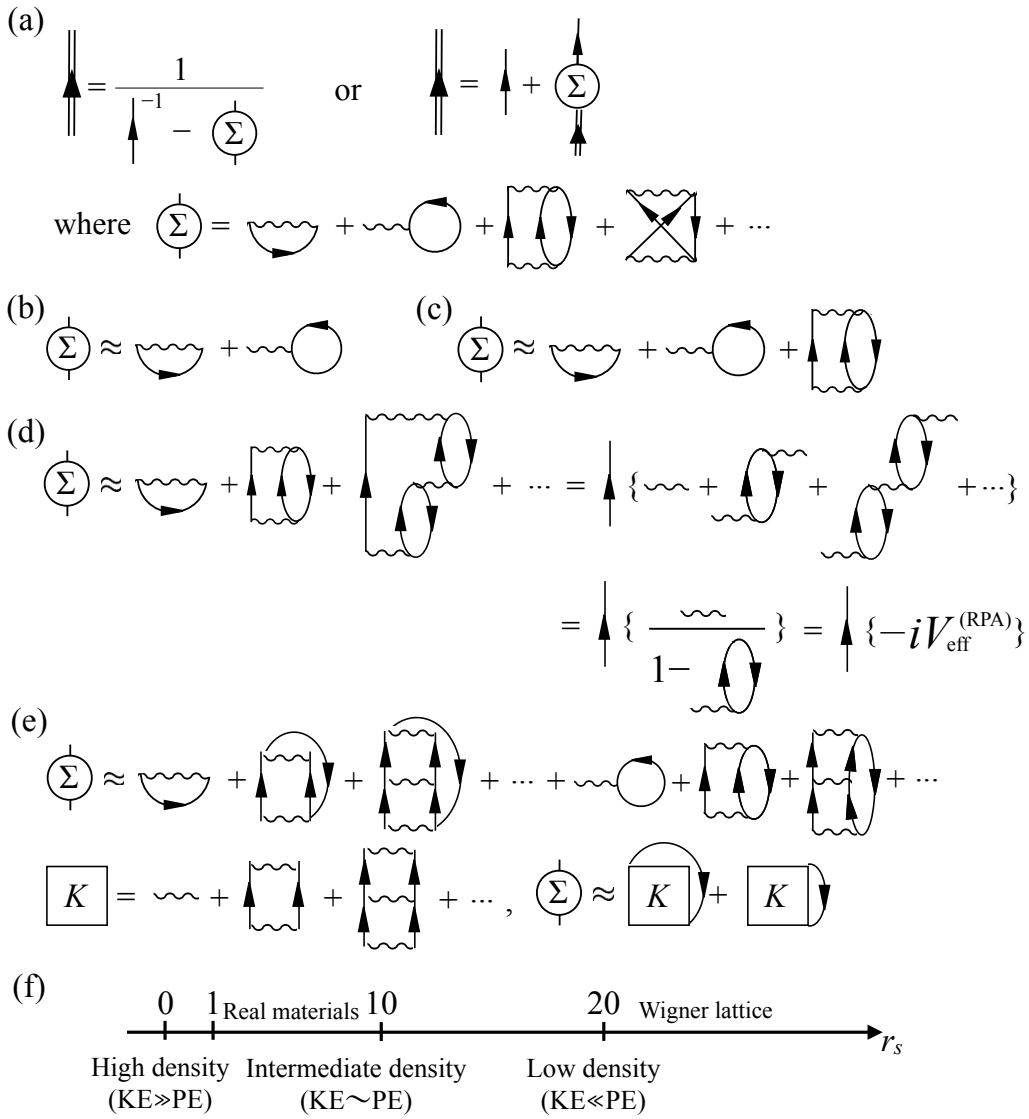

Figure 4.2: Diagrammatic representation of (a) Dyson's equation and its self-energy: irreducible diagrams, (b) self-energy within Hartree-Fock scheme, and (c) self-energy within single pair-bubble approximation, (d) self-energy within random phase approximation and its effective interaction, (e) self-energy within ladder approximation and K-matrix representation, and (f) the relation between density and a parameter r_s. KE and PE represent kinetic energy and potential energy, respectively.

Partial sum method

It is impossible to evaluate the exact self-energy *i.e.*, to take all the interaction into account, but there are several good approximations, which provide the effective mass, self-energy, and lifetime of quasi-particles. The method of approximation is called *selective* or *partial* sum [48].

When we take just only the first order of irreducible diagrams (the 'open oyster' and 'bubble' diagrams) as in Figure 4.2 (b), this approximation is called *Hartree-Fock approximation*. The open oyster diagram represents the exchange scattering, and the bubble diagram shows the forward scattering. The energy ε'_k and lifetime τ_k of quasiparticles can be calculated as

$$\varepsilon'_k = \varepsilon_k + \sum_{l \leq k_F} (V_{klkl} - V_{kllk}), \quad \tau_k = \infty \tag{4.43}$$

$$\text{where} \quad V_{klmn} = \int\int \phi^*_k(\boldsymbol{r})\phi^*_l(\boldsymbol{r'})V(|\boldsymbol{r} - \boldsymbol{r'}|)\phi_m(\boldsymbol{r})\phi_n(\boldsymbol{r'})d^3r d^3r'$$

The lifetime here is infinite because of the crudeness of Hartree-Fock approximation.

When we take the first order and one of the second order diagrams (the 'open oyster', 'bubble', and 'ring' diagrams) as self-energy part as in Figure 4.2 (c), this approximation is called *the single pair-bubble approximation*, which is beyond Hartree-Fock approximation. The ring diagram is sometimes called polarization part. The lifetime of quasiparticles can be calculated as

$$\tau_k^{-1} = \Im m \Sigma(\boldsymbol{k}, \omega) \propto (\varepsilon_k - \varepsilon_F)^2 \tag{4.44}$$

i.e., the lifetime here is finite. Moreover, this equation implies that the quasi-particle description is effective only near Fermi wave number.

Electron gas is characterized by a single parameter r_s, and is defined as

$$\frac{1}{n} = \frac{4}{3}(r_s a_0)^3 \tag{4.45}$$

where n is electron density, a_0 is Bohr radius. For high density (long-range interaction system) electron gas, where the kinetic energy is much greater than the potential energy, *random phase approximation* (RPA) can be applied. In this approximation, self-energy part is selected as the summation of pair-bubble as in Fig. 4.2(d). The effective interaction within RPA $V_{\text{eff}}^{\text{RPA}}$ can be calculated as

$$V_{\text{eff}}^{\text{RPA}}(q) = \frac{4\pi e^2}{q^2 + \lambda^2} \quad \text{or} \quad V_{\text{eff}}^{\text{RPA}}(r) \propto \frac{e^2}{r}\exp(-\lambda r) \tag{4.46}$$

i.e., the shielded Coulomb potential (also known as Yukawa potential) is deduced. Note that all the diagrams except bubble and open oyster are divergent but sum of

pair-bubbles is finite. Since all the diagrams can be arranged as a power series of r_s, small r_s is needed to converge the series: RPA is good for high density.

For low density system (small $n \sim k_F^3$), k_F is small: hole contribution is much weaker than particle contribution. In terms of diagrammatic language, the dominant diagrams are those with the least number of hole lines as in Figure 4.2 (e). This approximation is called *ladder approximation*. Then the lifetime is given by

$$\tau_k^{-1} = \frac{1}{\pi} k_F^2 a^2 (k - k_F)^2 \tag{4.47}$$

where a is the effective distance of short-range repulsive force.

Effects of self-energy on photoemission process

When the electron-electron interaction is not negligible, it influences on the band dispersion; the real part gives energy shifts while the imaginary part gives broadening of peak width as seen in Eq. (4.42). Besides it will affect the effective mass (mass renormalization) when it can be described within the Fermi liquid theory. The energy eigenvalue is given by

$$\begin{aligned} &\varepsilon - \varepsilon_{\boldsymbol{k}} - \Re e\Sigma(\boldsymbol{k}, \varepsilon) = 0 \\ \Leftrightarrow\ &\varepsilon = \varepsilon_{\boldsymbol{k}}^* = z_k(\varepsilon_{\boldsymbol{k}} - \mu) + \mu \end{aligned} \tag{4.48}$$

where the renormalization factor z_k is given by

$$z_{\boldsymbol{k}} = \left(1 - \frac{\partial \Re e\Sigma(\boldsymbol{k}, \varepsilon)}{\partial \varepsilon}\Big|_{\varepsilon=\mu}\right)^{-1} < 1. \tag{4.49}$$

In the vicinity of $\varepsilon = \mu$, $\Sigma(\boldsymbol{k}, \varepsilon)$ can be expanded as

$$\Sigma(\boldsymbol{k}, \varepsilon) \approx \Re e\Sigma(\boldsymbol{k}, \mu) + \frac{\partial \Re e\Sigma(\boldsymbol{k}, \varepsilon)}{\partial \varepsilon}\Big|_{\varepsilon=\mu} (\varepsilon - \mu) + i\Im m\Sigma(\boldsymbol{k}, \varepsilon_{\boldsymbol{k}}^*). \tag{4.50}$$

Plugging this expansion into Eq. (4.42), the spectral function can be expressed as

$$A(\boldsymbol{k}, \varepsilon) \approx -\frac{z_{\boldsymbol{k}}}{\pi} \frac{z_{\boldsymbol{k}} \Im m\Sigma(\boldsymbol{k}, \varepsilon)}{[\varepsilon - \mu - z_{\boldsymbol{k}}(\varepsilon - \mu)]^2 + \{z_{\boldsymbol{k}} \Im m\Sigma(\boldsymbol{k}, \varepsilon)\}^2}, \tag{4.51}$$

i.e., the band has its peak at $\varepsilon = \varepsilon_{\boldsymbol{k}}^*$, and it is shrunk by the factor of $z_{\boldsymbol{k}}$. In other words, the effective mass of quasi-particle m^* increases by the factor of $z_{\boldsymbol{k}}^{-1}$ compared with bare band mass m_b, which is defined by

$$m_b = \left(\frac{1}{k}\frac{d\varepsilon_{\boldsymbol{k}}}{d\boldsymbol{k}}\Big|_{\boldsymbol{k}=\boldsymbol{k}_F}\right)^{-1}. \tag{4.52}$$

The lifetime of quasi particle is given by

$$\frac{\hbar}{\tau_{\boldsymbol{k}}} \approx -2z_{\boldsymbol{k}} \Im m\Sigma(\boldsymbol{k}, \varepsilon_{\boldsymbol{k}}^*). \tag{4.53}$$

Note that the quasi-particle can only be defined within

$$-2z_{\boldsymbol{k}} \Im m\Sigma(\boldsymbol{k}, \varepsilon) < |\varepsilon - \mu|. \tag{4.54}$$

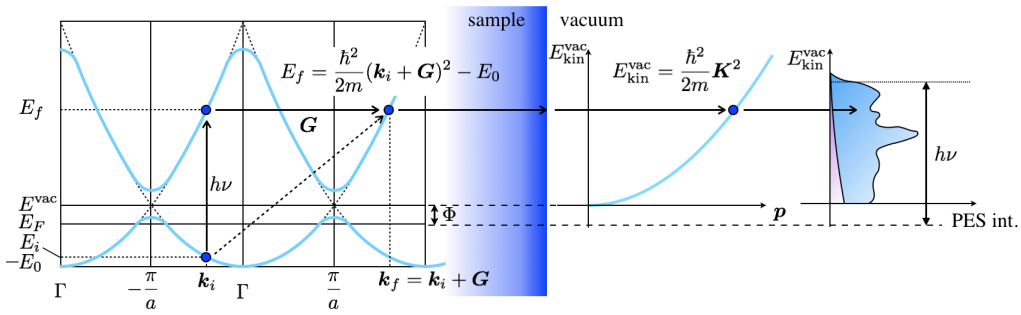

Figure 4.3: Kinematics of the photoemission process within the three-step model; direct optical transition to free-electron state in solid, transportation to the surface, and free-electron final state in vacuum. The corresponding PES intensity is also shown.

4.2.5 Angle-resolved photoemission spectroscopy

ARPES is the technique that one can directly observe the band dispersion below E_F [*i.e.*, spectral function of electron below E_F ;$A^{\varepsilon \leq E_F}(\boldsymbol{k}, \varepsilon)$], Fermi surfaces, and can estimate the mass renormalization. If a certain amount of carrier is doped to a system, it is also possible to estimate the effective carrier concentration using Luttinger theorem [49, 50].

In the photoemission process, electron on a band is excited by a photon ($h\nu$) from initial state (E_i) to final state (E_f), and its energy conservation follows

$$h\nu = E_f - E_i. \tag{4.55}$$

The energy of the free-electron final state inside solid can be expressed as

$$E_f = \frac{\hbar^2}{2m}(\boldsymbol{k_f^2}) - E_0 = \frac{\hbar^2}{2m}(k_\parallel^2 + k_\perp^2) - E_0 \tag{4.56}$$

where the origin of the energy ($E = 0$) was selected at $E = E_F$ When the photoelectron escapes from solid to vacuum, its kinetic energy ($E_{\rm kin}^{\rm vac}$) is

$$E_{\rm kin}^{\rm vac} = E_f - \Phi. \tag{4.57}$$

In the photoexcitation by low-energy photons, the momentum of incident photon $\hbar k_{\rm photon} = h\nu/c$ can be reasonably small compared to the size of the Brillouin zone and thus can be neglected. For instance, photons with the energy of 20 eV have $k_{\rm photon} \sim 0.005$ Å^{-1} whereas the typical size of the Brillouin zone is about 1 Å^{-1}. The momentum (or wave vector) of electron is conserved before and after the photoexcitation process except for the reciprocal lattice vectors. Therefore one can obtain the following momentum conservation in solid

$$\boldsymbol{k}_f = \boldsymbol{k}_i + \boldsymbol{G} \tag{4.58}$$

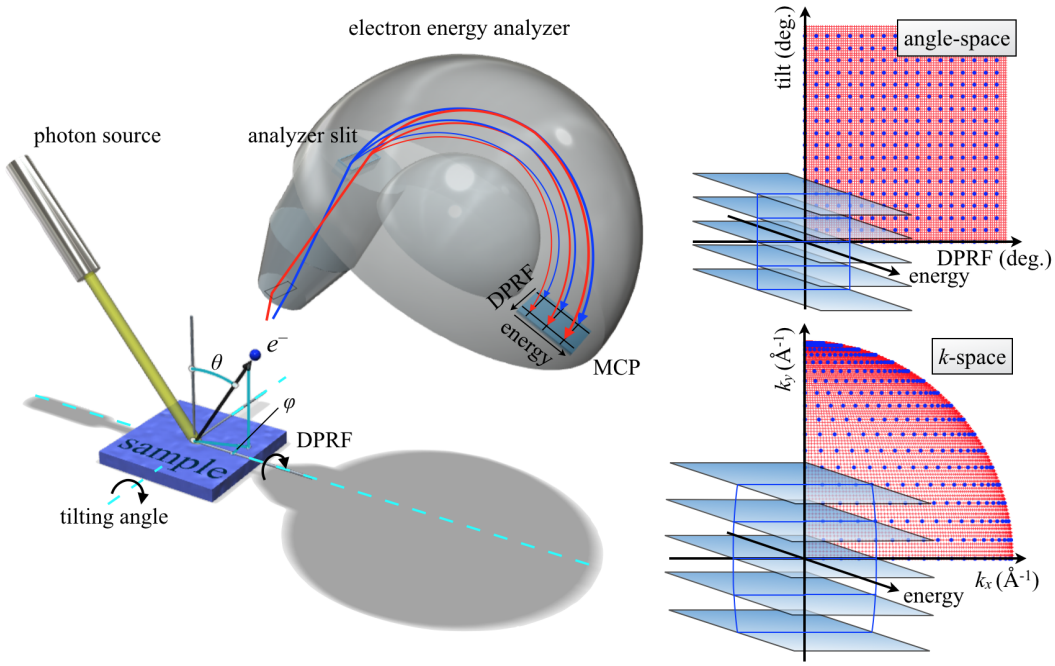

Figure 4.4: Schematic diagram of the geometry of ARPES and the definition of emission angles; polar θ and azimuthal ϕ. Angle space (from 0 to 90 degrees for both θ and ϕ) and k-space are also shown, and solid circles denote each 5-degree step. The schematics with acceptence angle of ± 20 degrees from tilting angle of -20 deg. to $+20$ deg. are overlaid as well.

where $\boldsymbol{k}_i$ ($\boldsymbol{k}_f$) is the initial (final) wave vector and $\boldsymbol{G} = (2n_x\pi/a, 2n_y\pi/b, 2n_z\pi/c)$ is the reciprocal lattice vector ($n_i \in \mathbb{N}, i = x, y, z$). When photoelectron escapes from solid to vacuum, the wave vector parallel to its surface conserves (while the perpendicular components do not) due to the translational symmetry as

$$\boldsymbol{k}_{\parallel} = \boldsymbol{K}_{\parallel} \tag{4.59}$$

where $\boldsymbol{K}$ is the wave vector of electron in vacuum. It can be expressed as follows that the momentum of parallel and perpendicular components of the photoelectron in vacuum;

$$\hbar K_{\parallel} = \sqrt{2mE_{\text{kin}}^{\text{vac}}}\sin\theta, \quad \hbar K_{\perp} = \sqrt{2mE_{\text{kin}}^{\text{vac}}}\cos\theta. \tag{4.60}$$

The argument above is schematically shown in Fig. 4.3, and the emission angle θ is defined in Fig. 4.4.

Using the energy and momentum conservations argued above, one can obtain the following;

$$E_{\text{kin}}^{\text{vac}} + \Phi = E_{\text{kin}}^{\text{vac}}\sin^2\theta + \frac{\hbar^2}{2m}k_{\perp}^2 - E_0 \Leftrightarrow \hbar k_{\perp} = \sqrt{2m(E_{\text{kin}}^{\text{vac}}\cos^2\theta + V_0)} \tag{4.61}$$

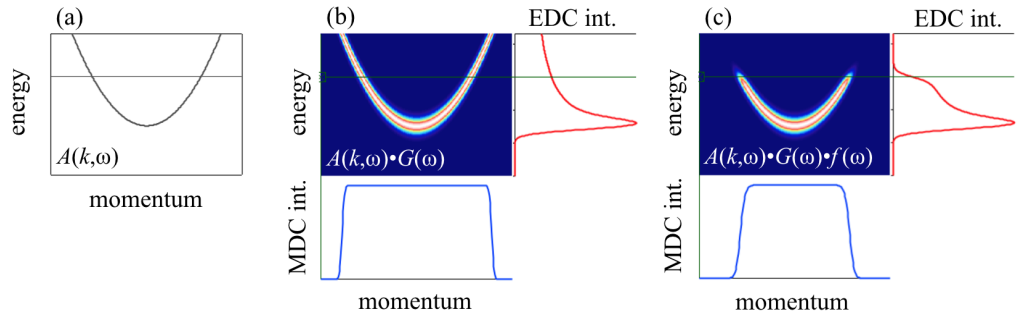

Figure 4.5: (a) Ideal electron-like band crossing E_F with uniform spectral weight and infinite lifetime, (b) with artificial width using Gauss function, and (c) with artificial width using Gauss function and Fermi-Dirac cutoff at finite temperature. Corresponding EDCs and MDCs are shown as well in (b) and (c).

where the parameter $V_0 = E_0 + \Phi$ is the inner potential. Summarizing Eqs. (4.55) to (4.61), one can obtain the both parallel and perpendicular components using the reduced zone scheme as

$$\begin{aligned} \hbar k_{\parallel} &= \sqrt{2m(E_i + h\nu - \Phi)}\sin\theta \\ \hbar k_{\perp} &= \sqrt{2m[(E_i + h\nu - \Phi)\cos^2\theta + V_0]}. \end{aligned} \tag{4.62}$$

Note that V_0 can be determined experimentally, and the method is called *normal emission spectroscopy*. Substituting $\theta = 0$ into Eq. (4.62) follows

$$\hbar k_{\parallel} = 0, \quad \hbar k_{\perp} = \sqrt{2m(E_i + h\nu + E_0)} \tag{4.63}$$

which indicates that one can obtain the band dispersion in the perpendicular direction (*i.e.*, k_z dispersion) by changing the incident photon energy $h\nu$ sequentially. If the band in the k_z direction is dispersive, the inner potential can be also determined.

Polarization dependent ARPES; orbital symmetry selective

In the photoemission process, the transition matrix element $|T_{fi}|$ can be described as

$$|T_{fi}|^2 = ||\langle\phi_f^k|\hat{\varepsilon}\cdot\boldsymbol{r}|\phi_i^k\rangle||^2 \tag{4.64}$$

where ϕ_i^k (ϕ_f^k) is the initial- (final-) state wave function, and $\hat{\varepsilon}$ is the polarization vector of the incident photons as already shown in Eq. (4.15). For high kinetic energy electrons, the wave function of the final state can be approximated by a plane wave $e^{i\boldsymbol{k}\cdot\boldsymbol{r}}$. Using the linearly polarized photons in the horizontal (vertical) direction with respect to the mirror plane, the term $\hat{\varepsilon}\cdot\boldsymbol{r}$ is even (odd), and the corresponding wave function of the initial state should be even (odd) with respect to the mirror plane in order to give nonvanishing $|T_{fi}|$. Therefore, one can select the partial DOS

of odd or even symmetry wave functions. The horizontal and vertical polarization is sometimes called $p-$ and $s-$polarization. Unlike the linear polarization, the dipole selection rule does not hold for circularly polarized photons giving nonzero $|T_{fi}|$ for all the orbitals.

4.2.6 Resonant photoemission spectroscopy

Resonant photoemission spectroscopy is the technique that one can extract a partial DOS of the specific orbital. When the incident energy is tuned to the core-level absorption, not only the direct photoemission but also so-called super Coster-Krönig process occurs. In the case of $4f^N$ electron system for instance, the direct photoemission process can be written as

$$4d^{10}4f^N \xrightarrow{h\nu} 4d^{10}4f^{N-1} + \text{ photoelectron} \tag{4.65}$$

and the corresponding super Coster-Krönig process is

$$4d^{10}4f^N \xrightarrow{h\nu} 4d^{9}4f^{N+1} \xrightarrow{\text{sCK}} 4d^{10}4f^{N-1} + \text{ photoelectron.} \tag{4.66}$$

The schematic diagram of these process is shown in the top of Fig. 4.6. Since the electronic configuration of initial and final states are the same for these processes, the $4f$ states in the photoemission spectrum is strongly enhanced, and therefore one can extract the partial DOS of specific orbital.

The constant initial state (CIS) plot follows a so-called Fano-type resonance, which is derived from configuration interaction between transition to the discrete states ϕ and to the continuum ψ_E with energy E [51, 52]. In the resonant PES process, the discrete ϕ and continuum ψ_E can be interested as core-level self-absorption and direct PES states, respectively. Here we briefly take a look at the simplest case; one discrete and one continuum model. The basis can be taken orthonormally as

$$\langle\phi|\phi\rangle = 1, \quad \langle\psi_E|\psi'_E\rangle = \delta_{EE'}, \quad \langle\psi_E|\phi\rangle = 0. \tag{4.67}$$

The matrix element of the Hamiltonian is given by

$$\langle\phi|\mathscr{H}|\phi\rangle = E_\phi, \;\; \langle\psi_{E'}|\mathscr{H}|\psi_E\rangle = E\delta(E'-E), \;\; \langle\psi_E|\mathscr{H}|\phi\rangle = V_E. \tag{4.68}$$

The eigenstate of the system can be derived using perturbation theory as

$$\Psi'_E = a\phi + \int dE' b(E')\psi_{E'}. \tag{4.69}$$

The transition matrix element of initial state $|i\rangle$ to perturbed state $|\Psi'_E\rangle$ can be ex-

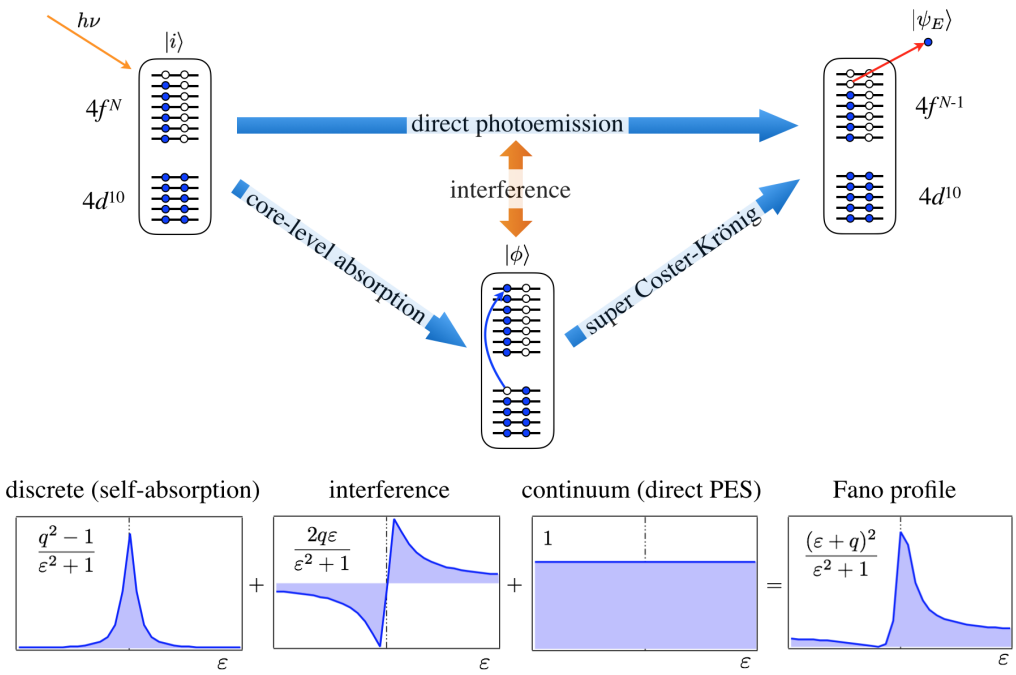

Figure 4.6: Schematic diagram of the resonant photoemission spectroscopy with the case of $4d$-$4f$ resonance. The states $|\phi\rangle$ and $|\Psi\rangle$ represent the discrete and continuous states, respectively. An example of the interpretation of Fano line profile: transition to discrete state, continuum, and discrete/continuum mixing. The parameter q is set to be 3 as an example here.

pressed by using $\hat{T}$ is the transition operator as

$$\begin{aligned}\langle\Psi'_E|\hat{T}|i\rangle =& \frac{1}{\pi V_E^*}\langle\phi|\hat{T}|i\rangle\sin\Delta - \langle\psi_E|\hat{T}|i\rangle\cos\Delta \\ &+ \frac{1}{\pi V_E^*}\mathcal{P}\int dE'\frac{\langle\phi|\mathscr{H}|\psi_{E'}\rangle\langle\psi_{E'}|\hat{T}|i\rangle}{E-E'}\sin\Delta \qquad (4.70)\\ =& \frac{1}{\pi V_E^*}\langle\Phi'|\hat{T}|i\rangle\sin\Delta - \langle\psi_E|\hat{T}|i\rangle\cos\Delta \qquad (4.71)\\ =& \langle\psi_E|\hat{T}|i\rangle\cos\Delta\{\frac{1}{\pi V_E^*}\frac{\langle\Phi'|\hat{T}|i\rangle}{\langle\psi_E|\hat{T}|i\rangle}\tan\Delta - 1\} \qquad (4.72)\end{aligned}$$

where in Eq. (4.70) the first, second, and third terms correspond to self-absorption, direct photoemission, and interference of self-absorption/direct photoemission, respectively, in the resonant photoemission process. The state Φ' in Eq. (4.71) is the discrete state modified by an admixture of states of the continuum;

$$\Phi' = \phi + \mathcal{P}\int dE'\frac{V_{E'}}{E-E'}\psi_{E'}, \qquad (4.73)$$

and the phase shift Δ is given by

$$\Delta = -\arctan \frac{\pi |V(E)|^2}{E - E_\phi - F(E)}, \; F(E) = \mathcal{P} \int dE' \frac{|V_{E'}|^2}{E - E'} \tag{4.74}$$

where the parameter $F(E)$ is the energy correction due to the second-order perturbation. Then the transition probability of initial state $|i\rangle$ to perturbed state $|\Psi'_E\rangle$ can be calculated from Eq. (4.72) as

$$\begin{aligned} \frac{|\langle \Psi'_E|\hat{T}|i\rangle|^2}{|\langle \psi_E|\hat{T}|i\rangle|^2} =& \frac{1}{1+\tan^2\Delta}\{\frac{1}{\pi V_E^*}\frac{\langle \Phi'|\hat{T}|i\rangle}{\langle \psi_E|\hat{T}|i\rangle}\tan\Delta - 1\}^2 \\ =& \frac{1}{1+(-1/\varepsilon)^2}\{-\frac{q}{\varepsilon} - 1\}^2 = \frac{(q+\varepsilon)^2}{1+\varepsilon^2} \end{aligned} \tag{4.75}$$

where the parameters q and ε are the modification of discrete state ϕ and reduced energy parameter as follows.

$$\begin{aligned} \varepsilon &= \frac{E - E_\phi - F(E)}{\pi |V_E|^2} = \frac{E - E_\phi - F(E)}{\frac{1}{2}\Gamma} \\ q &= \frac{1}{\pi V_E^*}\frac{\langle \Phi'|\hat{T}|i\rangle}{\langle \psi_E|\hat{T}|i\rangle} \quad \text{or} \quad \frac{1}{2}\pi q^2 = \frac{||\langle \Phi'|\hat{T}|i\rangle||^2}{\Gamma||\langle \psi_E|\hat{T}|i\rangle||^2} \end{aligned} \tag{4.76}$$

Equation (4.75) is known as Fano-type line shape, that shows a strong enhancement around $\varepsilon = 0$. The interpretation of this equation is the superposition of direct photoemission, core-level absorption, and quantum-mechanical interference between them, which is also schematically shown in Fig. 4.6.

4.2.7 Electron escape depth

PES is a surface-sensitive experimental technique. The escape depth of photoelectrons is determined by electron-electron and electron-phonon interactions. Generally, electron-phonon scattering plays a role only at low energies, namely, below the phonon frequencies. The escape depth of the electrons λ is then determined mainly by electron-electron interaction. The cross-section for electron-electron scattering σ is given by

$$\frac{d^2\sigma}{d\Omega d\omega} = \frac{\hbar^2}{\pi e a_0}\frac{1}{q^2}\Im m\Big\{-\frac{1}{\epsilon(q,\omega)}\Big\}, \tag{4.77}$$

where $\epsilon(q,\omega)$ is the dielectric function, $\hbar q$ is the momentum transfer, and ω is the energy loss of the electron. Although $\epsilon(q,\omega)$ differs from a material to another, the escape depth as a function of energy roughly follows the curve so-called *universal curve*. Except for small energy range ($\geq$10 eV), the electrons in solids can be approximately described by the free-electron gas. In the free electron case, the plasma frequency determines the loss function $\Im m\{-1/\epsilon\}$, and is a function of only the electron density or the mean electron-electron distance r_s and the damping

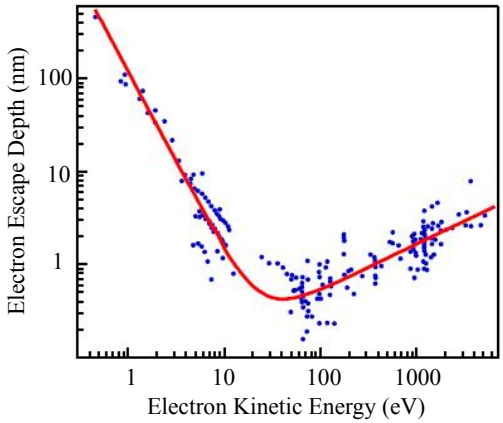

Figure 4.7: Electron escape depth with respect to the kinetic energy of electron [53].

rate of the plasmon alone. The inverse escape depth λ^{-1} can be expressed by r_s, which is roughly material-independent, and one obtains

$$\lambda^{-1} \simeq \sqrt{3}\frac{a_0 R}{E_{\text{kin}}} r_s^{-3/2} \log\Big[\big(\frac{4}{9\pi}\big)^{2/3} \frac{E_{\text{kin}}}{R} r_s^2\Big] \tag{4.78}$$

where a_0 = 0.529Å, $R = 13.6$ eV, and r_s is measured in units of the Bohr radius a_0. This gives us the escape depth as a function of photoelectron kinetic energy E_{kin} shown in Fig. 4.7.

4.3 X-ray absorption spectroscopy

Photon absorption spectroscopy is a strong method to investigate unoccupied states (above the Fermi level) in solids whereas the photoemission spectroscopy is the technique to obtain the information about occupied states (below the Fermi level) as in Figure 4.8. Usually the photon energy is tuned from 500 eV - 500 keV; x-ray region, *i.e.*, the technique is often called x-ray absorption spectroscopy. In a region of 500 eV$\leq$ $h\nu$ $\leq$ 2 keV, the light is classified as soft x-ray. When the photon energy is greater than 2 keV, on the other hand, it is called hard x-ray.

XAS methodology can be roughly divided into four experimental categories that can give complementary results to each other: Metal K-edge, metal L-edge, ligand K-edge, and EXAFS. Each assign of the name of the edges are shown in Tab. 4.1.

4.3.1 General formulation

The photon absorption intensity due to excitation from a core-level electron to unoccupied states is given by

$$\rho^{\text{XAS}}(\varepsilon) \propto \sum_i \sum_n ||\langle \Psi_n'^{N+1} | c_i^\dagger | \Psi_g^N \rangle||^2 \delta(\varepsilon - \varepsilon_{\text{c}} + E_n'^{N+1} - E_g^N) \tag{4.79}$$

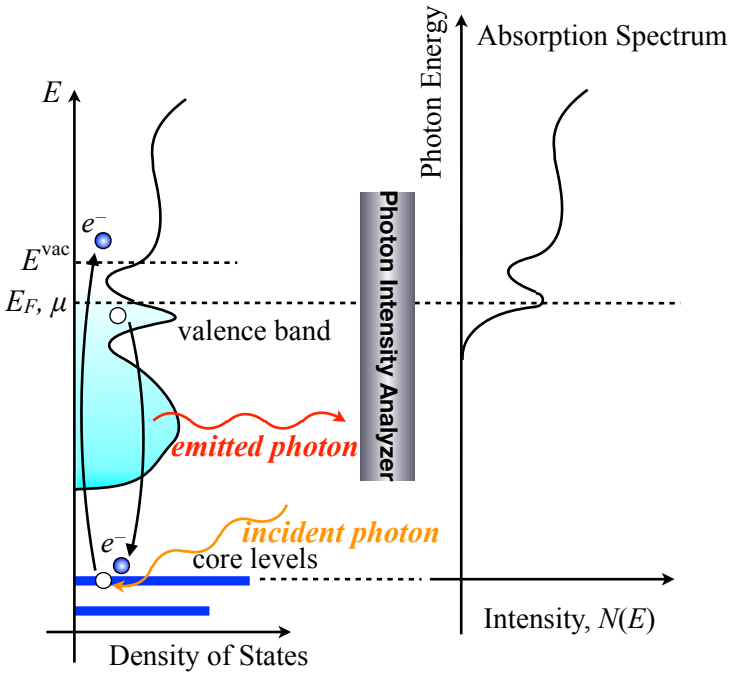

Figure 4.8: Schematic diagrams of the principle of XAS experiment performed by fluorescence-yield mode.

where $E_n'^{N+1}$ and $|\Psi_n'^{N+1}\rangle$ are the eigenvalue and eigenstates of $(N+1)$-electron system interacting with core hole.

4.3.2 Dipole ($E1$) transition

Since the absorption intensity is proportional to the quantity square of

$$\langle f|e\hat{\boldsymbol{r}}|i\rangle = \int \Psi_f^* \, e\hat{\boldsymbol{r}} \, \Psi_i d^3r \tag{4.80}$$

, and the dipole moment operator $e\hat{\boldsymbol{r}}$ has an odd parity, the wave functions of initial and final states which have the different parity will only survive as non-zero terms: otherwise the integral $|\langle f|e\hat{\boldsymbol{r}}|i\rangle|^2$ would go to zero because the function inside the integral has odd parity as long as the initial and final states have the same parity. This reflects *the parity selection rule* due to electric dipole transition. In terms of orbital notation, for instance, $s \to p$ and/or $p \to d$ transition is quite dominant compared with other transitions since the parities of initial and final states are different. Using this parity selection rule combined with the polarization of photon, we can select the orbital anisotropy/angular momentum of the final states.

Linear polarization

When we use the linear polarization, the electric field is

$$\boldsymbol{E}(\boldsymbol{r},t) \propto \boldsymbol{\epsilon}^{\alpha} \exp[i(\boldsymbol{k}\cdot\boldsymbol{x}-\omega t)] \tag{4.81}$$

where $\boldsymbol{\epsilon}^{\alpha}$ ($\alpha = 1$ or 2) stands for a polarization vector with $\boldsymbol{\epsilon}^1 = (1,0,0)$ and $\boldsymbol{\epsilon}^2 = (0,1,0)$. When the photon energy is tuned as the binding energy of K-edge, the transition from s orbital to p orbital occurs. Here we can select the direction of polarization. For instance, if we select the direction of polarization in x or y direction, the transition matrix element is

$$|\langle p|\boldsymbol{r}\cdot\boldsymbol{\epsilon}^1|s\rangle|^2 = |\langle p_x|x|s\rangle|^2 \ \text{ or } \ |\langle p|\boldsymbol{r}\cdot\boldsymbol{\epsilon}^2|s\rangle|^2 = |\langle p_y|y|s\rangle|^2, \tag{4.82}$$

i.e., we can select the orbital anisotropy of the final states.

Circular polarization

When we use the circular polarization, the electric field is

$$\begin{aligned}\boldsymbol{E}(\boldsymbol{r},t) &\propto \boldsymbol{\epsilon}^1 \exp[i(\boldsymbol{k}\cdot\boldsymbol{x}-\omega t)] + \boldsymbol{\epsilon}^2 \exp[i(\boldsymbol{k}\cdot\boldsymbol{x}-\omega t \pm \pi/2)] \\ &= (\boldsymbol{\epsilon}^1 \pm i\boldsymbol{\epsilon}^2)\exp[i(\boldsymbol{k}\cdot\boldsymbol{x}-\omega t)]\end{aligned} \tag{4.83}$$

where the plus (minus) sign denotes the right (left) hand circular polarization. When s and p orbitals are respectively selected as initial and final states, the transition matrix element is

$$|\langle p|\boldsymbol{r}\cdot\frac{\boldsymbol{\epsilon}^1 \pm i\boldsymbol{\epsilon}^2}{\sqrt{2}}|s\rangle|^2 = |\langle p_x \pm ip_y|\frac{x \pm iy}{\sqrt{2}}|s\rangle|^2, \ L_z = \pm 1, \tag{4.84}$$

i.e., we can select the orbital angular momentum of the final states.

4.3.3 Acquisition modes

There are several measurement modes for XAS: transmission mode, total electron yield (TEY) mode, and total/partial fluorescence-yield (TFY,PFY) mode. Typical alignment for hard x-ray measurement system is shown in Fig. **??**. There are three ionization chambers which count I_0, I_1, and I_2 where I_0 and I_1 for the sample, and I_1, and I_2 for the reference sample. There are several different advantages and disadvantages among these modes, which are explained below.

Transmission mode

In the transmission mode experiment, x-ray absorption spectrum is measured by taking the intensity ratio of incident x-ray I_0 and transmitted x-ray I_1 as in Figure 4.9. This method is standard for hard x-rays since soft x-ray strongly interacts with matters and has a large absorption cross-section with atmosphere.

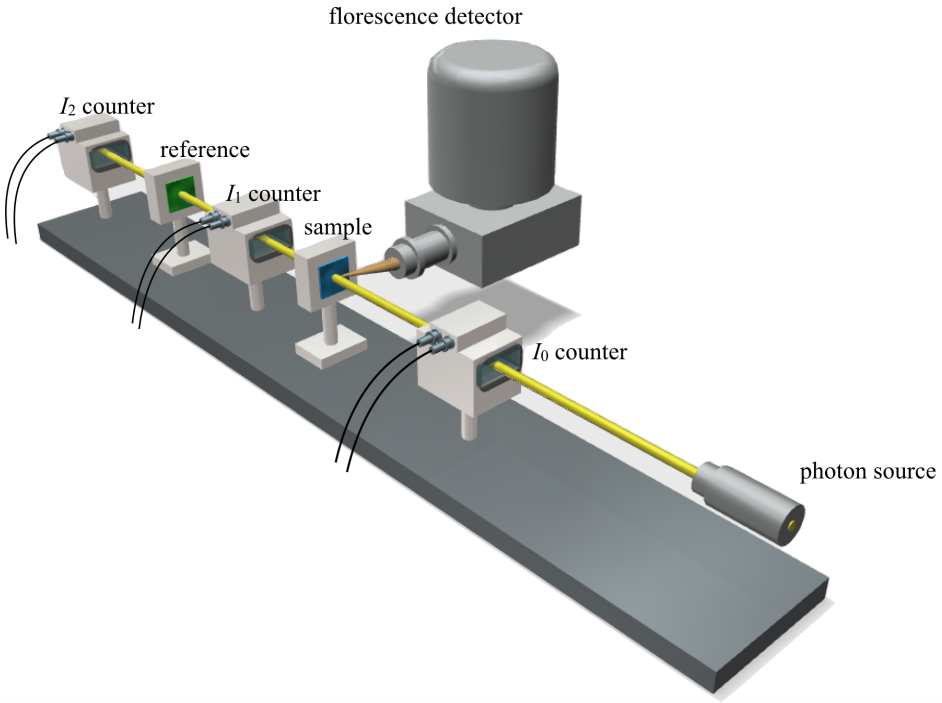

Figure 4.9: Schematic diagrams of typical XAS experimental setup using hard x-ray: transmission mode and fluorescence-yield mode.

Total electron-yield mode

In the total electron-yield mode, x-ray absorption spectrum is measured by the amount of photoelectrons and Auger electrons ,i.e., the amount of electrons which flows into the sample from the earth. In practice, the electric current from the sample to the earth is measured. The TEY mode is more surface sensitive than other modes, and its probing depth is around 5 nm [54]. Since one measures the electric current, TEY mode is not applicable to samples whose resistivities are high.

Fluorescence-yield mode

In the fluorescence-yield mode (FY), x-ray absorption spectrum is measured by the intensity of the fluorescence, which is emitted when photo-excited electrons are de-excited back to the core levels as shown in Figure 4.9. The probing depth of FY mode is about and 200 nm [55]. TFY mode can be utilized for both conducting and insulating samples.TFY mode has however disadvantages that the signal intensity is low and that occasionally the spectral line shape is distorted due to self-absorption effect [56].

In our experiment, we select transmission and FY modes since we used hard x-ray region and the information is more bulk sensitive.

Table 4.1: Nomenclature of each core level in x-ray spectroscopies.

Core state	Spectroscopic name
$1s$	K
$2s$, $2p$	L_1, $L_{2,3}$
$3s$, $3p$, $3d$	M_1, $M_{2,3}$, $M_{4,5}$
$4s$, $4p$, $4d$, $4f$	N_1, $N_{2,3}$, $N_{4,5}$, $N_{6,7}$

5

EXPERIMENTAL SETUPS

In this chapter, all the experimental setups are explained in detail. In this thesis, PES and XAS were performed to investigate the electronic structures of Fe-based and BiS_2-based superconductors.

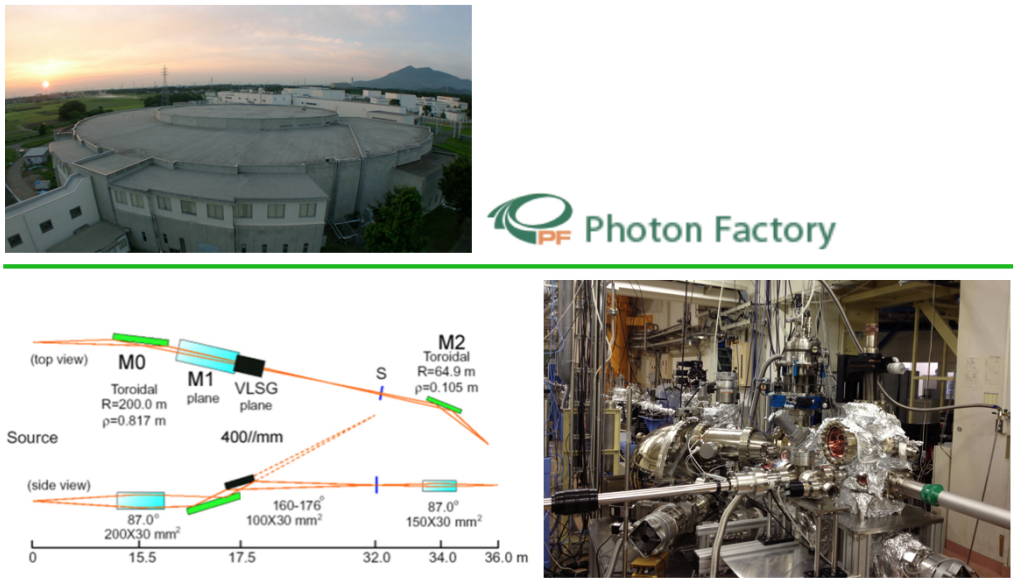

Figure 5.1: The overview of Photon Factory, KEK, and the general view of the endstaion at beamline BL-28A. Schematic diagram of the beamline optics [57] of BL-28A is shown in the left.

5.1 Experimental setups of PES

5.1.1 Photon Factory, KEK, Tsukuba, Japan

Beamline BL-28A

This beamline is the undulator beamline dedicated to angle-integrated and angle-resolved PES using high-flux, highly-circularly polarized VUV (∼30-150eV) radiation emitted from a helical undulator in the HUP and HUN modes. It can also provide high-degree horizontally linear polarization if the insertion device is operated in the linear undulator (LYP) mode. The grating monochromator comprises four gratings, which are interchangeable in situ under UHV. The central beam axis of undulator radiation is extracted by adjusting the vertical and horizontal positions of an aperture of the 4-dimensional slits. The first harmonic energy of undulator radiation can be varied at any time during user runs by changing the undulator's magnet gap from a computer on the experimental station. The energy resolution $E/\Delta E$ ∼500 - 2000, that depends on the slit widths. Photon flux at the first harmonic energy is reported about 10^{11} photons/s as a typical value. The endstation is equipped with SCIENTA 2002 hemispherical anlyzer. Beam size is about 0.5mm (horizontal) $\times$ 0.2 mm (vertical). The overviews of Photon Factory, BL-28A, and the beamline optics are shown in Fig. 5.1.

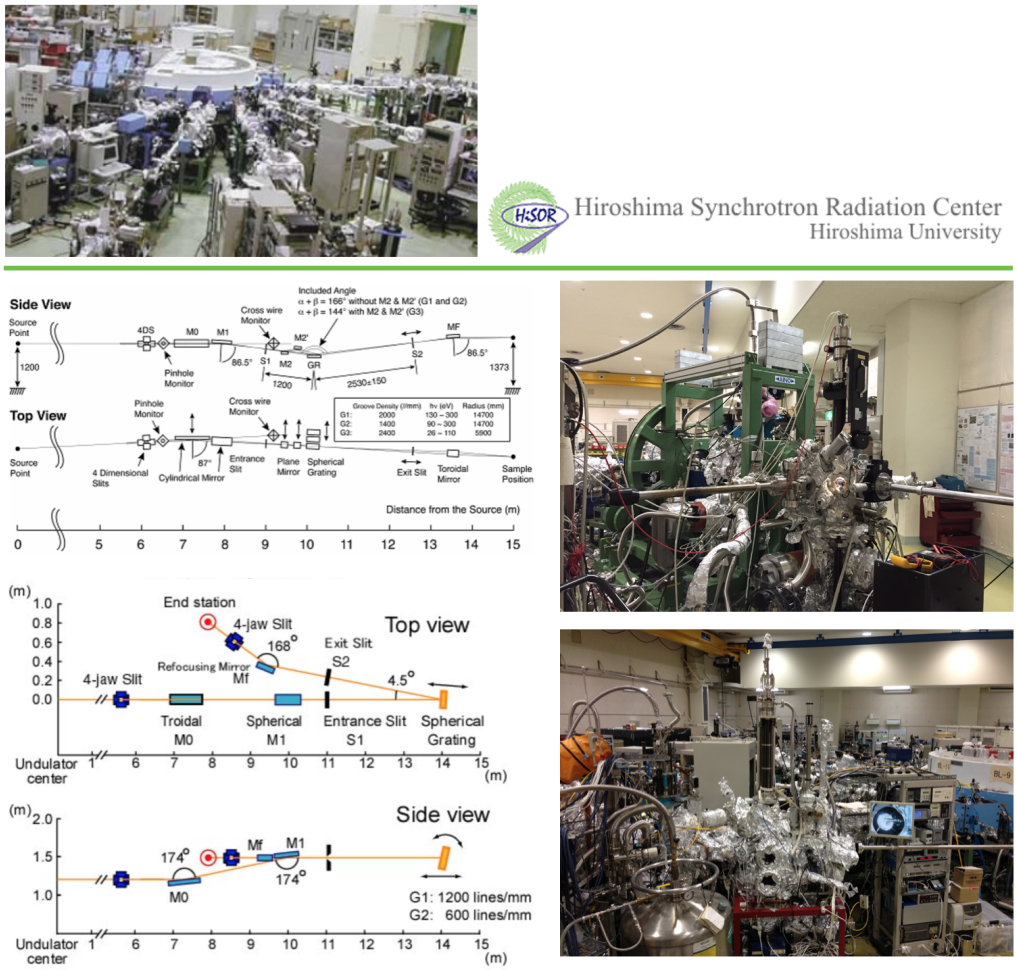

Figure 5.2: The overview of the ring of Hiroshima Synchrotron Radiation Center, Hiroshima University, is shown in the top. The general views of BL-1 and BL-9A are also shown in the middle and bottom. Corresponding beamline optics [58] of BL-1 and BL-9A are shown in the left.

5.1.2 HSRC, Hiroshima University, Hiroshima, Japan

Beamline BL-1 of HiSOR

The BL-1 of Hiroshima Synchrotron Radiation Center is a high-resolution photoemission spectroscopy beamline, and photons are purely linearly polarized due to the 41-period linear undulator installed here. A spherical grating monochromator of so-called Dragon type is equipped, and G1(2000 lines/mm), G2(1400 lines/mm) and G3(2400 lines/mm) provide us photon energies of $h\nu$ =130-300, 90-300 and 26-110 eV, respectively, *i.e.*, ARPES in the vacuum ultraviolet and soft x-ray regions are available. As for the end-station, VG SCIENTA R4000 analyzer is installed, and

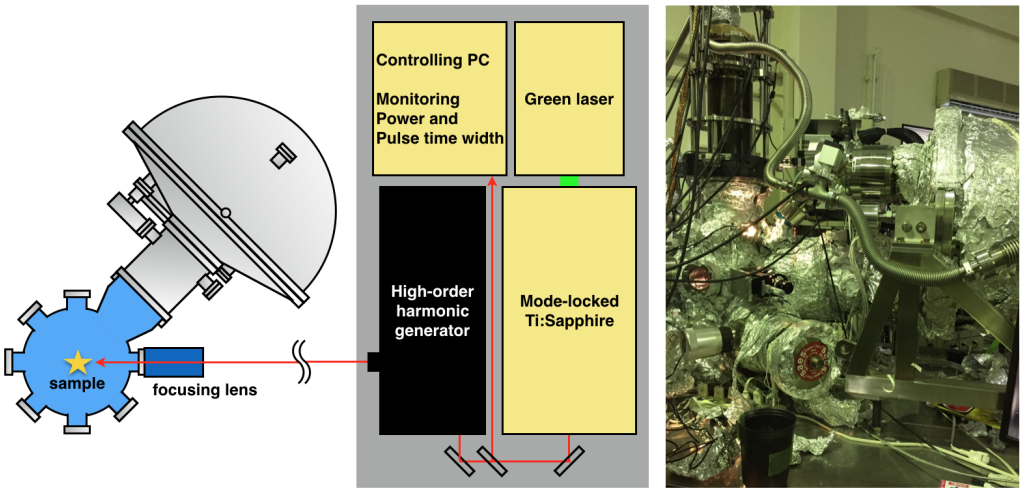

Figure 5.3: Schematic diagram of the laser-ARPES apparatus setups, Hiroshima University. The overview is shown in the right.

the manipulator has six degrees of freedom; x, y, z, DPRF, azimuthal, and tilting angles. The most peculiar aspect of this beamline is how we change the polarization of photons; the entire end-station including the manipulator and the analyzer rotates 90 degrees around the light axis so that a mirror plane also rotates by 90 degrees with respect to the light axis. In other words, one can obtain both s- and p-polarization setups by rotating the end-station. The general view of the endstation and beamline optics are shown in the middle of Fig. 5.2.

Beamline BL-9A of HiSOR

BL-9A is also a high-resolution photoemission spectroscopy beamline, and a 18-period multi-mode undulator is adopted. This multi-mode undulator allows photons polarize both linearly and circularly by optimizing the phase. A normal incident monochromator is mounted with off-plane eagle setup, and two types of grating G1 (Al 600 lines/mm) and G2 (Au 1200 lines/mm) cover photon energies of $h\nu$ =10-40 and 4-12 eV, respectively. As for the end-station, VG SCIENTA R4000 analyzer is installed, and the manipulator has six degrees of freedom; x, y, z, DPRF, azimuthal, and tilting angles. The general view of the endstation and beamline optics are shown in the bottom of Fig. 5.2.

Laser-ARPES apparatus

The photon source of this apparatus is made by green laser, mode-locked Ti:Sapphire, and high-order harmonic generator. Ti:sapphire refers to the lasing medium, a crystal of sapphire Al_2O_3 with doped titanium ions. A Ti:sapphire laser is usually

pumped with another laser, and in this setup, pumped with green laser. Mode-locked oscillators generate ultrashort pulses with a typical duration between a few picoseconds and 10 femtoseconds. Here, mode-locking is a technique in optics by which a laser can be made to produce pulses of light of extremely short duration, on the order of picoseconds or femtoseconds. The basis of the technique is to induce a fixed-phase relationship between the longitudinal modes of the laser's resonant cavity. The laser is then so-called 'phase-locked' or 'mode-locked'. The laser generated by the mode-locked Ti:sapphire goes to the high-order harmonic generator and controlling PC that can monitor the power and pulse time width. At the main chamber, VG SCIENTA R4000 analyzer is equipped. The schematic diagram of the apparatus and the overview are shown in Fig. 5.3.

5.1.3 Elettra, Sycrotrone Trieste, Italy

Spectromicroscopy beamline

The Spectromicroscopy beamline is space-resolved high resolution photoemission beamline. The electron energy analyzer with a mean radius of 40 mm is installed. The acceptance angle is about 16 degrees, and maximum energy resolution is 12.5 meV. The endstation is also equipped with a microscope based on a Schwarzschild objective. This device consists of two spherical mirrors which magnify the beam size down to a submicron scale on the sample. Highly reflective Schwarzschild objective is prepared using periodic multilayer coating. Two objectives are available; at photon energies of 27 eV and 74eV. The smallest achievable beam size on the sample is currently 0.5 μm FWHM [60]. The temperature is available from 20 K up to 450 K. The general view of the endstation and schematic diagram of the optics as well as the enlarged Schwarzschild objective are shown in the bottom of Fig. 5.4.

5.2 Experimental setups of XAS

5.2.1 Elettra, Sycrotrone Trieste, Italy

XAFS beamline

At XAFS beamline, two pairs of entrance W alloy slits define the shape of the beam impinging on the monochromator. The monochromator is a double-crystal Kohzu apparatus. The energy range 2.4 - 27 keV can be covered using interchangeable pairs of Si(111) and Si(311) crystals under vacuum. Two successive Bragg reflections with an inborn energy resolution given by the Darwin angular width gives photons the certain energy parallel to the incoming beam direction with an offset upward by 25 mm. The detuning of the second crystal provides harmonic rejection at energies below 9 keV. At the end-station, three ionization chambers by Oxford

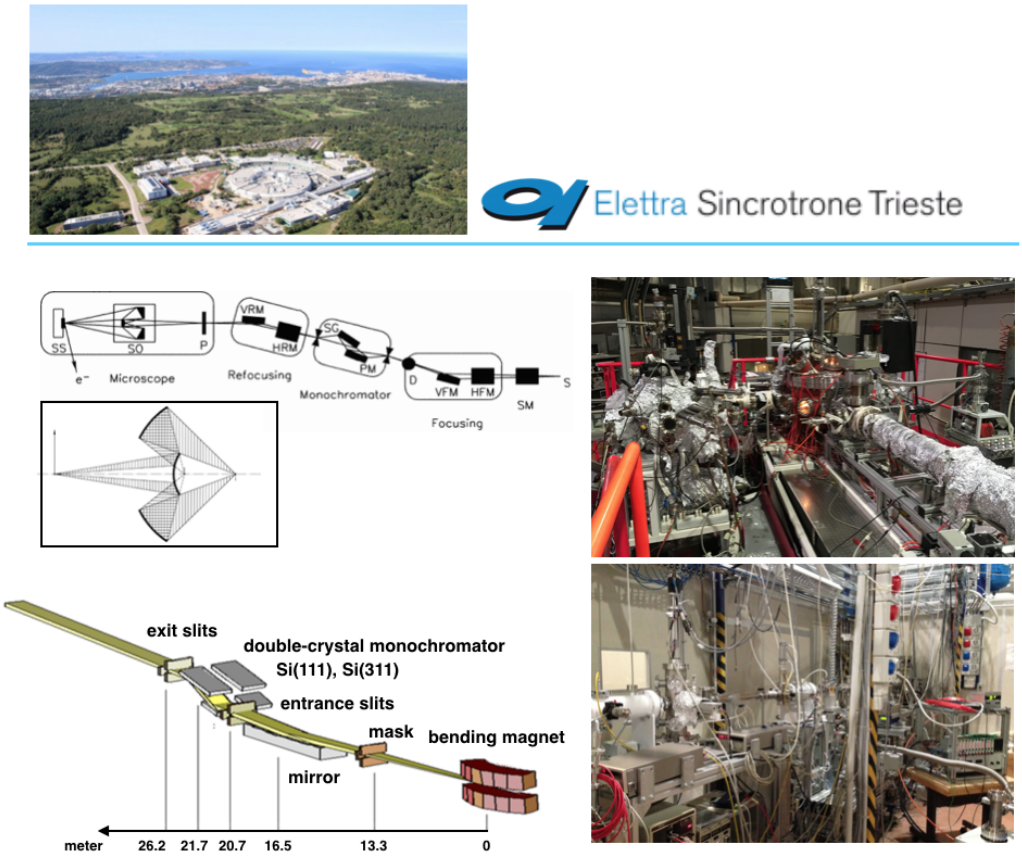

Figure 5.4: The overview of Elettra, Syncrotone Trieste, is shown in the top. The general view of the endstation and schematic diagram of the optics [59] at Spectromicroscopy beamline and XAFS beamline are shown in the bottom.

Instruments are installed for measurements in transmission mode. These chambers are filled with optimal He/N_2/Ar/Kr gas mixture at a total pressure of 2 barr. Three acquisition modes of transmission, fluorescence, and total electron yield are available. The general view of the endstation and schematic diagram of the optics at XAFS beamline are shown in the bottom of Fig. 5.4.

5.2.2 ESRF, The European Synchrotron, Grenoble, France

ID21

At ID21, the scanning x-ray microscope can be operated in the energy range from 2-9 keV, giving access to the K-edges of Phosphorus to Copper, and to the L- and M-edges of some heavier elements for micro-fluorescence and micro-XANES measurements. a double-crystal fixed-exit Si(111) monochromator (Kohzu, Japan)

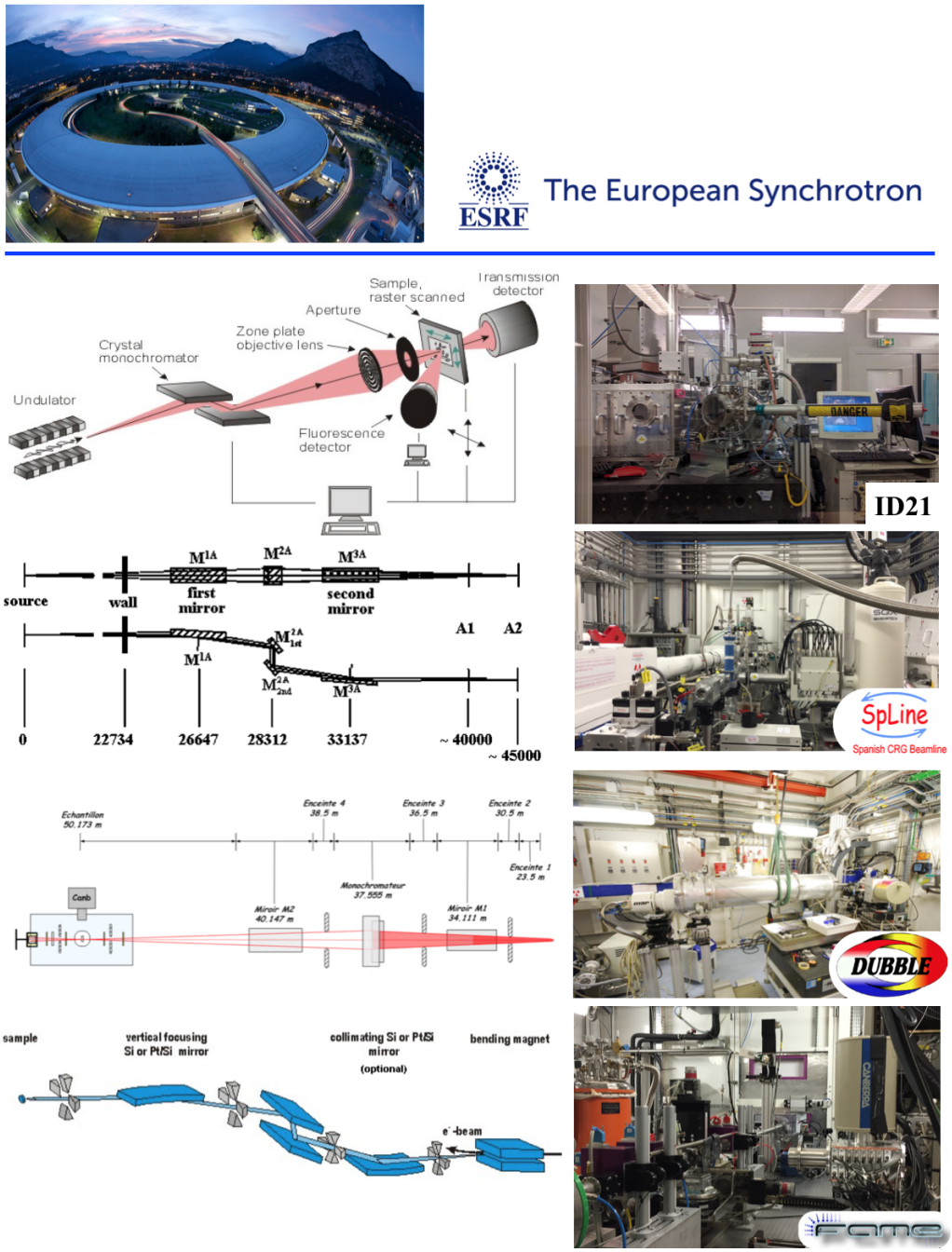

Figure 5.5: *Top*: the overview of the ESRF ring, the European Synchrotron Radiation Facility, Grenoble, whose storage has about 6 GeV electron beam with a maximum current of 200 mA as well as the world's most intense x-ray source. Schematic diagram of the optics [61] and overviews of the endstations at (from the second top to the bottom) space-resolved XANES beamline ID21, BM25A (Spanish beamline, SpLine), BM26A (Dutch-Belgian beamline, DUBBLE), and BM30B (French beamline, FAME), ESRF.

was used for the energy scans. The beam was focused down to a microprobe by a Kirkpatrick-Baez mirror system, that allows us to focus the beam down to 0.35×0.7 μm^2 with a photon flux of 10^{10}-10^{11} photons/s/Si(111). At the endstation, following detectors are available; a single/7-element high purity germanium detector (HpGe) from Princeton Gamma-Tech (US) and the fluorescence detector of a 10 mm^2 silicon drift diode (Röntec, Germany). Transmission signal as well as a full fluorescence spectrum can be recorded for each pixel of the map. Schematic diagram of the optics and overviews of the endstations are shown in Fig. 5.5.

BM25A

At the Spanish beamline BL-25A also known as SpLine, the monochromator has the pseudo channel-cut type with two fixed Si(111) crystals moved together with a simple goniometer circle, in the $(-n, +n)$ configuration. The second crystal is equipped with a piezoelectric driver that allows to change very slightly the Bragg angle (pitch adjustment) in order to reduce the harmonic component of the incident beam, and to keep the transmission of the monochromator constant during long time intervals. At the endstation, a transmission EXAFS spectrometer has been installed before the powder diffractometer. For fluorescence measurements, Si drift detector is available. For transmission experiments photo-diodes, total electron yield, ionization chambers, and gas filled proportional detectors are available. Sample cooling can be done by both liquid He and liquid N_2. Schematic diagram of the optics and overviews of the endstations are shown in the top of Fig. 5.5.

BM26A

At the Dutch-Belgian beamline BM26A as known as DUBBLE beamline, the optics for this branch starts with a collimating mirror with Si and Pt strips. The second optical element is a double-crystal (Si 111) monochromator. This is followed by a meridionally focusing mirror with Si and Pt strips. This mirror can also be operated flat in order to achieve the highest angular-resolution. The energy range that can be achieved by this monochromator is 5-40 keV. Typical amount of photon flux at the endstaion is around 1×10^{11} photons/sec. The energy resolution $\Delta E/E$ is 1.74×10^{-4}. Typical beam size at sample position is (H×V) 5×1 mm^2 and possible maximum size is 8×1.5 mm^2. Schematic diagram of the optics and overviews of the endstations are shown in the middle of Fig. 5.5.

BM30B

At the French beamline BM30B also known as FAME, the monochromator is a double-crystal monochromator using either a pair of Si(111) or Si(220) crystals kept parallel, depending on the necessary energy range, resolution, and/or photon

flux. The energy range of the monochromator is from 4 to 40keV. Size of the beam is 80×3 mm^2. At the endstaion, fluorescence detector (Canberra 30 elements) is equipped at the endstation. Liquid nitrogen and helium cryostats are available. Schematic diagram of the optics and overviews of the endstations are shown in the bottom of Fig. 5.5.

6

ELECTRONIC STRUCTURE OF FE(SE,TE)

In this chapter, the electronic structure of Fe(Se,Te) is discussed. We have performed laser-ARPES on optimally doped FeSe$_{0.4}$Te$_{0.6}$ combined with first principles, and succeeded in resolving the fine orbital states near Γ point. The Fe $3d$ xy/yz orbitals were hybridized due to the spin-orbit interaction. On the other hand, the orbital degeneracy of yz/zx were kept at Γ point even though the spin-orbit interaction is effective. We have also studied electronic structure of Fe(Se,Te) systematically using multi-orbital d-p type Hamiltonian and applied unrestricted Hartree-Fock approximation.

6.1 Introduction

The discovery of superconductivity in Fe pnictides [16] and chalcogenides [62, 63] has stimulated extensive experimental and theoretical investigations on their multi-orbital character.

6.1.1 Spin and orbital fluctuation

In Fe-based systems, it has been proposed that electron-phonon interaction due to the Fe-ion oscillation can induce the critical d-orbital fluctuations using five-orbital Hubbard-Holstein model without being prohibited by the Coulomb interaction with in the random phase approximation (RPA) [64]. The Hubbard-Holstein Hamiltonian is given by

$$\mathscr{H} = -t\sum_{i\sigma}[c^{\dagger}_{i,\sigma}c_{i+1,\sigma}+\text{h.c.}]+U\sum_{i}n_{i\uparrow}n_{i\downarrow}+\omega\sum_{i}b^{\dagger}_{i}b_{i}+g\sum_{i\sigma}n_{i\sigma}(b^{\dagger}_{i}+b_{i}), \quad (6.1)$$

which describes the on-site Coulomb interaction and electron-phonon coupling, and g is the coupling constant, a function of boson Matsubara frequency. The proposed superconducting state without sign reversal (s_{++}-wave state) found a strong ferro-orbital fluctuation when three orbitals of YZ, ZX, and $X^2 - Y^2$ are taken into account [note that they are equivalent to yz, zx, and xy since $YZ(ZX) = \{zx - (+)yz\}/\sqrt{2}$, see Fig. 6.1].

These fluctuations give rise to the strong pairing interaction for the s_{++}-wave state, which is consistent with experimentally observed robustness of superconductivity against impurities. When the magnetic fluctuations due to Coulomb interaction are also strong, the superconducting state showed a smooth crossover from the s-wave state with sign reversal ($s_{\pm}$-wave state) to the s_{++}-wave state as impurity concentration increases as shown in Fig. 6.1. The parameters α_s and α_c are spin and charge Stoner factor, respectively.

Not only phonons, but also Coulomb interaction can drive the orbital-fluctuation-mediated superconductivity from the theoretical point of view [65].

6.1.2 Physical properties of Fe(Se,Te)

Among the Fe-based superconductors, $FeSe_{1-x}Te_x$ has the simplest crystal structure, a maximum $T_c \sim 15$ K [62, 66], and like most of the other Fe-based superconductors, its crystal structure is basically tetragonal. the interest on the $FeSe_{1-x}Te_x$ system has been further stimulated by the very recent findings on the orbital-driven nematicity in FeSe [67–70], the superconductivity above 100 K [71] and the interface electron-phonon coupling [72] in single-layer $FeSe/SrTiO_3$.

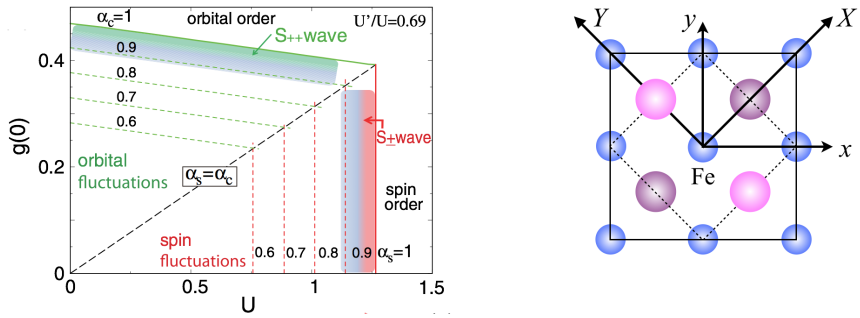

Figure 6.1: U-$g(0)$ phase diagram [64] and xy axes and XY axes in FeAs layer, which is commonly used in the literatures.

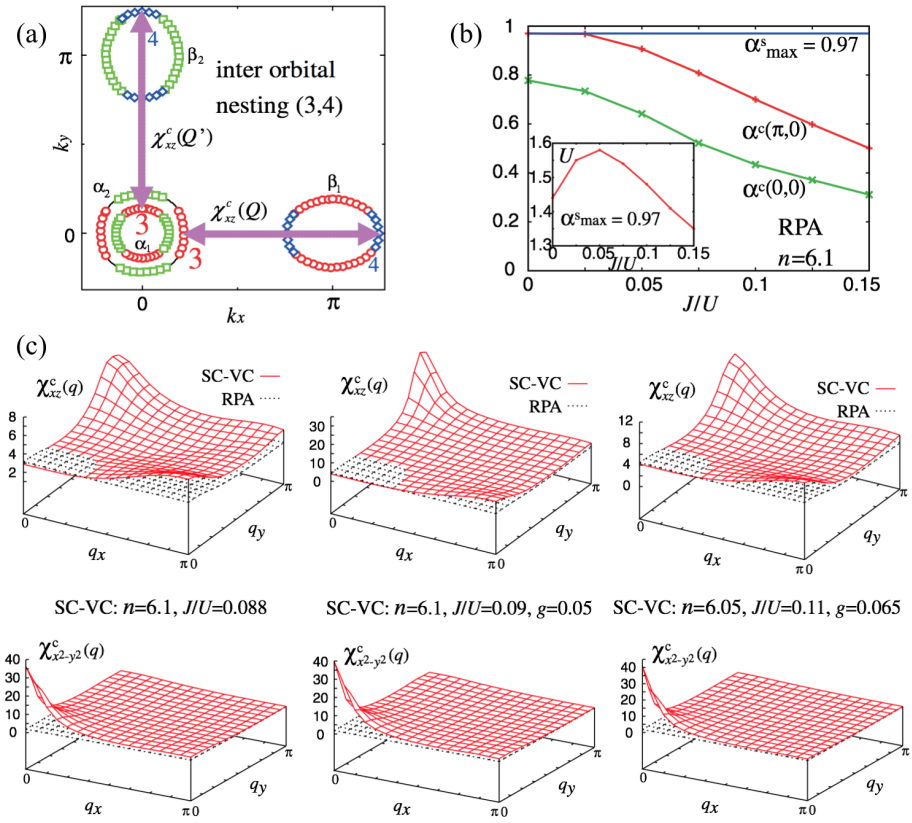

Figure 6.2: (a) Typical Fermi surface of the Fe-based systems where the inter-orbital nesting exists. Green squares are zx, red circles are yz, and blue diamonds are xy. (b) Spin and charge stoner factor as a function of J/U. Inset shows the J/U dependence of U. (c) Charge susceptibility of zx and x^2-y^2 ($\chi^c_{zx}(q)$ and $\chi^c_{x^2-y^2}(q)$) given by the self-consistent vertex correction method [65].

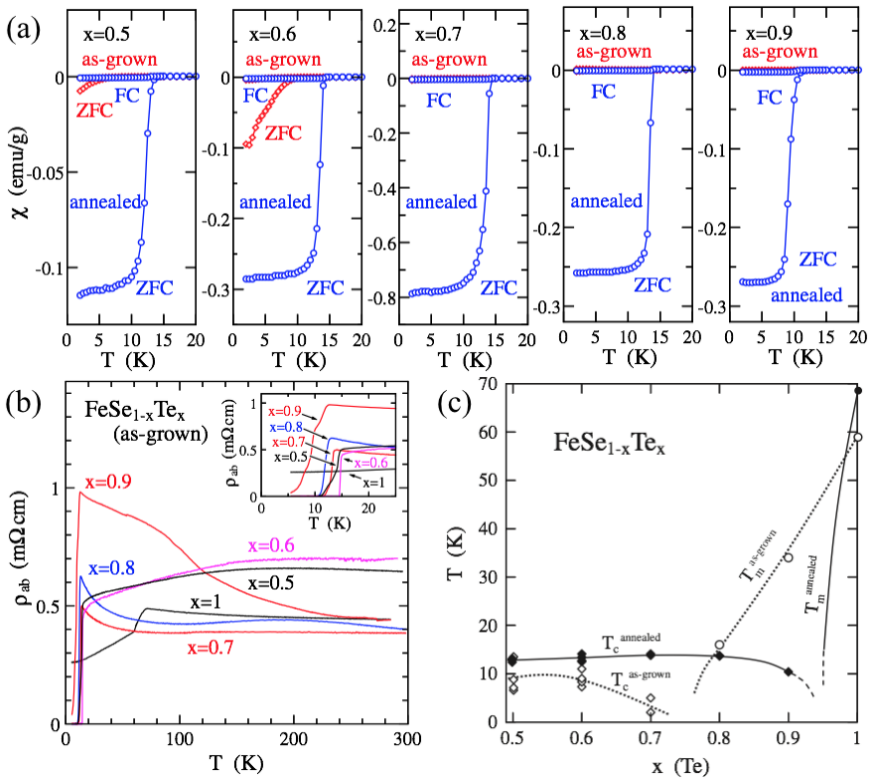

Figure 6.3: Temperature dependence of (a) magnetic susceptibility and (b) in-plane resistivity. (c) Phase diagram of as-grown and annealed $FeSe_{1-x}Te_x$ [66].

Transport properties and annealing effect

Magnetic susceptibility, resistivity, and phase diagram of $FeSe_{1-x}Te_x$ are shown in Fig. 6.3. The annealing treatment (400 ^{o}C for 100 h in vacuum) broadens the superconducting dome and suppresses the AFM phase most likely because of the homogeneous distribution of Se and Te in a crystal [66].

DFT calculation on FeSe and FeTe

Density functional calculation on FeSe and FeTe are shown in Fig. 6.4 [73]. The results showed quite cylindrical Fermi surfaces and an SDW instability in both FeSe and FeTe. However, the strength of the SDW is substantially higher in FeTe as is the size of the Fermi surface. Within the general framework discussed by Subedi *et al.*, FeTe would be expected to have stronger pairing and therefore higher T_c than FeSe.

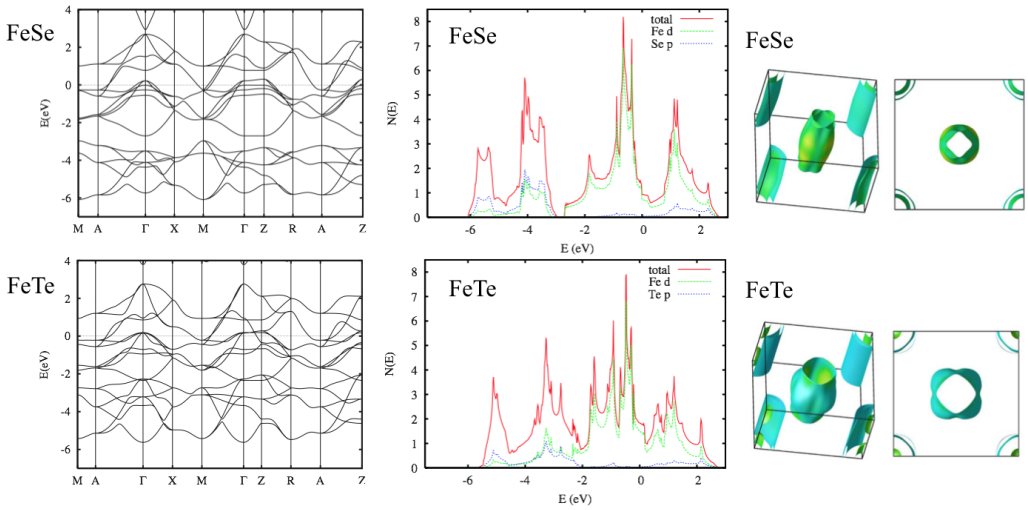

Figure 6.4: Band structures, density of states, and Fermi surfaces of FeSe (top) and FeTe (bottom) from non-spin-polarized LDA calculations. The corners of the Fermi surfaces are Γ points [73].

6.1.3 Orbital characterization

In spite of the apparent simplicity of its crystal structure, the assignment of the orbital character of $FeSe_{1-x}Te_x$ system in ARPES is still controversial. For instance, out of the hole bands observed near the zone center in ARPES, the outermost hole band (which is labeled as γ in literature) forms the large Fermi pocket and is always very weak. This outermost hole band is assigned to xy by Chen *et al.* using polarization dependent ARPES [74], consistent with most of the ARPES studies [75,76], while Tamai *et al.* assign it to yz/zx [77]. The intermediate hole band (labeled as β in literature) forms the small Fermi pocket and is assigned to yz/zx [74] or xy [78]. The inner most band that almost touches the Fermi level (labeled as α in literatures) is assigned to yz/zx [74, 78].

Such a puzzling situation indicates the complexity of the electronic states in $FeSe_{1-x}Te_x$ that has been overlooked in the interpretation of ARPES results.

6.1.4 Analytical problem in ARPES

One of the central questions on the multi-band electronic structure is whether the Fe $3d$ yz/zx degeneracy at the Brillouin zone center is lifted or not, which should be kept in the tetragonal crystal structure. It has been difficult to reveal this issue by ARPES because the α and β bands almost touches Fermi level with finite energy resolutions and FD cutoff. In this situation, when we look at EDCs, it is difficult to distinguish if the peak near E_F is a real structure or just due to FD cutoff. On the

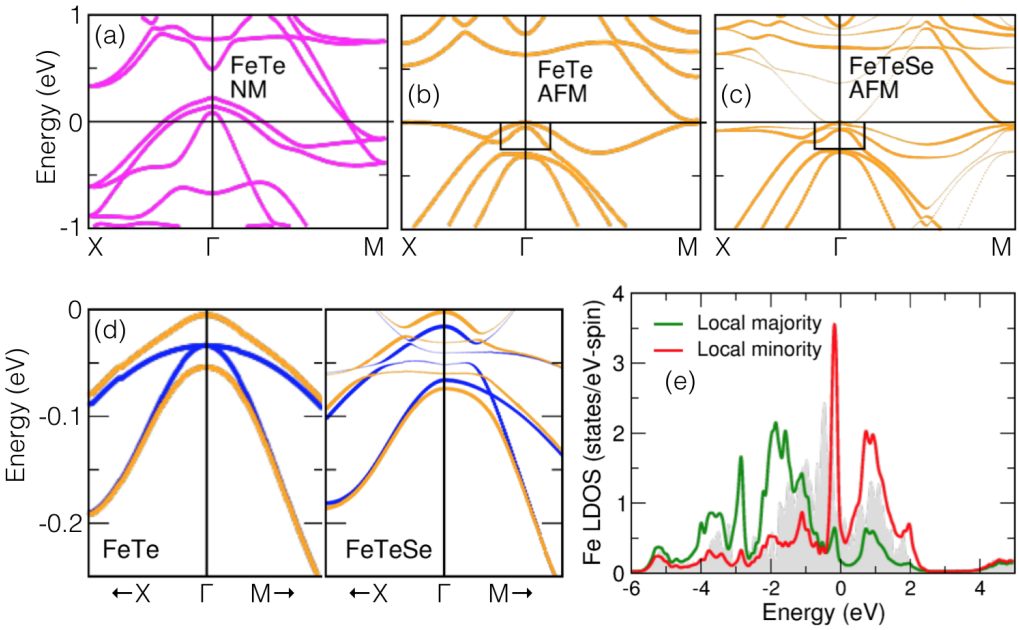

Figure 6.5: (a) Spin-orbit bands along the high-symmetry lines of the Brillouin zone for (a) non-magnetic (NM) FeTe, (b) AFM FeTe, and (c) AFM $FeTe_{0.5}Se_{0.5}$ with the Te and Se in a c(2×2) ordering. (d) Expanded views of the bands around Γ in boxed regions in (b) and (c); bands with spin-orbit coupling are described in orange whereas those without SO in blue, and the size of the dots reflects the k-projection weight. (e) Spin-resolved local Fe density of states for (c); the gray background is the corresponding NM LDOS. [79].

other hand, when we look at MDCs, it is also problematic to track the peak positions because one can never be convinced if the peak is a real structure or just due to the finite energy resolution.

6.1.5 Effects of magnetic ordering and spin-orbit interaction

Johnson *et al.* argued the relatively large spin-orbit interaction on the chalcogenide atoms (especially Te) lifts the degeneracy of the yz and zx orbitals at the zone center while the spin-orbit interaction in the Fe d orbitals alone is not enough to lift the degeneracy to the degree observed [79].

They performed GGA calculation on non-magnetic FeTe, AFM FeTe, and AFM $Fe_2(TeSe)$, and their results are displayed in Figs. 6.5(a)-6.5(c). The band structures with and without spin-orbit coupling near E_F in AFM FeTe and AFM $Fe_2(TeSe)$ are shown in Fig. 6.5(d), that are the expansion of the boxed regions in Figs. 6.5(b) and 6.5(c). In FeTe around Γ point, the bands without spin-orbit coupling for the two spin directions are degenerate because of the fourfold magnetic space group

symmetry relating the two Fe atoms. With spin-orbit coupling included, the states at Γ are split by 60 meV as in Fig. 6.5(d).

In Fe(Te,Se) system, replacing half the Te by Se in each layer introduces a symmetry breaking that already splits the degeneracy at Γ. The splitting at Γ without spin-orbit coupling indicates short-range correlations or orderings are not dominant. With spin-orbit coupling, the splitting at Γ is about the same size as FeTe, but there are now three bands along Γ-M, with the uppermost relatively flat band as in Fig. 6.5(d). The Fe local density of states (LDOS) projected onto different spins are shown in Fig. 6.5(e). They argued that orbital ordering and nematicity appear as a natural consequence of magnetic and spin-orbit interactions in these systems, however, their observation of the α/β splitting at Γ point seems depending on the EDC/MDC analysis.

6.1.6 Motivation

As we already argued, one of the central questions on the multi-band electronic structure is whether the Fe $3d$ yz/zx degeneracy at the Brillouin zone center, which should be kept in the tetragonal crystal structure, is lifted or not due to the electronic nematicity that has been probed by various experimental techniques in the tetragonal region of the phase diagram [80]. Indeed, the Fe $3d$ yz/zx degeneracy, or the degeneracy between the α and β bands at the zone center, is found to be lifted in most of the ARPES studies on the Fe pnictide/chalcogenide superconductors [81]. In order to address this issue experimentally, one has to use a very high resolution apparatus. Therefore, we have performed laser-ARPES on optimally-doped $FeSe_{0.4}Te_{0.6}$ combined with first principles in order to see the effects of spin-orbit interaction, that has been overlooked since the discovery.

Besides, we have performed systematic study on Fe(Se,Te) system using tight binding model analysis.

6.2 Orbital states and spin-orbit interaction in $FeSe_{0.4}Te_{0.6}$ studied by laser-ARPES and first principles

6.2.1 Experimental condition

The ARPES measurements were performed using the laser ARPES apparatus developed at Hiroshima University with 6.4 eV laser as described in Chapter 5. The overall energy resolution including the monochromator and the electron analyzer was set to be 1.7 meV. The angular resolution was $\sim 0.25°$, and its corresponding momentum resolution was 0.003 $Å^{-1}$. The base pressure of the spectrometer was in the 10^{-9} Pa range. We have cleaved the single crystals at 20 K under this ultrahigh

Table 6.1: Summary of the characteristic features using PP or AE.

	PP+PW	AE+PW+SW
number of basis	few	many
core electron calculation	no	yes
reliability	depends on PP	same for all

vacuum in order to obtain a clean (001) surface and took ARPES data at the same temperature within 3 hours after the cleavage. In all the ARPES measurements, the single crystals were properly oriented on the sample stage by the standard Laue measurements and were cooled using a liquid He refrigerator. The Fermi level was determined using the Fermi edge of copper reference signals, that comes from the sample holder. The surface of the holder was scratched under the ultrahigh vacuum in order to obtain the precise Fermi level.

6.2.2 Method of calculation

Band structures of FeTe were calculated within the DFT scheme using Quantum Espresso [82]; we select a plane wave for the basis of the Kohn-Sham equation since it is suitable for calculation with periodic boundary condition (*i.e.*, solids), and pseudopotentials (PPs) are utilized for core-potentials. In the transition-metal $3d$ orbitals, the wave functions are spatially localized because there is no core-electrons that have the same angular momentum. When calculating the localized wave function such as $3d$ orbitals, all-electron (AE) calculation has its limited softenization of pseudo wave function due to the norm conservation condition. Therefore, we select the ultra soft pseudopotential, in which the norm conservation condition is not necessary anymore. Instead, norm conservation condition can be satisfied by adding some compliment when calculating the charge density. The characteristic features of the calculations using PP and AE are summarized in Tab. 6.1.

6.2.3 Results and discussion

Figure 6.6 shows the Fermi surface with the linearly polarized light, integrated with the range of E_F±5 meV. The top of the α band (almost touching E_F) at the zone center and the β Fermi surface are clearly observed. The butterfly-like shape of the β Fermi surface, which is induced by the transition-matrix element effect, is rotated clockwise or counterclockwise depending on the helicity of the circularly polarized light [83]. This indicates that the β Fermi surface is derived from one of the Fe $3d$ yz/zx bands. The intense α band at the zone center should be assigned to the other Fe $3d$ yz/zx band since the suppression of the Fe $3d$ xy band is expected at the zone center due to the odd parity with respect to the yz and zx planes.

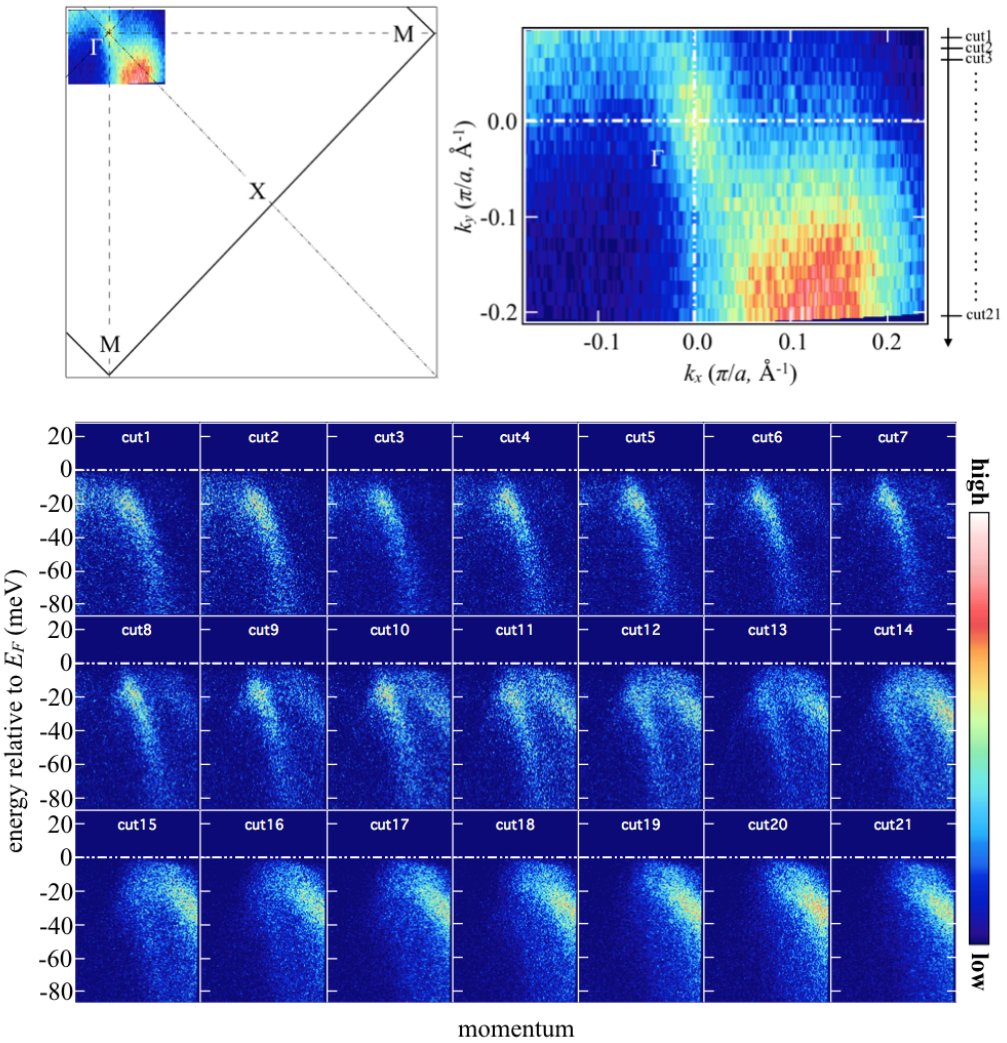

Figure 6.6: Top: Fermi surface mapping of $FeSe_{0.4}Te_{0.6}$ integrated within $E_F \pm 5$ meV using a mixture of s- and p-polarizations. The measured region with respect to the Brillouin zone is shown in the left, and expanded view is shown in the right. The incident photon energy is set to be 6.4 eV. Bottom: each cut of the Fermi surface.

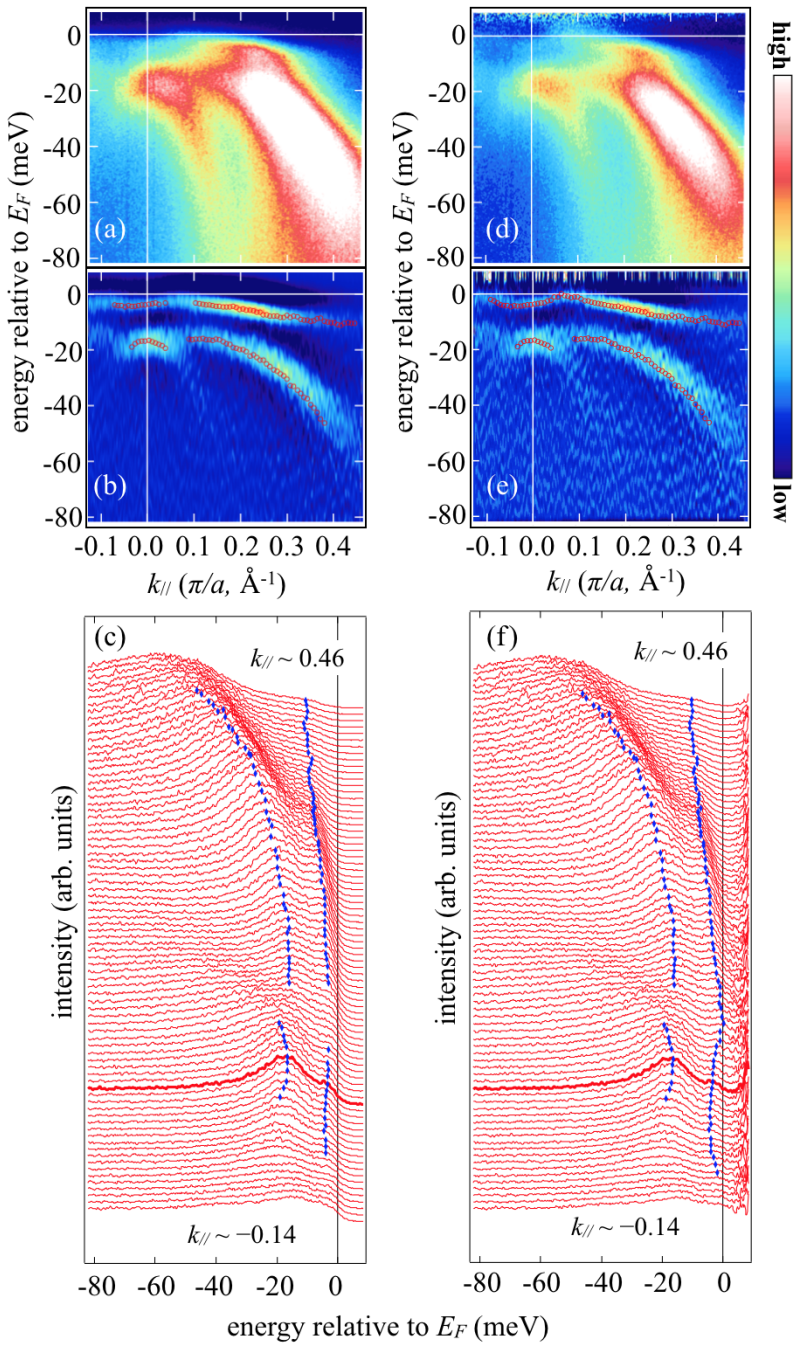

Figure 6.7: (a) ARPES spectra ($A(k,\omega)$) along Γ-M direction , (b) $-(\partial^2 A(k,\omega)/\partial\omega^2)$, and (c) EDCs. Peak positions of the EDCs are overlaid on the second derivative data and EDCs, and they are respectively denoted by circles and vertical bars. (d), (e), and (f) are the same as (a), (b), and (c) but the ARPES spectra were divided by Fermi-Dirac function convolved with experimental resolution.

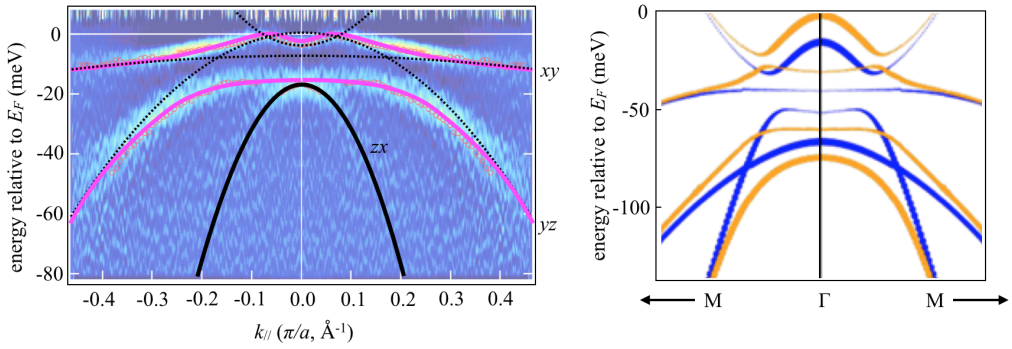

Figure 6.8: *Left*: interpretation of the band dispersions obtained by laser-ARPES. *Right*: GGA calculation performed by Johnson *et al.* [79] with (orange line) and without (blue line) spin-orbit interaction, symmetrized at Γ point. The replacement of Te by Se in each layer introduces a symmetry breaking that already splits the degeneracy at Γ without spin-orbit coupling.

Figure 6.7(a) shows the ARPES spectra ($A(k,\omega)$) cut along Γ-M as a function of $k_{||}$ whereas Fig. 6.7(b) shows its second derivative in the energy direction ($\partial^2 A(k,\omega)/\partial\omega^2$). Figure 6.7(c) shows the energy distribution curves (EDCs). The peak positions of EDCs are overlaid on both second derivative image [Fig. 6.7(b)] and EDCs [Fig. 6.7(c)], and they are respectively denoted by circles and vertical bars. In order to see the features slightly above the Fermi level, one can divide the ARPES spectra by Fermi-Dirac function convolved with experimental resolution. Figures 6.7(d), 6.7(e), and 6.7(f) are the same as Figs. 6.7(a), 6.7(b), and 6.7(c), but on the ARPES spectra divided by Fermi-Dirac function convolved with experimental resolution. From the raw data as well as its second derivative, one can clearly see that α and β bands are almost degenerate at the zone center. In addition to the α and β bands, another dispersion, most likely to be γ band, has been resolved between E ∼5 - 10 meV. This weak feature can be more clearly see in Figs. 6.7(d) - 6.7(f) than Figs. 6.7(a) - 6.7(c), and suddenly shows strong intensity when it comes close to the β band.

This can be due to the hybridization of β and γ bands (*i.e.*, the hybridization of yz and xy orbitals) or the spin-orbit splitting of yz and xy orbitals. The γ band has less (more) xy character when it is close to (away from) the zone center due to the the hybridization with β band.

Left panel of Fig. 6.8 shows our interpretation, the orbital characterization of the observed bands. The solid lines are the guide of the ARPES results, and the second derivative image is semi-transparently overlaid on the sketch. Right panel of Fig. 6.8 is the DFT calculation on AFM $FeTe_{0.5}Se_{0.5}$ performed by Johnson *et al.* [79] with and without spin-orbit interaction, and they are denoted by blue orange

Table 6.2: Summary of the energy shifts and renormalization factors for fitting the experimental band dispersions.

	energy shift (meV)	renormalization factor
30th band (α band)	-155	$1/10$
31st band (β band)	-250	$1/6$
32nd band (γ band)	-160	$1/17$

lines, respectively. Comparing the ARPES results with this DFT calculation, the band structure is very similar with the one calculated with spin-orbit interaction, except the band position, band width, and yz/zx orbital degeneracy at Γ point. The energy shift can be interpreted as the effect of self-energy derived from the electron correlation, and the shrinkage of band width can be understood as a renormalization effect. However, the yz/zx orbital degeneracy observed by ARPES is not consistent with the picture under the finite spin-orbit interaction since in general the spin-orbit interaction resolves the orbital degeneracy.

In order to confirm that the spin-orbit interaction resolves the orbital degeneracy at Γ point and to confirm whether the xy/yz splitting between Γ and M points is due to spin-orbit interaction (SOC) or not, we have performed DFT calculation within GGA scheme on non-magnetic FeTe. Figures 6.9(a) and 6.9(b) are the band structures calculated without and with SOC, respectively. One can clearly see from Fig. 6.9(c) that not only the yz/zx orbital degeneracy at Γ is resolved point, but also the xy/yz orbital degeneracy between Γ and M points is also resolved by the SOC. The expanded views are shown in Figs. 6.9(d) and 6.9(e). Besides, the three hole bands are crossing E_F when the SOC is not included, and one of the hole bands (α band) shifts below E_F when the SOC is taken into account.

Reminding us of the experimental fact, the ARPES results in Fig. 6.7 are; the orbital degeneracy of yz/zx at Γ is kept while the that of xy/yz is resolved. In order to compare the ARPES spectra and DFT calculation, the DFT results are overlaid on the ARPES spectra as shown in Fig. 6.9(f). The band dispersions obtained by GGA calculation were required to shift energies and to rescale the band widths in order to fit with the ARPES results. The magnitude of energy shifts and renormalization factors are summarized in Tab. 6.2. The α and β bands have good agreement with DFT calculation when energy shifts and renormalization factors were adjusted while the γ band has poor agreement especially near Γ point, where it hybridized with an electron-like band coming from above the γ band; the experimental dispersion of γ band locates in the direction of lower binding energy. This indicates that there might be a stronger scattering between γ band ($d\ xy$ orbital) and α and/or β bands near Γ point. In other words, since this part is hybridized with the electron-like band, it is possible that there exist a different type of scattering compared with hole-like part. Moreover, it could explain the yz/zx orbital degeneracy observed

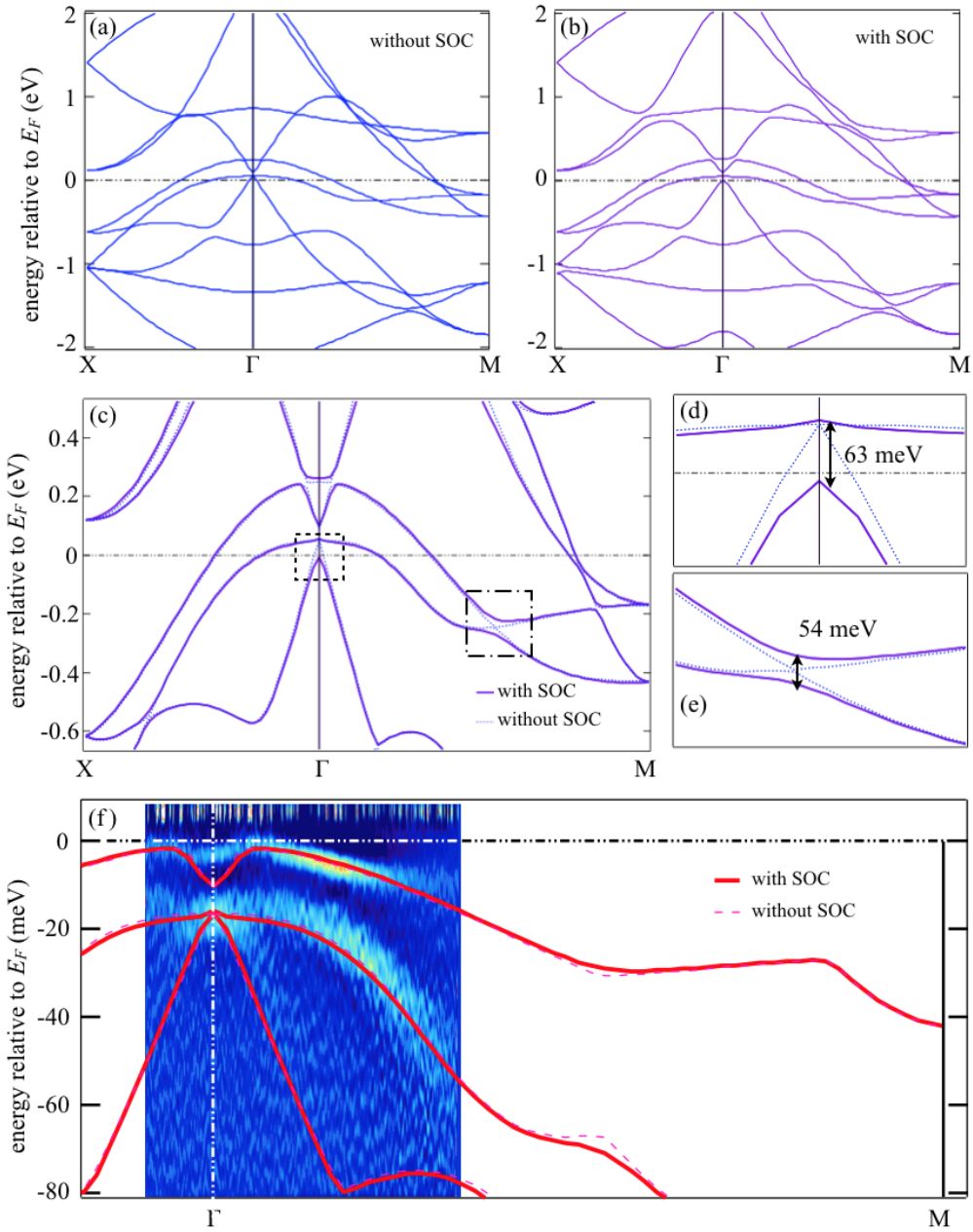

Figure 6.9: Band structures calculated using GGA on FeTe (a) without spin-orbit coupling (SOC) and (b) with SOC. (c) Comparison of (a) and (b) near E_F. (d) and (e) are the expanded view of the dashed region and dot-dashed region in (c), respectively. (f) Comparison of second derivative ARPES spectra of $FeSe_{0.4}Te_{0.6}$ divided by Fermi-Dirac function convolved with experimental resolution with GGA calculation on FeTe with and without SOC. The GGA results are shifted in the energy direction and band widths are scaled as summarized in Tab. 6.2.

by ARPES as follows. When the SOC is taken into account, orbital degeneracies of both yz/zx at Γ and xy/yz in the middle of Γ-M are resolved. However, when this scattering appeared near Γ is also taken into account, the lifted yz orbital (β band) goes back to the direction of higher binding energy. If the energy scale of the splitting due to the SOC and that of the scattering is the same, yz/zx orbital degeneracy can be kept under the SOC effective environment.

It is also worth pointing out the orbital-dependent band renormalization. The xy orbital has a strong renormalization compared with yz/zx, and yz/zx orbitals have different renormalization factors even in a tetragonal symmetry. Different strengths of renormalization indicate that there may already exist a nematic tendency, namely, the yz/zx orbital instability. Strongly renormalized xy orbital and yz/zx orbital instability may play important role for the superconductivity.

6.2.4 Conclusion

In summary, we have performed laser-ARPES on $FeSe_{0.4}Te_{0.6}$ and DFT calculation on FeTe. We have successfully observed the Fe $3d$ yz/zx orbital degeneracy at Γ point and xy/yz splitting as well. It is identified by DFT calculation that the xy/yz splitting was due to spin-orbit interaction. The comparison of ARPES and DFT suggests that a strong and/or different type of scattering may exist between xy (γ band) and yz (β band) orbitals near Γ point since near the Γ point the γ band is hybridized with an electron-like band coming from above. This scattering might cause the degeneracy of yz/zx under the SOC-effective situation. Moreover, the orbital-dependent band renormalization was confirmed. The xy orbital has a strong renormalization compared with yz/zx, and yz/zx orbitals have different renormalization factors even in a tetragonal symmetry. Different renormalizations in yz/zx orbitals indicate that there may already exist a nematic tendency, namely, the yz/zx orbital instability. Strongly renormalized xy orbital and yz/zx orbital instability may play important role for the superconductivity.

6.3 Unrestricted Hartree-Fock study on FeTe

6.3.1 Method of calculation

We use the multi-orbital d-p type Hamiltonian where full degeneracy of the Fe $3d$ orbitals and the chalcogen (Ch) p orbitals are taken into account.

The transfer integrals between the Ch p orbitals $V^{pp}_{kll'}$ are given by SlaterKoster parameters $(pp\sigma)$ and $(pp\pi)$ which are fixed at 0.60 eV and -0.15 eV respectively. The transfer integrals between the Fe $3d$ and Ch p orbitals V^{pd}_{kml} are represented by $(pd\sigma)$ and $(pd\pi)$. They are fixed as $(pd\sigma) = -2.0$ eV and $(pd\pi) = 0.9$ eV.

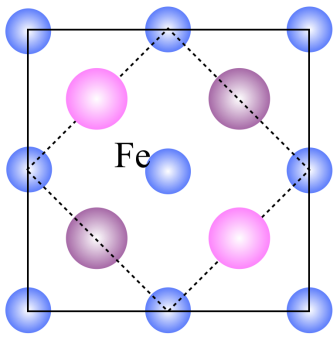

Figure 6.10: Top view of the schematic crystal structure of Fe(Se,Te) system for the unrestricted Hartree-Fock calculation.

The intra-atomic Coulomb interactions between Fe $3d$ electrons are given by Kanamori parameters. They can be expressed as $u = u' + j + j'$ and $j = j'$. The charge-transfer energy Δ is defined by $\Delta = \varepsilon_d - \varepsilon_p + 6U$, where ε_d and ε_p are the energies of the bare Fe $3d$ and Ch p orbitals, and $U[= u - (20/9)j]$ is the multiplet-averaged d-d Coulomb interaction. The summary of the electronic-structure parameters are displayed in Tab. 6.3.

We set the unitcell of Fe(Se,Te) with periodic boundary conditions and put the Fe $3d$ and Ch p electrons on its each site.

6.3.2 Results and discussion

First of all, we have calculated with the various spin configuration, and compared the energies in order to find out the energetically stable spin configuration; paramagnetic (PM), ferromagnetic (FM), stripe antiferromagnetic (AFM), diagonal antiferromagnetic (dAFM), bistripe antiferromagnetic (2AFM), and diagonal-bistripe antiferromagnetic (d2AFM) states. The PM state has the highest energy, indicating that the spin-ordering can give rise to more stable states. The results are summa-

Table 6.3: Summary of the electronic-structure parameters for unrestricted Hartree-Fock calculation of FeCh system where Ch stands for chalcogen atoms.

charge-transfer energy	$\Delta = \varepsilon_d - \varepsilon_p + 6U$	
Kanamori parameters	$u = u' + j + j' = 2.5$ eV	$j = j' = 0.5$ eV
d-d Coulomb interaction	$U = u - (20/9)j$	
Fe-Ch	$(pd\sigma) = -2.0$ eV	$(pd\pi) = 0.9$ eV
Ch-Ch	$(pp\sigma) = 0.6$ eV	$(pp\pi) = -0.15$ eV
Fe-Fe	$(dd\sigma) = 0.8$ eV	$(dd\pi) = -0.4$ eV

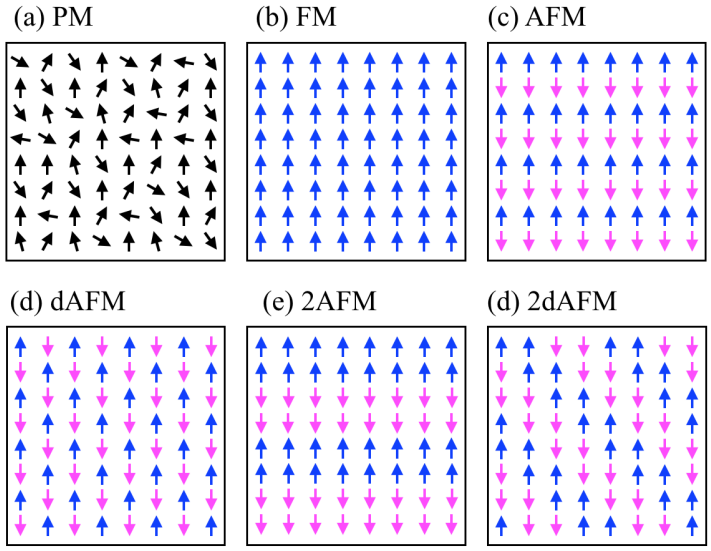

Figure 6.11: Various spin confiugurations of Fe(Se,Te) system. (a) paramagnetic, (b) ferromagnetic, (c) antiferromagnetic, (d) diagonal antiferromagnetic, (e) bistripe antiferromagnetic, and (f) diagonal & bistripe antiferromagnetic order.

Table 6.4: Summary of the relative energies on the various spin configuration presented in Fig. 6.11. The energy reference is the energy of AFM states. The number of nearest FM/AFM spins and second nearest FM/AFM spins are also shown.

	PM	FM	AFM	dAFM	2AFM	d2AFM
ΔE per Fe site (eV)	25.95	-0.0036	0	20.50	20.50	10.51
nearest FM spin	none	4	2	0	3	2
nearest AFM spin	none	0	2	4	1	2
2nd nearest FM spin	none	4	0	4	2	2
2nd nearest AFM spin	none	0	4	0	2	2

rized in Tab. 6.4. From Tab. 6.4, one can see that the system prefers for nearest spins to be FM whereas for second nearest to be AFM states. Since it is geometrically impossible to take the 4 FM nearest spins and 4 AFM spins at the same time, the energetically stable states were found to be FM and AFM states. Therefore, since the real system shows AFM state, our tight binding model gave us reasonable results.

We have investigated the u (Kanamori paramter) dependence of the system under the PM and AFM condition.The gap size and magnitude of magnetic moment are shown in the upper panel of Fig. 6.12. The number of occupied electrons in the yz/zx orbitals are also shown in the lower panel of Fig. 6.12. When the system is in PM state, the yz/zx orbital degeneracy is kept as shown in Fig. 6.12. When the

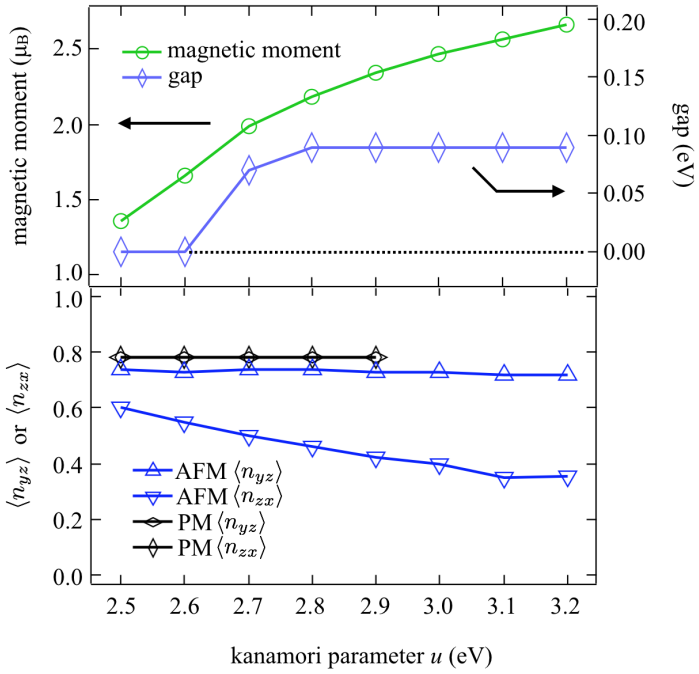

Figure 6.12: Magnetic moment on each Fe site, the magnitude of band gap, and the expectation value of occupied electrons in the yz/zx orbitals [$\langle n_{yz}\rangle/\langle n_{zx}\rangle$] under the PM and AFM condition as a function of Kanamori parameter u calculated using multi-orbital d-p model within the scheme of unrestricted Hartree-Fock approximation.

AFM condition is applied, one can see that the system is already in the orbital ordered states in this energy range of the kanamori parameter. We found that there is an AFM and ferro-orbital metallic state, and system becomes AFM and ferro-orbital insulating state with increasing u. In the insulating phase, when the u increases, the AFM and ferro-orbital ordered states further develop, indicating that the system is in the Kugel-Khomskii regime [21]. As for the AFM metallic state, it could be due to the mean-field treatment since we have neglected the effects of fluctuation (while the AFM insulating phase can be well-described by the HF method).

6.3.3 Conclusion

We have investigated the spin and orbital configurations on Fe(Se,Te) system. The results of the spin configuration are consistent with the neutron scattering experimental results, indicating that this tight binding model is reasonable to a certain extent. Using this model, we have studied u dependence of the system, and found that there is a metal-insulator transition point. However, this transition may be due

to the mean-field approximation since we neglected the effects of fluctuation, which is generally not negligible in the metallic phase.

7

ELECTRONIC STRUCTURE OF RE(O,F)BIS$_2$

In this chapter, electronic structures of BiS$_2$-based Ce(O,F)BiS$_2$ superconductor and EuFBiS$_2$ have been investigated. In the introducing part of this chapter, we will take a look at previous studies and problems of the BiS$_2$-based systems. In the results part, it mainly consists of block layer part and BiS$_2$ part. In the former one, we see the electronic states of block layer using XAS technique and resonant PES whereas in the latter one we discuss the orbital states of Bi $6p$ using polarization-dependent ARPES.

7.1 Characteristic features and problems

The discovery of superconductivity in $Bi_4O_4S_3$ and La(O,F)BiS_2 by Mizuguchi *et al.* [19, 20] in 2012 has given rise to an extensive research efforts from both theoretical and experimental aspects. It was found that superconductivity of $Bi_4O_4S_3$ originates from the BiS_2 layers. The crystal structure is composed of a stacking of BiS_2 superconducting layers and the spacer layers. Therefore, this family has been named as 'BiS_2-based superconductors'.

7.1.1 Band structure and quasi-one-dimensionality

Soon after the discovery of BiS_2-based superconductivity, Usui, Suziki, and Kuroki theoretically proposed that conduction electrons are mainly dominated by Bi $6p_x/6p_y$ and S $3p$ by means of deducing a minimal model for $LaOBiS_2$ [84]. They first performed *ab initio* band-structure calculation as in Fig. 7.1(a) and obtained the maximally localized Wannier orbitals. Using these orbitals, they constructed an effective tight-binding model with 24 orbitals; six Bi $6p$, 12 S $3p$, and six O $2p$ orbitals, and the results are shown in Fig. 7.1(b). Omitting the orbitals which are far from E_F and neglecting the interlayer coupling between BiS layers, the minimal model ends up with four-orbital model consisting of Bi $6p$ and S $3p$. The model Hamiltonian was selected as

$$\begin{aligned}\mathscr{H}_0 = &\sum_{ij}\sum_{\mu\nu}\sum_{\sigma}[t(x_i - x_j, y_i - y_j; \mu, \nu)c^{\dagger}_{i\mu\sigma}c_{j\nu\sigma} \\ &+ t(x_j - x_i, y_j - y_i; \nu, \mu)c^{\dagger}_{j\nu\sigma}c_{i\mu\sigma}] + \sum_{i\mu\sigma}\varepsilon_{\mu}n_{i\mu\sigma}. \end{aligned} \tag{7.1}$$

Moreover, an even more simple model can be found by focusing only on the bands that intersect the Fermi level. Extracting these bands using the maximally localized Wannier orbitals centered at the Bi sites and neglecting the interlayer hopping, the Hamiltonian reduces to a two-dimensional two-orbital model.

Moreover, one dimensional character of Bi p_x/p_y was found, *i.e.*, the p_X ($\propto p_x + p_y$) orbital character is dominated in the (0,0)-(π, π) direction as in Fig. 7.2(a). The one-dimensional bands generally provide good nesting of the Fermi surfaces. In order to see this effect, they calculated for the two orbital model the 4×4 irreducible susceptibility matrix in the orbital representation $\chi^0_{l_1l_2l_3l_4}(\boldsymbol{q}) = \sum_k G^0_{l_1l_3}G^0_{l_4l_2}$, where G^0 represents the 2×2 bare Green's function matrix, and they found diagonal structures ((0,0) - (π, π) direction) and unequivalence of three nestings due to the nearest neighbor hopping in Eq. (7.1).

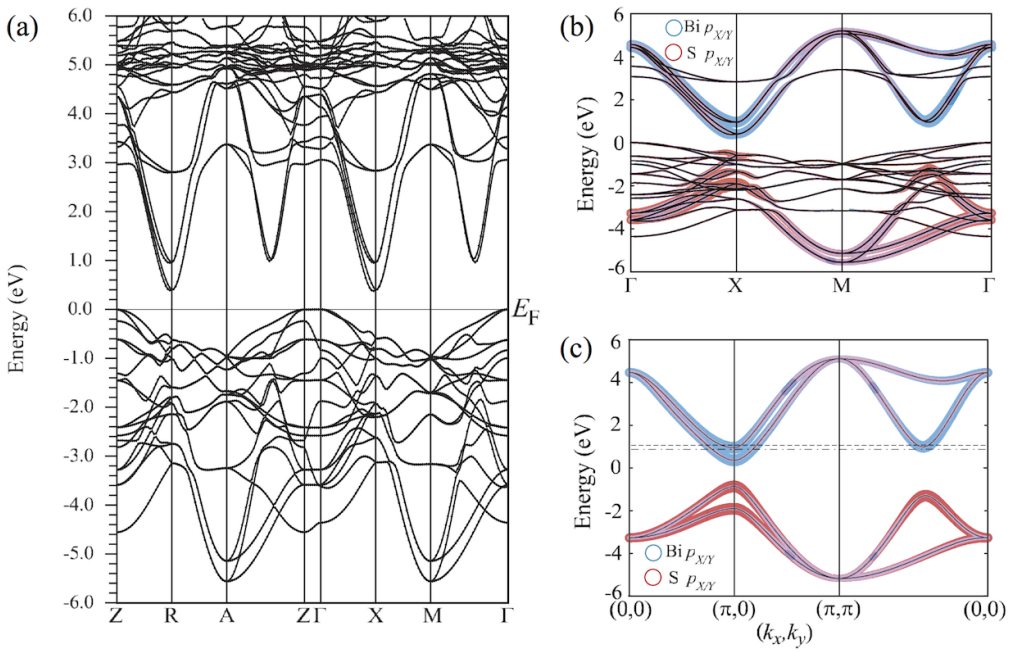

Figure 7.1: (a) *Ab initio* band-structure calculation on $LaOBiS_2$. Band structures calculated by (b) the 24-orbital model and (c) the four-orbital model [84].

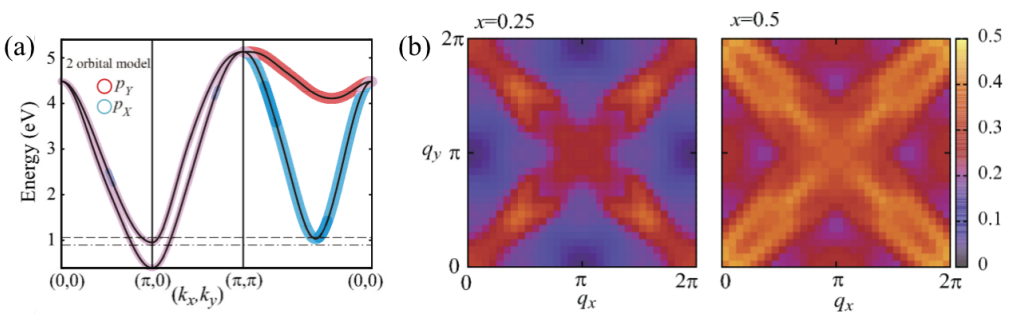

Figure 7.2: (a) Band structure calculated by the two-orbital model. (b) The largest eigenvalues of the irreducible susceptibility matrix at $x = 0.25$ and $x = 0.5$ [84].

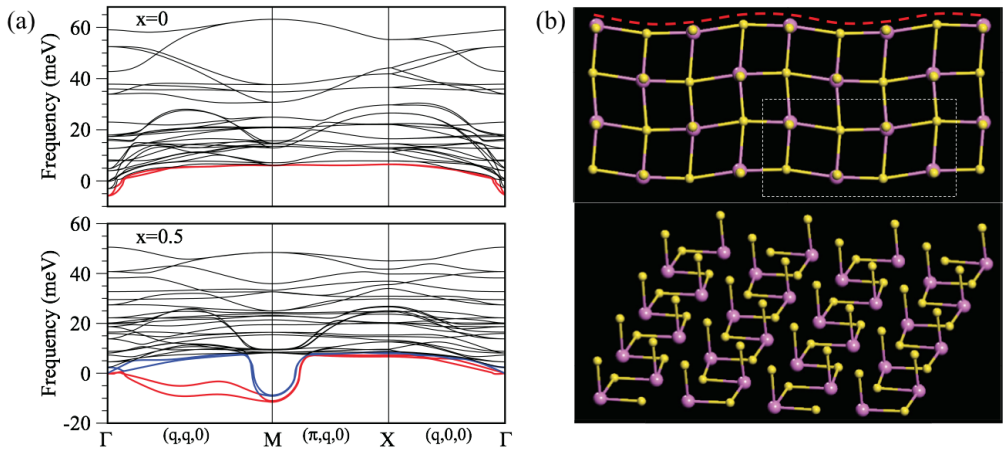

Figure 7.3: (a) Phonon dispersions of $LaOBiS_2$ and $LaO_{0.5}F_{0.5}BiS_2$, indicating the instabilities at Γ for $x = 0$ and along the entire line $(q, q, 0)$ with the most unstable phonons at M and $(\pi/2, \pi/2)$ for $x = 0.5$. (b) The BiS_2 layer in a fully optimized CDW phase of $LaO_{0.5}F_{0.5}BiS_2$. Large and small spheres are Bi and S, respectively [85].

7.1.2 Phonon, spin fluctuation, and/or orbital fluctuation

It was reported that BiS_2-based systems are strong electron-phonon coupling superconductors by first-principles calculations [85], which is shown in Fig. 7.3(a). The $x = 0.0$ system shows the instability near Γ point while the $x = 0.5$ system has instabilities along the entire line of $Q = (q, q, 0)$. They repeated the phonon dispersion calculations for $x = 0.5$ using a charged system without F doping and obtained the same instabilities, indicating that the soft phonons found here are an intrinsic property of the BiS_2 plane. Moreover, it also reported that they found the inharmonic ferroelectric soft phonons and one-dimensional CDW instability, and corresponding crystal structure is shown in Fig. 7.3(b)

Meanwhile, Usui *et al.* also investigated the superconducting pairing mechanism using spin fluctuation [84], and Martins *et al.* also adopt the two-orbital model and spin fluctuation as Usui *et al.*, and identified that B_{2g} and A_{1g} gap functions are closely competing as the dominant pairing channels, particularly for band fillings around $n = 0.5$ [86].

Since the nesting vectors can be taken by the same orbitals, orbital fluctuation has not been discussed yet in any paper at this moment. Therefore it is required to identify the orbital states near the Fermi level.

Table 7.1: Summary of the previous EPMA studies on $RE\mathrm{O}_{1-x}\mathrm{F}_x\mathrm{BiS}_2$ (RE=Ce,La, Nd) systems; comparison of nominal x and the amount of F estimated by EPMA.

RE	nominal x	estimation by EPMA	c-axis (Å)	reference
Ce	0.3	0.16	13.507	Miura *et al.* [87]
	0.5	0.24	13.383	
	0.7	0.28	13.340	
La	0.3	0.23	13.57	Nagao *et al.* [88]
	0.7	0.46	13.37	
Nd	0.3	0.26	13.56	
	0.7	0.37	13.43	

Table 7.2: Summary of the previous ARPES studies on $\mathrm{NdO}_{1-x}\mathrm{F}_x\mathrm{BiS}_2$ systems; comparison of nominal x and the electron concentration estimated by Luttinger volume (LV) of the Fermi surface.

RE	nominal x	estimation by LV	c-axis (Å)	reference
Nd	0.3	0.07	13.49	Zeng *et al.* [89]
	0.5	0.16	–	Ye *et al.* [90]

7.1.3 F-doping; nominal vs. effective

In the $RE\mathrm{O}_{1-x}\mathrm{F}_x\mathrm{BiS}_2$ systems, it is believed that the F-doping corresponds to the electron doping to the BiS_2 layer, controlling the band filling.

Previous electron probe micro analysis (EPMA) studies have revealed that the actual amout of F estimated by EPMA is always smaller than the nominal value while ARPES studies using Luttinger theorem have observed much smaller effective carrier concentration than the nominal x. Those differences are so large that one cannot ignore them, and this is one of the central problems standing in the $RE\mathrm{O}_{1-x}\mathrm{F}_x\mathrm{BiS}_2$ systems. They are summarized in Tab. 7.1 and Tab. 7.2, respectively. One can see from these tables that the F amount is always much smaller than the nominal values of x, and the Luttinger volume is even smaller than the value estimated by EPMA.

7.1.4 Physical properties of Ce(O,F)BiS_2 and EuFBiS_2

In this thesis, we focus on Ce(O,F)BiS_2 and EuFBiS_2 systems because they are particularly interesting among the $RE\mathrm{O}_{1-x}\mathrm{F}_x\mathrm{BiS}_2$ systems; the Ce(O,F)BiS_2 system shows the coexistence of superconductivity and ferromagnetism at low temperature [91] while the EuFBiS_2 system shows the Eu mixed valence state and it is considered that a part of electrons in Eu is self-doped to the BiS_2 layer [92]. More-

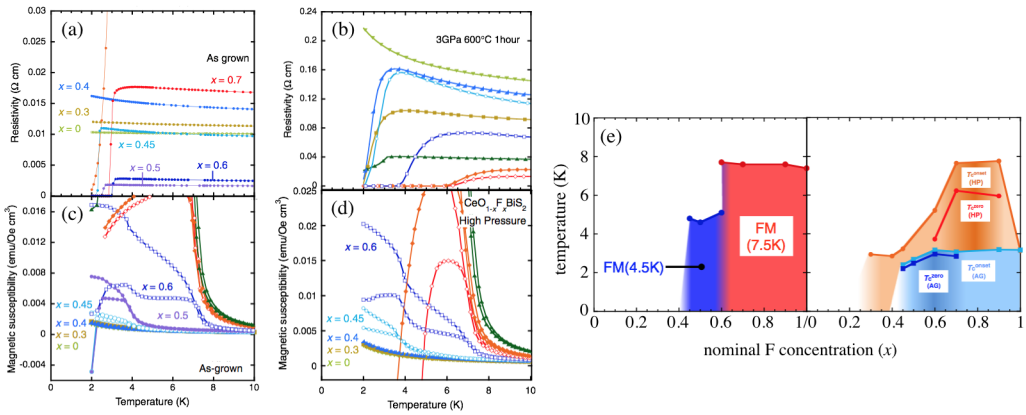

Figure 7.4: (a) Resistivity of $CeO_{1-x}F_xBiS_2$ system with various x grown under ambient pressure and (b) under high pressure. (c) Magnetic susceptibility of $CeO_{1-x}F_xBiS_2$ system grown under ambient pressure and (d) under high pressure. (e) Magnetic and superconducting phase diagram [91].

over, it is also possible to approach the problems argued in the earlier part of this section.

$CeO_{1-x}F_xBiS_2$

As indicated above, this system shows the coexistence of superconductivity and ferromagnetism at low temperature. The resistivities and magnetic susceptibilities of $CeO_{1-x}F_xBiS_2$ samples grown under ambient pressure and under high pressure are shown in Fig. 7.4.

$EuFBiS_2$

The previous Mössbauer study on the $EuFBiS_2$ system revealed that the system shows Eu mixed valence state as shown in Fig. 7.5(a). Band-structure calculations using LSDA+U also performed with various U, and they are shown in the rest of Fig. 7.5. The calculation indicates that a part of electrons in Eu were introduced to the BiS_2 layer; not only Bi $6p_x/6p_y$ bands are crossing E_F, but also Eu $4f$ bands are crossing E_F around X and M points, *i.e.*, the system in the valence fluctuation state.

7.1.5 Motivation and overview

We first approached the each specific system ($CeO_{1-x}F_xBiS_2$ and $EuFBiS_2$), try to understand the meaning of the experimental results, and applied some calculation in order to confirm whether the interpretation is possible or not. Then we also revealed

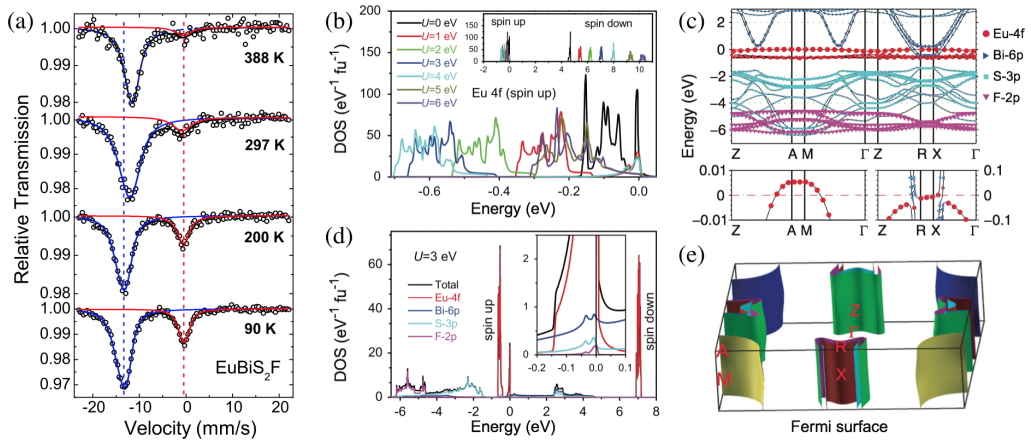

Figure 7.5: (a) ^{151}Eu Mössbauer spectra of $EuFBiS_2$. Band-structure calculations for $EuFBiS_2$ using LSDA+U; (b) Eu $4f$ bands with various U values., (c) band structure with $U = 3$ eV with the notations of dominated orbitals (lower panels zoom in the band dispersions near E_F), (c) total and projected DOS with $U = 3$ eV (inset: enlarged plot near E_F, and (d) Fermi surfaces [92].

the possible answers to the problems mentioned in this section above, the quasi-one-dimensionality, phonon, spin-, and/or orbital-fluctuation, and nominal v. effective carrier problems. The overview of this chapter is as follows:

In $CeO_{1-x}F_xBiS_2$ system, the coexistence of superconductivity and ferromagnetism provokes further studies to understand the interaction of different electronic degrees of freedom and the role of spacer layers. In order to reveal the role of the F-doping not only in a sense of carrier-doping but also in a broad sense including the relation between superconductivity and ferromagnetism, we have performed Ce L_3-edge XAS on polycrystalline $CeO_{1-x}F_xBiS_2$ system with various x for both as-grown and high pressure synthesized samples in Section 7.2. Moreover, since we have found the Ce valence state is interesting and there were some inconsistency compared with magnetic susceptibility measurements on single crystals [93], we again performed Ce L_3-edge XAS but on single crystals. In order to obtain the partial DOS of Ce $4f$ orbital, we also performed Ce $4d$-$4f$ resonant ARPES on the same single crystals in Section 7.3.

As for the $EuFBiS_2$ system, similar phenomena was observed as $CeO_{1-x}F_xBiS_2$. In order to solve this issue, we have performed Eu L_3-edge XAS, Eu $4d$-$4f$ resonant PES, and ARPES.

In Section 7.5, we finally discuss the quasi-one-dimensionality proposed by Usui, Suzuki, Kuroki, that can be directly confirmed by polarization-dependent ARPES. According to the band structure calculation on doped system, Fermi surfaces consist of Bi $6p_x/6p_y$ orbitals, and Bi $6p_z$ orbital locates above E_F. Therefore,

one can select the horizontally or vertically polarized photons as an incident light, and it allows us to select the Bi $6p_x$ or Bi $6p_y$ orbitals, respectively. Thus we have performed the polarization-dependent ARPES on $CeO_{0.5}F_{0.5}BiS_2$ system and elucidated the orbital characters on the Fermi surfaces. After the orbital-characterization of the Fermi surfaces, we also discuss the possibilities of the pairing mechanism by the nesting condition.

We summarize the important features and remarkable findings on BiS_2 systems in Section 7.6.

7.2 Impact of F-doping in Ce(O,F)BiS$_2$ revealed by Ce L_3-edge XAS

We have performed Ce L_3-edge XAS measurements on $CeO_{1-x}F_xBiS_2$, in which the superconductivity of the BiS_2 layer and the ferromagnetism of the $CeO_{1-x}F_x$ layer are induced by the F-doping, in order to investigate the impact of the F-doping on the local electronic and lattice structures. The Ce L_3-edge XAS spectrum of $CeOBiS_2$ exhibits coexistence of $4f^1$ (Ce^{3+}) and $4f^0$ (Ce^{4+}) state transitions revealing Ce mixed valency in this system. The spectral weight of the $4f^0$ state decreases with the F-doping and completely disappears for $x > 0.4$ where the system shows the superconductivity and the ferromagnetism. The results suggest that suppression of Ce-S-Bi coupling channel by the F-doping appears to drive the system from the valence fluctuation regime to the Kondo-like regime, leading to the coexistence of the superconducting BiS_2 layer and the ferromagnetic $CeO_{1-x}F_x$ layer.

Ce L_3 XAS is a direct probe of the local structure around a selected absorbing atom and distribution of the valence electrons, with the final states in the continuum being due to multiple scattering resonances of the photoelectron in a finite cluster [94]. In this work, we have exploited Ce L_3 XAS to investigate the impact of the F-doping on the local electronic and lattice structures of $CeO_{1-x}F_xBiS_2$ system synthesized differently, i.e. as grown (AG) and high pressure (HP) annealed.

7.2.1 Experimental condition

Ce L_3-edge XAS measurements were performed on polycrystalline samples of $CeO_{1-x}F_xBiS_2$ prepared by the solid-state reaction method. Both AG and HP annealed samples were used for the measurements. All the samples were well characterized for their transport and average structural properties prior to the absorption measurements. Details on the sample preparation and characterization are given elsewhere [91]. The x-ray absorption experiments were performed at the XAFS beamline of the Elettra Synchrotron Radiation Facility, Trieste. Since it is difficult to prepare clean surfaces using the available polycrystalline $CeO_{1-x}F_xBiS_2$ sam-

ples, the bulk-sensitive Ce L_3-edge XAS taken in the transmission mode is the most reliable tool to evaluate the Ce valence. Therefore, the measurements were taken at room temperature in transmission mode using three ionization chambers mounted in series for simultaneous measurements on the sample and a reference. As a routine experimental approach, several absorption scans were collected on each sample to ensure the reproducibility of the spectra, in addition to the high signal to noise ratio.

7.2.2 Results and discussion

Figure 7.6 displays the Ce L_3-edge XAS spectra of AG (Fig. 7.6 (a)) and HP (Fig. 7.6 (d)) $CeO_{1-x}F_xBiS_2$ ($x = 0.0$, 0.2, 0.4, 0.6, 0.8, and 1.0). The spectra are normalized with respect to the atomic absorption estimated by a linear fit to the high energy part of the spectra. Three main structures around 5725 eV, 5737 eV, and 5758 eV can be identified on the Ce L_3-edge XAS spectra; two of them reflect the electronic structure while the one does local crystal structure. The first peak around 5725 eV is the absorption white line corresponding to the transition from the Ce $2p$ core level to the vacant Ce $5d$ state mixed with the Ce $4f^1$ final state. [95–98]. On the other hand, the second peak around 5737 eV corresponds to the transition from the Ce $2p$ core level to the vacant Ce $5d$ state mixed with the Ce $4f^0$ final state. The $4f^1$ and $4f^0$ final states are the so-called well-screened and poorly-screened states and provide information on the Ce valence states. Presence of both $4f^1$ and $4f^0$ states suggest the Ce^{3+}/Ce^{4+} valence fluctuation. The energy difference between the $4f^1$ and $4f^0$ absorption peaks, which is approximately 12 eV [95–97] is mainly determined by the Ce $2p$ - Ce $4f$ Coulomb interaction and is expected to be independent of the F-doping. One can see a systematic change due to the F-doping in the $4f^1$ and $4f^0$ peak intensity as shown Figs. 7.6(b) and 7.6(e). They are so-called difference spectra, that was obtained by subtracting the reference spectra, in this case we chose $x = 1.0$, from each spectrum. The third peak around 5758 eV includes the information on the local lattice structures. This peak is so-called continuum resonance (CR), likely to be due to Ce-Bi scattering with a contribution from the Ce-Ce scattering, reflecting evolution of the Ce-Bi/Ce bond length. In addition, there is a weak feature around 5742 eV. This feature is a characteristic feature of layered rare-earth systems, and its intensity is generally sensitive to the O/F atom order/disorder in the CeO/F layer. Figures 7.6(c) and 7.6(f) are the first derivative of the Ce L_3-edge XAS spectra with respect to the photon energy, and one can see that the energy position of $4f^1$ and $4f^0$ are the same for various x while the peak position of the CR has a x-dependence.

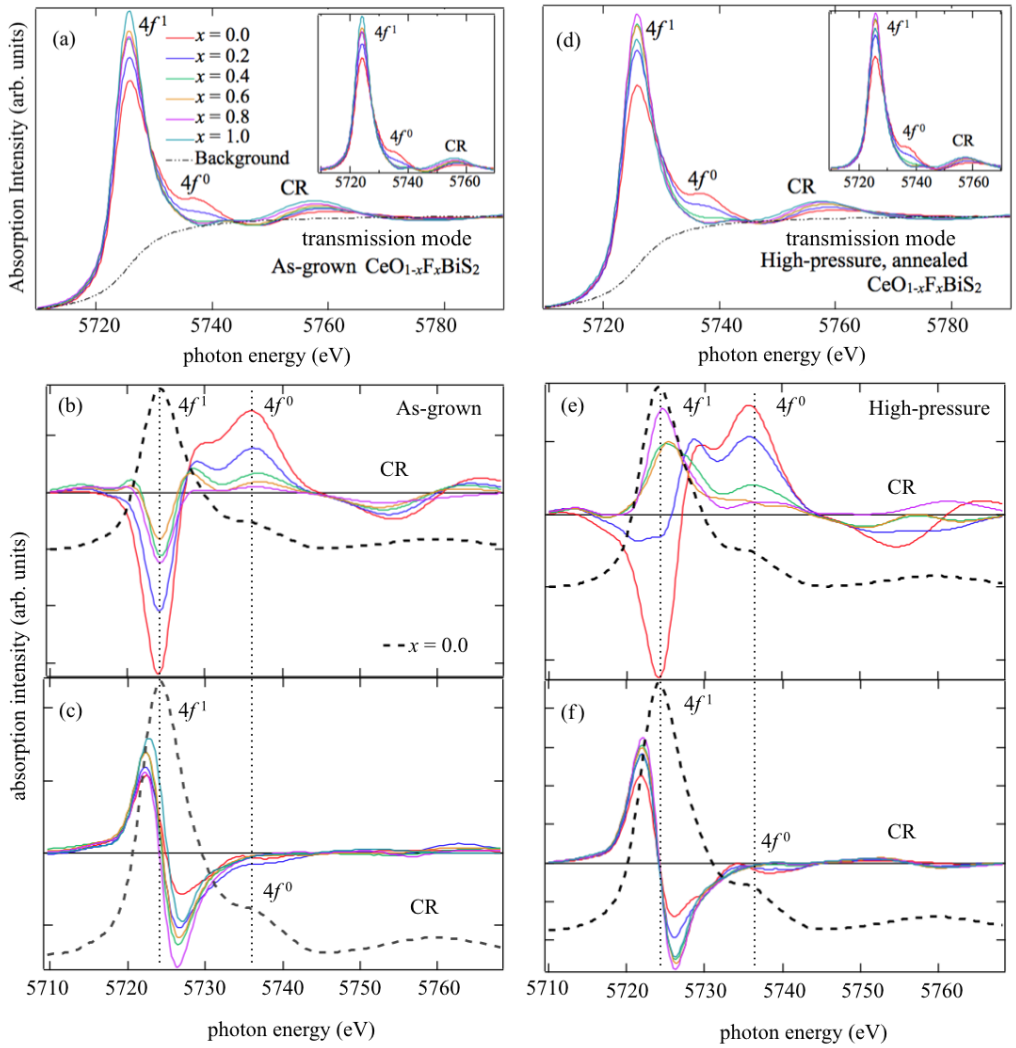

Figure 7.6: (a) Ce L_3-edge normalized XAS spectra of AG $CeO_{1-x}F_xBiS_2$ system with $x = 0.0$, 0.2, 0.4, 0.6, 0.8, and 1.0. The $4f^1$, $4f^0$, and CR peaks around 5725 eV, 5737 eV, and 5758 eV are shown. The background (arctangent function)-subtracted spectra are shown in the insets. The spectra were taken at room temperature with transmission mode. (b) The difference spectra with respect to AG $x = 1.0$ sample. (c) First derivative with respect to energy. The reference spectrum (normalized XAS spectrum of $x = 0.0$ system) is shown for both (b) and (c). (d), (e), and (f) are the same for (a), (b), and (c) but on HP $CeO_{1-x}F_xBiS_2$ system.

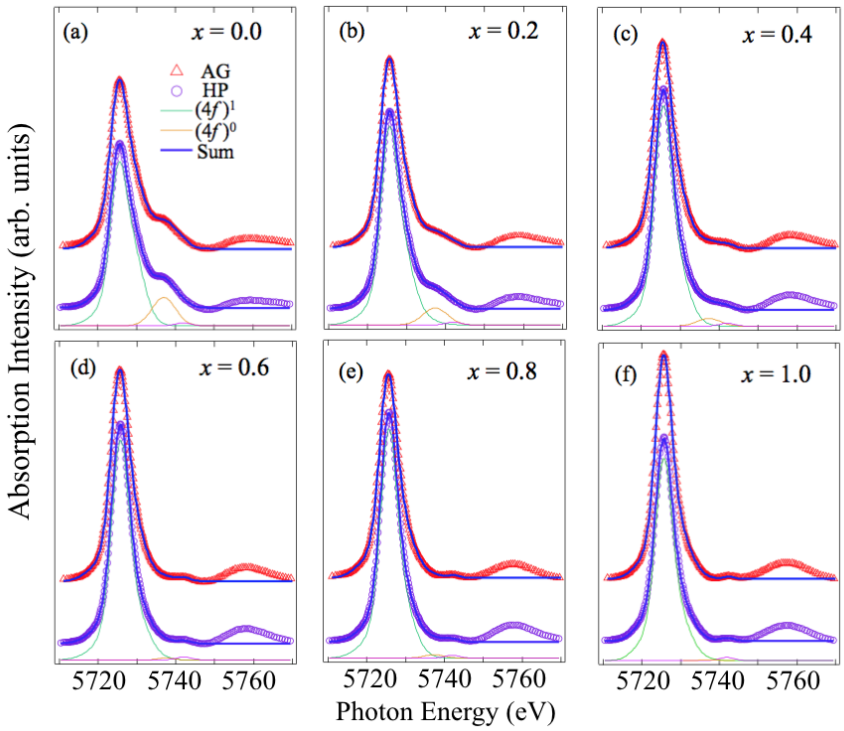

Figure 7.7: Multi-curve fitting results on Ce L_3-edge XAS spectra in $CeO_{1-x}F_xBiS_2$ with (a) $x = 0.0$, (b) $x = 0.2$, (c) $x = 0.4$, (d) $x = 0.6$, (e) $x = 0.8$, and (f) $x = 1.0$. The experimental data of AG and HP are shown as triangles and circles, respectively. The fitted results are shown by solid lines on the HP and AG experimental data. Each component of the fitting lines is shown only for the HP experimental data. The tiny peak around 5742 eV is fixed for all the cases from (a) to (f).

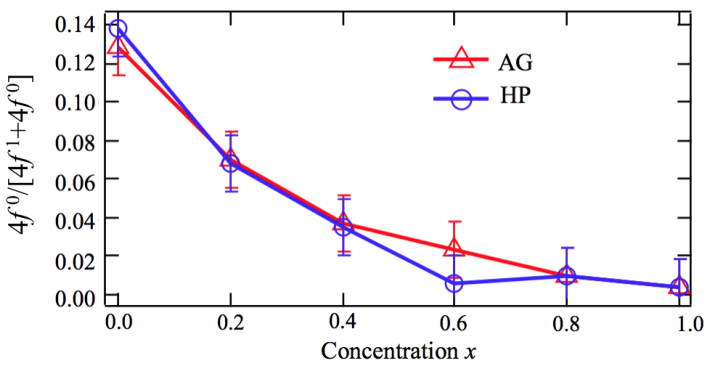

Figure 7.8: The relative spectral weight of $4f^0$ states with respect to the doping amout x for both AG and HP $CeO_{1-x}F_xBiS_2$ samples.

Electronic structure; Ce $4f^1$ and Ce $4f^0$ features

In order to qualify the electronic states, we have estimated the spectral weight of $4f^1$ and $4f^0$ absorption peaks using the following procedure. A constant background estimated by an arctangent function was subtracted from the XAS spectra (inset of Fig. 7.6). The background-subtracted spectra were fitted by Gaussian functions, reproducing all the main peaks, *i.e.*, $4f^1 + 4f^0$ as shown in Fig. 7.7. As for the $4f^1$ peak, we utilized three Gaussian functions to reproduce the asymmetric line shape, while a symmetric Gaussian function was enough to describe the $4f^0$ peak. The $4f^0$ peak is found to decrease monotonically with the F-doping. The fit of the weak peak (peak around 5742 eV, characteristic feature of layered structures) is fixed for all the fits since this feature is independent of the F-doping. The weak peak was used in the fit in order to ensure the proper area estimation of the $4f^0$ peak. The CR was not considered in the fit. The fit for all the samples are shown along with the experimental results.

The intensity of the main peaks $4f^1 + 4f^0$ depends on the amount of additional background from the grain boundaries and the hybridization between the Ce $4f$ and Ce $5d$ orbitals which can be changed by the F-doping and the high pressure synthesis. Therefore, we employ the relative spectral weight $4f^0/[4f^1+4f^0]$, which is obtained by integrating the Gauss functions and is shown in Fig. 7.8, in order to discuss the Ce valence. The relatively large $4f^0/[4f^1 + 4f^0]$ value in CeOBiS$_2$ indicates that the Ce^{4+} state with $4f^0$ electronic configuration is coexisting with the Ce^{3+} state with $4f^1$ electronic configuration [91, 95, 96]. The existence of the $4f^0$ peak, namely, the valence fluctuation between the Ce^{3+} and Ce^{4+} states in CeOBiS$_2$ is in sharp contrast to the pure Ce^{3+} state in iron-based CeOFeAs pnictides [98, 99]. The $4f^0/[4f^1 + 4f^0]$ value decreases with the F-doping both in the AG and HP samples. The $4f^0/[4f^1 + 4f^0]$ value of the AG sample is slightly larger than the HP sample at x=0.6, which is located between the Ce^{3+}/Ce^{4+} valence fluctuation regime and the Ce^{3+} Kondo-like regime. The small $4f^0/[4f^1 + 4f^0]$ value at x=0.6 in the HP sample would be consistent with the fact that the superconductivity and ferromagnetism tend to be enhanced in the HP samples. However, the difference in $4f^0/[4f^1 + 4f^0]$ is very subtle, suggesting that some additional factors such as inhomogeneity play important role in the difference between the AG and HP samples.

Local structure; continuum resonance

Recalling the atomic structure, the layered structure of CeOBiS$_2$ contains BiS$_2$ layer intercalated with CeO layer. The in-plane S atoms in the BiS$_2$ layer (S1 as in Fig. 7.9 (a)) are located at a distance of about 2.8 Å from Bi atoms while the out-of-plane S (S2 as in Fig. 7.9(a)) atom linking the spacer layer with the BiS$_2$ plane is located at a distance of about 2.6 Å. By the F-substitution, the Bi-S2 distance

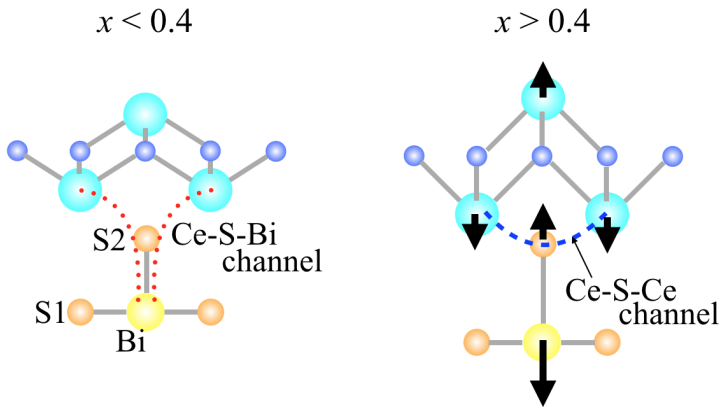

Figure 7.9: The local structure of $CeO_{1-x}F_xBiS_2$ for $x < 0.4$ and for $x > 0.4$. The bond length of Ce-S2 decreases and that of Bi-S2 increases when $x > 0.4$ as depicted.

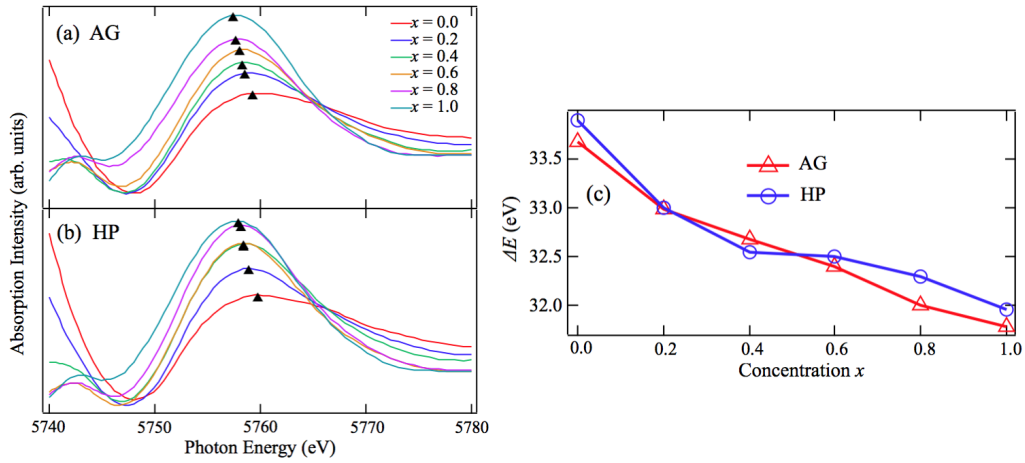

Figure 7.10: Evolution of the CR as a function of the F-doping in (a) AG samples and (b) HP samples. Peak positions are indicated by small triangles. (c) Changes of the energy relative to the absorption white line (ΔE) as a function of the F-doping.

increases ($\Delta R_{\text{max}} \sim 0.12$Å) while Ce-S2 distance decreases ($\Delta R_{\text{max}} \sim 0.15$Å), [91, 100] leading to breaking of the Ce-S-Bi coupling channel as in Fig. 7.9 (b) to (c). Consequently, the hybridization between the Ce $4f$ orbital and the Bi $6p$ conduction band decreases with the F-doping and the Ce^{3+}/Ce^{4+} valence fluctuation is suppressed. This means that the F-doping drives the system from the Ce^{3+}/Ce^{4+} valence fluctuation and/or mixed valence regime to the Ce^{3+} Kondo-like regime [96]. Indeed, the Ce $4f^0$ spectral weight almost disappears at $x > 0.4$, where the system shows the superconductivity and the ferromagnetism. Therefore, when one can apply the valence fluctuation regime, the coupling between the Ce $4f$ and Bi $6p$ states is not good for the superconducting state. There is another possibility that the system shows a phase separation; metallic phase due to the self-doping by Ce $4f$ to Bi $6p_x/6p_y$ and insulating phase. The Ce $4f$ electrons are localized in the Kondo regime for $x > 0.4$ and that should be responsible for the ferromagnetism. The ferromagnetic Ce compounds in the Kondo regime are rather uncommon [101–107] and the direct Ce-Ce exchange interaction plays an important role in many cases. In $CeO_{1-x}F_xBiS_2$, the Ce-Ce distance is relatively longer than the ferromagnetic Ce compounds. Therefore, instead of the direct Ce-Ce exchange interaction, the Ce-S-Ce superexchange interaction as in Fig. 7.9 between Ce^{3+} sites is expected to be responsible for the ferromagnetism of the $CeO_{1-x}F_x$ layer. For $x > 0.4$, the ferromagnetic $CeO_{1-x}F_x$ layer is expected to be insulating just like the $LaO_{1-x}F_x$ layer, and is decoupled from the superconducting BiS_2 layer.

Above arguments are consistent with the structural changes observed in the same experiment through the CR peak. The CR peak is due to the Ce-Bi scattering with a contribution from the Ce-Ce. Fig. 7.10 shows a zoom over of the CR peak for the two series of $CeO_{1-x}F_xBiS_2$ samples, with the peak position evolving with the F-doping. The decrease of energy separation between the white line and the CR peak suggests that the Ce-Bi distance is getting elongated following the empirical rule for the CR ($\Delta E \propto 1/d^2$) [94]. The elongation of the Ce-Bi bond length would contribute to the reduction of the Ce-Bi coupling through Ce-S-Bi channel. Namely, the hybridization between the Ce $4f$ orbital and the Bi $6p$ conduction band decreases with the F-doping and the Ce^{3+}/Ce^{4+} valence fluctuation is suppressed. This is consistent with the decrease of the $4f^0/[4f^1 + 4f^0]$ value by the F-doping.

7.2.3 Conclusion

In conclusion, the Ce L_3-edge XAS results on $CeO_{1-x}F_xBiS_2$ shows that the superconductivity and ferromagnetism are suppressed for $x < 0.4$ in the valence fluctuation regime evidenced by the $4f^1$ and $4f^0$ states. The peak position of the CR depends on the F-doping and indicates the Ce-Bi bond length increases with the F-doping. The present experimental results show that $CeOBiS_2$ has the Ce^{3+}/Ce^{4+} valence fluctuation due to the Ce-Bi coupling through Ce-S-Bi channel and that the

superconductivity of the BiS_2 layer tends to be suppressed by the Ce-Bi coupling. The Ce-S-Bi coupling channel is broken by the F-doping. Consequently, the system undergoes a crossover from the valence fluctuation regime for $x < 0.4$ to the Kondo-like regime for $x > 0.4$ in which superconducting BiS_2 layer and the ferromagnetic $CeO_{1-x}F_x$ layer are decoupled and hence coexist. The results provide important information on the role of Ce valence in the coexisting superconductivity and ferromagnetism in the $CeO_{1-x}F_xBiS_2$ system.

7.3 Unusual valence state of Ce $4f$ in Ce(O,F)BiS_2 revealed by XAS and resonant PES

As in the previous section, the XAS study on $CeO_{1-x}F_xBiS_2$ has revealed that the Ce valence is intermediate (mixed valence) and the Ce $4f$ states may contribute to the Fermi surfaces for $x < 0.4$, and the F-doping makes the system crossover from valence fluctuation and/or static mixed valence regime to Kondo-like regime. However, from the magnetic susceptibility measurement on $CeOBiS_2$, Ce $4f$ electrons are found to be in a well-localized state [93], which is inconsistent with the XAS results. In order to identify the role of the Ce $4f$ electrons, we have investigated the electronic states of Ce $4f$ in $CeO_{1-x}F_xBiS_2$ using Ce L_3-edge XAS and Ce $4d$-$4f$ resonant ARPES.

7.3.1 Experimental condition

High-quality single crystals of $CeOBiS_2$ and $CeO_{0.5}F_{0.5}BiS_2$ have been prepared by CsCl flux method [93]. As for the stoichiometry of $x = 0.5$ sample, the observed lattice constant $c = 13.443$Åis reasonable compared with previous studies on Ce(O,F)BiS_2 system [88, 91]. The Ce L_3 XAS measurements were performed at ID21, μXANES beamline of the ESRF, Grenoble. Acquisition was performed at low temperature using a liquid nitrogen cryostat. The resonant ARPES measurements with linearly polarized photons were performed at the undulator beamline BL-1 of HSRC, Hiroshima University. The photon energy was set to be 30 - 130 eV. We cleaved the single crystalline sample *in situ* under ultrahigh vacuum ($< 1 \times 10^{-10}$ Torr) to obtain clean (001) surface. The total energy resolutions were measured to be 21 meV and 103 meV at $h\nu$ =30 eV and $h\nu$ =120 eV, respectively. The angular resolution was 0.7 deg., corresponding to 0.032 $Å^{-1}$ for 30 eV and 0.067 $Å^{-1}$ for 130 eV in momentum space. All the ARPES measurements were performed at 50 K with p-polarization geometry, that can collect the Bi $6p_x$ and $6p_z$ electrons near the Fermi level (E_F) in the Γ-X (k_x) direction.

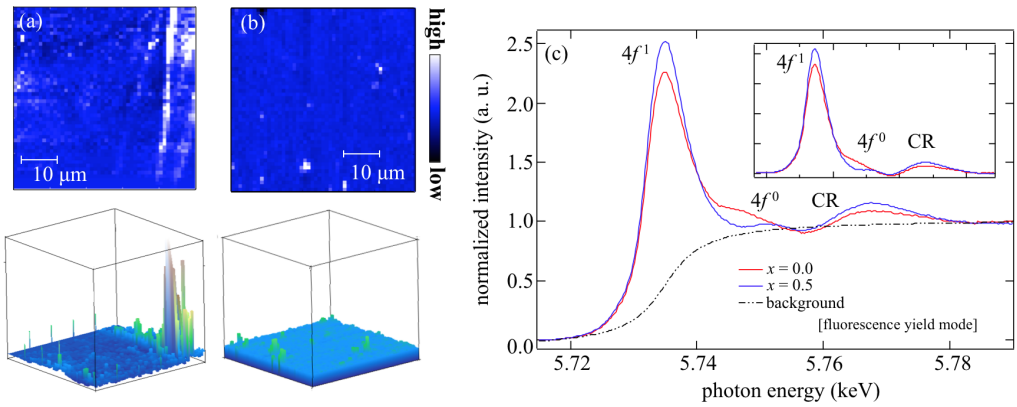

Figure 7.11: (Color online) (a) Real space image of μXANES at Ce L_3-edge (5.732 keV) on CeOBiS$_2$ (b) and on CeO$_{0.5}$F$_{0.5}$BiS$_2$. (c) Normalized XAS spectra of CeOBiS$_2$ and CeO$_{0.5}$F$_{0.5}$BiS$_2$. The background (arctangent function) is denoted by the dot-dashed line. The spectra after background subtraction are also shown in the inset.

7.3.2 Results and discussion

Space-resolved Ce L_3-edge XAS study

Figures 7.11(a) and 7.11(b) show the real space 50 μm $\times$ 50 μm images of XAS intensities at Ce L_3-edge (5.732 keV) on CeOBiS$_2$ and CeO$_{0.5}$F$_{0.5}$BiS$_2$, respectively. From these images, one can see that the Ce $4f$ electronic states are spatially homogeneous in this scale. We also confirmed that the spectral shape at the dark spot is the same as that of the bright spot, indicating that the intensity modulation is not derived from electronic inhomogeneity.

Figure 7.11(c) shows the normalized Ce L_3-edge XAS spectra of CeOBiS$_2$ and CeO$_{0.5}$F$_{0.5}$BiS$_2$. The spectra were normalized with respect to the atomic absorption estimated by a linear fit to the high energy part of the spectra as used in the previous section. The background (arctangent function) is shown by the dot-dashed line. The background-subtracted spectra are also shown in the inset with the same energy and intensity scales. Three main structures around 5.732, 5.745, and 5.768 keV can be identified in the Ce L_3-edge XAS spectra. The first (second) feature is the transition from Ce $2p$ to Ce $5d$ mixed with $4f^1$ ($4f^0$) final state [95–98]. The coexistence of the first and second peaks suggests that Ce^{3+} and Ce^{4+} coexist in the system. Here, the spatially homogeneous XAS map indicates that the observed f^0/f^1 mixed valence is not due to CeO$_2$ impurities but is an intrinsic physics. The third feature is so-called continuum resonance (CR) derived from the Ce-Bi scattering, and reflects the Ce-Bi bondlength. In addition to the three main features, there is a weak structure around 5.75 keV. This is the typical structure of layered rare-earth system, and its intensity is sensitive to the O/F atomic order/disorder in

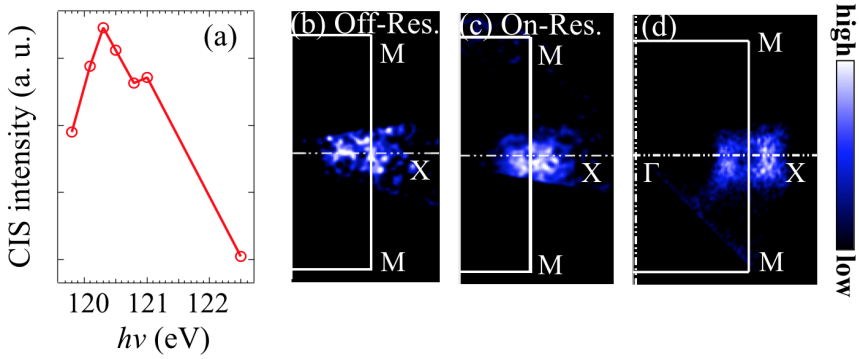

Figure 7.12: (Color online) (a) CIS plot of $CeO_{0.5}F_{0.5}BiS_2$, indicating that the on-resonant photon energy is about 120.3 eV. Fermi surfaces of $CeO_{0.5}F_{0.5}BiS_2$ taken with p-polarization setup (b) at on-resonant photon energy (120.3 eV) and (c) at off-resonant photon energies of 115.4 eV and (d) at 30 eV. The ARPES intensities are integrated within $\pm$ 50 meV with respect to E_F. (e) Cut along M-Γ-X with off-resonant photon energy and (e') its second derivative, (f) cut with on-resonant photon energy, (i) EDCs integrated along M-Γ-X for both off- and on-resonant photon energies, and the inset shows the expanded view near E_F on $CeOBiS_2$. (g), (g'), (h), and (j) are the same as (e), (d), and (i) but on $CeO_{0.5}F_{0.5}BiS_2$.

Ce(O,F) layer. All the XAS results are quantitative consistent with the results of the Ce L_3-edge XAS results of polycrystalline $CeO_{1-x}F_xBiS_2$ shown in the previous section. However, the inconsistency with the magnetic susceptibility measurement still remains; in $CeOBiS_2$, the XAS result suggests that the Ce $4f$ electrons are valence fluctuating whereas the magnetic susceptibility measurement found Ce $4f$ well-localized. We have performed Ce $4d$-$4f$ resonant ARPES on the $CeOBiS_2$ and $CeO_{0.5}F_{0.5}BiS_2$ single crystals in order to investigate the Ce $4f$ electronic states and specify the orbitals mixing with the Ce $4f$ in $CeOBiS_2$.

Ce $4d$-$4f$ resonant ARPES study

Figure 7.12(a) shows constant initial state (CIS) plot with respect to photon energy at the Ce $4f$ peak of $CeO_{0.5}F_{0.5}BiS_2$ normalized by photon flux, which determines the Ce $4d$-$4f$ on-resonant photon energy of the system as 120.3 eV. Figures 7.12(b) and 7.12(c) show the Fermi surface maps of $CeO_{0.5}F_{0.5}BiS_2$ at off-resonant 115.4 eV and on-resonant 120.3 eV. They are obtained by rotating the azimuthal angle with respect to the crystallographic c axis of the sample. Since there is no considerable changes in Fermi surfaces with the on- and off-resonant photon energies, the Ce $4f$ electrons are not employed as a part of the Fermi surfaces. The Fermi surfaces measured at 30 eV are shown in Fig. 7.12(d).

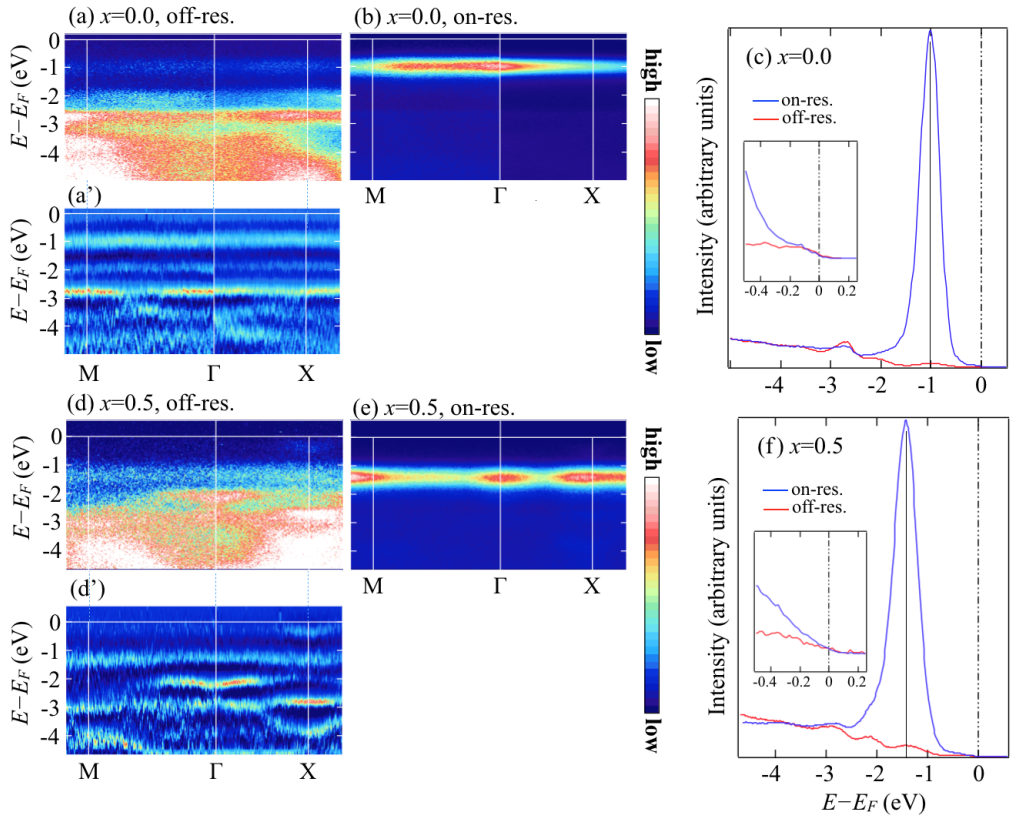

Figure 7.13: (a) Cut along M-Γ-X with off-resonant photon energy and (a') its second derivative, (b) cut with on-resonant photon energy, (c) EDCs integrated along M-Γ-X for both off- and on-resonant photon energies, and the inset shows the expanded view near E_F on $CeOBiS_2$. (d), (d'), (e), and (f) are the same as (a),(a'), (b), and (c) but on $CeO_{0.5}F_{0.5}BiS_2$.

Figures 7.13(a) and 7.13(b) (Figs. 7.13(d) and 7.13(e)) show the ARPES data taken at 115.4 eV (off-resonance) and 120.3 eV (on-resonance), respectively, for $CeOBiS_2$ (for $CeO_{0.5}F_{0.5}BiS_2$) along M-Γ-X. Figures 7.13(c) and 7.13(f) respectively show the energy distribution curves (EDCs) integrated along M-Γ-X taken for $CeOBiS_2$ and $CeO_{0.5}F_{0.5}BiS_2$ at on- and off-resonant photon energies, and the inset shows the expansion near E_F. One can see from the EDCs [Figs. 7.13(c) and 7.13(f)] that the structures A, B, and C of $CeO_{0.5}F_{0.5}BiS_2$ are roughly shifted to the higher binding energy by 0.4 eV due to the electron doping compared with those of $CeOBiS_2$, but one can also see there is a slight band-dependence of the shifts, which could be due to local atomic structural changes [100]. The on-resonance spectra are dominated by the partial density of states (DOS) of Ce $4f$ due to the resonant enhancement. If the system is in a conventional valence fluctuating regime, the on-resonant spectrum considerably enhances two features; at approximately 0

eV (f^0 component) due to a strong cf hybridization and at -1.0 eV (f^1 component) in $CeOBiS_2$ [at 0 eV (f^0) and at -1.4 eV (f^1) in $CeO_{0.5}F_{0.5}BiS_2$] with respect to E_F. On the other hand, if the system is in a Kondo-like regime, the on-resonant enhancement can be seen in one feature; at -1.0 eV in $CeOBiS_2$ (at -1.4 eV in $CeO_{0.5}F_{0.5}BiS_2$) with respect to E_F, which is f^1 component [108].

In $CeO_{0.5}F_{0.5}BiS_2$, the Bi $6p$ Fermi pocket around X point is observed in both the on- and off-resonance data. The valence band below -1 eV can be assigned to Bi $6s$, S $3p$, and Ce $4f$ bands. When the photon energy is tuned to the Ce $4d$-$4f$ absorption energy (120.7 eV), the flat band located at -1.4 eV is considerably enhanced. The resonant ARPES results show that the Ce $4f$ band is located between the Bi $6p$ conduction band and the Bi $6s$/S $3p$ valence band, and that there is no appreciable Ce $4f$ spectral weight at E_F. Namely, the results indicate that the Ce $4f$ electrons are basically localized (Kondo-like regime), do not contribute to the Fermi pockets around X, and its valance should be $3+$. This result on $CeO_{0.5}F_{0.5}BiS_2$ is consistent with the bulk sensitive Ce L_3-edge XAS result where $CeOBiS_2$ falls in the valence fluctuation regime and gradually changes to the Kondo-like regime with the F substitution for O as in the previous section. The superexchange or RKKY interaction between the localized Ce $4f$ moments is derived from the Ce $4f$-S $3p$ hybridization.

On the other hand, in $CeOBiS_2$, we found that the Ce $4f$ lineshape is very similar to that of $CeO_{0.5}F_{0.5}BiS_2$ as shown in Figs. 7.12(i) and 7.12(j), and is different from what one expected for valence fluctuating systems. In typical valence fluctuating systems such as $CeRu_2$, the Ce $4f$ band is strongly hybridized with the conduction band such as Ru $4d$ and is well reproduced by LDA band calculations. The observed Ce $4f$ band of $CeOBiS_2$ has very flat dispersion and does not agree with the LDA band calculation [109]. Here we speculate following two scenarios; (i) the Ce $4f$ electrons in $CeOBiS_2$ are mixed with the unoccupied Bi $6p_z$. From the crystal structure, the nearest ion for Ce is oxygen, but the oxygen band is located far from E_F by 3 - 4 eV and therefore hard to hybridize with the Ce $4f$. The other candidate for the mixing partner of the Ce $4f$ is the unoccupied Bi $6p_z$ through the out-of-plane S. Since the Bi $6p_z$ orbitals do not contribute to the Fermi surfaces, one electron in the Ce $4f$ orbitals should be completely transferred to the Bi $6p_z$ orbitals in order to obtain the f^0 component in the Ce L_3 XAS. However, if the electron transfer from the Bi $6s$ orbitals to the Ce $4f$ orbitals is included, the mixture of the f^1 and f^0 states becomes possible and the Ce L_3 XAS result would be explained. Note that the Ce $4f$-Bi $6p_z$ hybridization does not necessarily leads to a metallic state. It provides the mixed valence state given by the linear combination of $|4f^1\rangle$ and $|4f^0\ L^1\rangle$ where L is Bi $6p_z$. This state can be localized if the overlap between the neighboring Bi $6p_z$ states is sufficiently small compared with the intersite Coulomb repulsive energy. Even if the overlap is not small enough for the localization due to the pure Coulomb interaction, the combination of the Coulomb interaction and

the atomic disorder [100] can provide an insulating ground state, possibly a sort of charge glass of Bi $6p_z$ electrons. Moreover, this hybridization may impede the ferromagnetic order in the Ce(O,F) layer. The second scenario is as indicated in the previous section, (ii) the system shows the phase separation; metallic and insulating phases. The metallic phase can appear due to the self-doping given by the Ce $4f$ electrons. If all the electrons of Ce $4f$ orbital are introduced to the Bi $6p_x/6p_y$, the metallic phase appear about 15 % of the sample.

Anderson's impurity model analysis on Ce L_3-edge XAS results

In order to examine this possibility, we have performed Anderson's impurity model (AIM) calculation on Ce L_3-edge XAS results under the condition that the Ce $4f$ is mixing with the unoccupied Bi $6p_z$ and the occupied Bi $6s$. The model Hamiltonian is given by the standard Anderson Hamiltonian including the Ce $4f$ and $5d$ electrons, the conduction-band electrons, and the Ce $2p$ core-level electrons.

$$\begin{aligned}\mathscr{H}_{\mathrm{A}} = &\sum_k \varepsilon_k c_k^\dagger c_k + \varepsilon_f \sum_m f_m^\dagger f_m + U_f \sum_{m'>m} f_{m'}^\dagger f_{m'} f_m^\dagger f_m + n_{\mathrm{c}}\varepsilon_{\mathrm{c}} \\ &+ (1-n_{\mathrm{c}})Q_f \sum_m f_m^\dagger f_m + \sum_{mk}(V_{mk} c_k^\dagger f_m + V_{mk}^* f_m^\dagger c_k) \\ &+ \varepsilon_d \sum_m d_m^\dagger d_m + U_{fd} \sum_{m'>m} f_{m'}^\dagger f_{m'} d_m^\dagger d_m + (1-n_{\mathrm{c}})Q_d \sum_m d_m^\dagger d_m, \end{aligned} \tag{7.2}$$

Here, $f_m^\dagger$ ($d_m^\dagger$) are creation operators for the Ce $4f$ ($5d$) electrons with orbital notation m, and $c_k^\dagger$ are creation operators for Bloch electrons in the Bi $6p_z$ and Bi $6s$ bands for the scenario (i) with wave vector $\boldsymbol{k}$ [they can be Bloch electrons in the Bi $6p_x/6p_y$ and Bi $6s$ bands for the scenario (ii)]. The parameters U_f and Q_f (Q_d) are the on-site repulsive Coulomb interaction between the Ce $4f$ electrons and the attractive Coulomb interaction between the Ce $4f$ ($5d$) electron and the Ce $2p$ core hole, and U_{fd} is the on-site repulsive Coulomb interaction between the Ce $4f$ and Ce $5d$ electrons. Note that the notations m and k include spin. The parameter V describes the transfer integral between the Ce $4f$ and conduction-band electrons, ε_f (ε_d) is the energy level of Ce $4f$ ($5d$) electrons relative to the Fermi level, and $\varepsilon_{\mathrm{c}}/n_{\mathrm{c}}$ represent the energy/number of the Ce $2p$ core-level electron.

In the Ce L_3-edge XAS process, the absorption occurs from the Ce $2p$ core level to the Ce $5d$ unoccupied states mixed with the Ce $4f$ states. In the framework of the Anderson's impurity model, the initial state can be simply given by

$$|\psi_i\rangle = \alpha|4f^0\ L^1\rangle + \beta|4f^1\rangle + \gamma|4f^2\ \underline{L}^1\rangle \tag{7.3}$$

where L and $\underline{L}$ denote a Bi $6p_z$ electron for scenario (i) [Bi $6p_x/6p_y$ electron for scenario (ii)] and Bi $6s$ hole, respectively. The final states are given by

$$|\psi_f\rangle = \alpha'|\underline{c}\ 4f^0\ L^1\ 5d^1\rangle + \beta'|\underline{c}\ 4f^1\ 5d^1\rangle + \gamma'|\underline{c}\ 4f^2\ \underline{L}^1\ 5d^1\rangle \tag{7.4}$$

where $\underline{c}$ denotes the Ce $2p$ core hole. Using α, β, γ, α', β', and γ', the spectral weight is given by $|\alpha\alpha' + \beta\beta' + \gamma\gamma'|^2$. The energy of the $|\underline{c}\ 4f^0\ L^1\ 5d^1\rangle$ state is given by $\varepsilon_d - Q_d$, that of the $|\underline{c}\ 4f^1\ 5d^1\rangle$ is given by $\varepsilon_f + \varepsilon_d - Q_f - Q_d + U_{fd}$, and that of $|\underline{c}\ 4f^2\ \underline{L}^1\ 5d^1\rangle$ is given by $2\varepsilon_f + \varepsilon_d - 2Q_f - Q_d + U_f + 2U_{fd}$.

The parameters U_{fd} and Q_d are neglected in the present analysis because they are substantially small compared with the other parameters. Since ε_f can be determined by the Ce $4d$-$4f$ resonant ARPES results and Q_f is fixed at $U_f/0.8$ [110,111], the present analysis includes two free parameters; U_f and T, where the effective transfer integral $T = \sqrt{\sum_{mk} \mid V_{mk} \mid^2}/\sqrt{N}$ with N = 14 (see Fig. 7.14(a)) represents the off diagonal term. The dominator is due to the degeneracy of f orbital.The $|f^1\rangle$ and $|f^2\rangle$ state can be described by the linear combination of f-orbitals as

$$\begin{aligned}
|f^1\rangle &= \frac{1}{\sqrt{{}_{14}\mathrm{C}_1}}[|\mathfrak{f}^1;1\rangle + |\mathfrak{f}^1;2\rangle + \cdots + |\mathfrak{f}^1;14\rangle] \\
&= \frac{1}{\sqrt{{}_{14}\mathrm{C}_1}}\sum_{\alpha=1}^{1} 4|\mathfrak{f}^1;\alpha\rangle \qquad (7.5)\\
|f^2\rangle &= \frac{1}{\sqrt{{}_{14}\mathrm{C}_2}}[|\mathfrak{f}^2;1,2\rangle + |\mathfrak{f}^2;1,3\rangle + \cdots + |\mathfrak{f}^2;13,14\rangle] \\
&= \frac{1}{\sqrt{{}_{14}\mathrm{C}_2}}\sum_{\beta\neq\alpha}^{14} |\mathfrak{f}^2;\alpha,\beta\rangle \qquad (7.6)
\end{aligned}$$

where α/β stands for the orbital notation including spin, and $|\mathfrak{f}\rangle$ especially denotes the specific orbital states. Then the transfer integral from $|f^0\rangle$ state to $|f^1\rangle$ state is

$$\begin{aligned}
\sqrt{\sum_{mk} \mid V_{mk}^{(01)} \mid^2} &= \langle f^0\ L^1|\mathscr{H}_{\mathrm{A}}|f^1\rangle \\
&= \langle f^0\ L^1|\mathscr{H}_{\mathrm{A}}|\frac{1}{\sqrt{14}}\sum_{\alpha=1}^{14}|\mathfrak{f}^1;\alpha\rangle = \sqrt{14}T \qquad (7.7)
\end{aligned}$$

and the transfer integral from $|f^1\rangle$ state to $|f^2\rangle$ state is

$$\begin{aligned}
\sqrt{\sum_{mk} \mid V_{mk}^{(12)} \mid^2} &= \langle f^1|\mathscr{H}_{\mathrm{A}}|f^2\ \underline{L}^1\rangle \\
&= \frac{1}{\sqrt{{}_{14}\mathrm{C}_1 \cdot {}_{14}\mathrm{C}_2}}\sum_{\beta\neq\alpha}^{14}\langle\mathfrak{f}^1;\alpha|\mathscr{H}_{\mathrm{A}}|\mathfrak{f}^2\ \underline{L}^1;\alpha,\beta\rangle \\
&= \sqrt{\frac{2}{14\cdot 14\cdot 13}}\cdot 14\times 13\langle\mathfrak{f}^1|\mathscr{H}_{\mathrm{A}}|\mathfrak{f}^2\ \underline{L}^1\rangle \\
&= \sqrt{2}\cdot\sqrt{13}T \qquad (7.8)
\end{aligned}$$

where non-zero terms are $T = \langle\mathfrak{f}^1;\alpha|\mathscr{H}_{\mathrm{A}}|\mathfrak{f}^2;\alpha,\beta\rangle$ or $\langle\mathfrak{f}^1;\beta|\mathscr{H}_{\mathrm{A}}|\mathfrak{f}^2;\alpha,\beta\rangle$. Each orbital state α has 13 non-zero terms. This is why the coefficient 14×13 appears. For

simplicity, the effective transfer integral is the same for the Bi $6p_z$ and $6s$ orbitals. Then the matrix representation of the Anderson Hamiltonian without impurity levels for initial and final states are

$$\mathscr{H}_{\mathrm{A}}^{\mathrm{ini}} = \begin{bmatrix} 0 & \sqrt{14}T & 0 \\ \sqrt{14}T & \varepsilon_f & \sqrt{2}\cdot\sqrt{13}T \\ 0 & \sqrt{2}\cdot\sqrt{13}T & 2\varepsilon_f + U_f \end{bmatrix} \tag{7.9}$$

and

$$\mathscr{H}_{\mathrm{A}}^{\mathrm{fin}} = \begin{bmatrix} \varepsilon_0 & \sqrt{14}T & 0 \\ \sqrt{14}T & \varepsilon_0 + \varepsilon_f - Q_f & \sqrt{2}\cdot\sqrt{13}T \\ 0 & \sqrt{2}\cdot\sqrt{13}T & \varepsilon_0 + 2\varepsilon_f + U_f - 2Q_f \end{bmatrix}. \tag{7.10}$$

Here we introduce equally spaced 10 impurity levels to this Hamiltonian. The size of the matrix is 56×56; 1×1 for $|f^0\ L^1\rangle$, ${}_{10}\mathrm{C}_1 \times {}_{10}\mathrm{C}_1$ for $|f^1\rangle$, and ${}_{10}\mathrm{C}_2 \times {}_{10}\mathrm{C}_2$ for $|f^2\ \underline{L}^1\rangle$ states. In this calculation, we define the transfer integral as

$$T^2 = \sum_{i=1}^{10} \left|\langle f^0\ L^1|\mathscr{H}_{\mathrm{A}}|\mathfrak{f}^1\rangle\right|^2 = \sum_{i=1}^{10} \left|\langle \mathfrak{f}^1|\mathscr{H}_{\mathrm{A}}|\mathfrak{f}^2\ \underline{L}^1\rangle\right|^2 \tag{7.11}$$

where n is the impurity level, and the transfer integral is n-independent. Therefore, it is necessary to normalize the effective transfer integral as

$$\langle f^0\ L^1|\mathscr{H}_{\mathrm{A}}|f^1\rangle = \sqrt{\frac{14}{10}}T \tag{7.12}$$

$$\langle f^1|\mathscr{H}_{\mathrm{A}}|f^2\ \underline{L}^1\rangle = \sqrt{\frac{2\cdot 13}{10}}T. \tag{7.13}$$

The diagonal term of the f^1 state with impurity level i ($1 \le i \le 10$) is

$$\mathscr{H}_{\mathrm{A}}^{\mathrm{ini}}(n,n) = \varepsilon_f + \frac{i-5.5}{10}\cdot W \tag{7.14}$$

where $n = i+1$ ($\Leftrightarrow 2 \le n \le 11$), and the diagonal and off-diagonal terms of the f^2 state with impurity levels i and j ($1 \le i \le 10, i+1 \le j \le 10$) are described by

$$\mathscr{H}_{\mathrm{A}}^{\mathrm{ini}}(n,n) = 2\varepsilon_f + U_f + \frac{(i+j)-11}{10}\cdot W \tag{7.15}$$

$$\mathscr{H}_{\mathrm{A}}^{\mathrm{ini}}(n,i+1) = \sqrt{\frac{2\cdot 13}{10}}\cdot T \tag{7.16}$$

$$\mathscr{H}_{\mathrm{A}}^{\mathrm{ini}}(n,j+1) = \sqrt{\frac{2\cdot 13}{10}}\cdot T \tag{7.17}$$

where W stands for the band width of the impurity level, n can be described as $n^{ij} = \sum_{l=1}^{i}(11-l) + (j-i+1)$ [$\Leftrightarrow 12 \le n \le 56$] , and the values 5.5 and 11 in the diagonal terms of the f^1 and f^2 state are due to the weighted average of 1-10 ($i_{\mathrm{min}} - i_{\mathrm{max}}$) and 3-19 ($[i+j]_{\mathrm{min}} - [i+j]_{\mathrm{max}}$). Then the matrix representation of the Hamiltonians is as follows.

$$
\mathscr{H}_{\mathrm{A}}^{\mathrm{ini}} = \left(\begin{array}{c|ccccc|ccccc}
0 & \sqrt{\frac{14}{10}}\cdot T & \sqrt{\frac{14}{10}}\cdot T & \dots & \sqrt{\frac{14}{10}}\cdot T & \sqrt{\frac{14}{10}}\cdot T & & & 0 & & \\
\hline
\sqrt{\frac{14}{10}}\cdot T & \varepsilon_f + \frac{1-5.5}{10}\cdot W & & & & & \sqrt{\frac{2\cdot 13}{10}}\cdot T & \sqrt{\frac{2\cdot 13}{10}}\cdot T & \dots & & \\
\sqrt{\frac{14}{10}}\cdot T & & \varepsilon_f + \frac{2-5.5}{10}\cdot W & & & & \sqrt{\frac{2\cdot 13}{10}}\cdot T & & & & \\
\vdots & & & \ddots & & & \vdots & & \ddots & & \vdots \\
\sqrt{\frac{14}{10}}\cdot T & & & & \varepsilon_f + \frac{9-5.5}{10}\cdot W & & & & & & \sqrt{\frac{2\cdot 13}{10}}\cdot T \\
\sqrt{\frac{14}{10}}\cdot T & & & & & \varepsilon_f + \frac{10-5.5}{10}\cdot W & & & \dots & \sqrt{\frac{2\cdot 13}{10}}\cdot T & \sqrt{\frac{2\cdot 13}{10}}\cdot T \\
\hline
 & \sqrt{\frac{2\cdot 13}{10}}\cdot T & \sqrt{\frac{2\cdot 13}{10}}\cdot T & \dots & & & 2\varepsilon_f + U_f + \frac{(1+2)-11}{10}\cdot W & & & & 0 \\
 & \sqrt{\frac{2\cdot 13}{10}}\cdot T & & & & & & 2\varepsilon_f + U_f + \frac{(1+3)-11}{10}\cdot W & & & \\
0 & \vdots & & \ddots & & \vdots & & & \ddots & & \\
 & & & & & \sqrt{\frac{2\cdot 13}{10}}\cdot T & & & & 2\varepsilon_f + U_f + \frac{(8+10)-11}{10}\cdot W & \\
 & & & \dots & \sqrt{\frac{2\cdot 13}{10}}\cdot T & \sqrt{\frac{2\cdot 13}{10}}\cdot T & & & & & 2\varepsilon_f + U_f + \frac{(9+10)-11}{10}\cdot W
\end{array}\right)
$$

$$
\mathscr{H}_{\mathrm{A}}^{\mathrm{fin}} = \left(\begin{array}{c|ccccc|ccc}
\varepsilon_0 & \sqrt{\frac{14}{10}}\cdot T & \sqrt{\frac{14}{10}}\cdot T & \dots & \sqrt{\frac{14}{10}}\cdot T & \sqrt{\frac{14}{10}}\cdot T & & & \\
\hline
\sqrt{\frac{14}{10}}\cdot T & \varepsilon_0 + \varepsilon_f + \frac{1-5.5}{10}\cdot W - Q_f & & & & & & \sqrt{\frac{2\cdot 13}{10}}\cdot T & \dots \\
\sqrt{\frac{14}{10}}\cdot T & & \varepsilon_0 + \varepsilon_f + \frac{2-5.5}{10}\cdot W - Q_f & & & & & \sqrt{\frac{2\cdot 13}{10}}\cdot T & \\
\vdots & & & \ddots & & & & \vdots & \\
\sqrt{\frac{14}{10}}\cdot T & & & & \varepsilon_0 + \varepsilon_f + \frac{9-5.5}{10}\cdot W - Q_f & & & & \\
\sqrt{\frac{14}{10}}\cdot T & & & & & \varepsilon_0 + \varepsilon_f + \frac{10-5.5}{10}\cdot W - Q_f & & & \\
\hline
 & \sqrt{\frac{2\cdot 13}{10}}\cdot T & \sqrt{\frac{2\cdot 13}{10}}\cdot T & \dots & & & \varepsilon_0 + 2\varepsilon_f + U_f + \frac{(1+2)-11}{10}\cdot W - 2Q_f & & \\
 & \sqrt{\frac{2\cdot 13}{10}}\cdot T & & & & & & & \ddots \\
0 & \vdots & & \ddots & & & & &
\end{array}\right)
$$

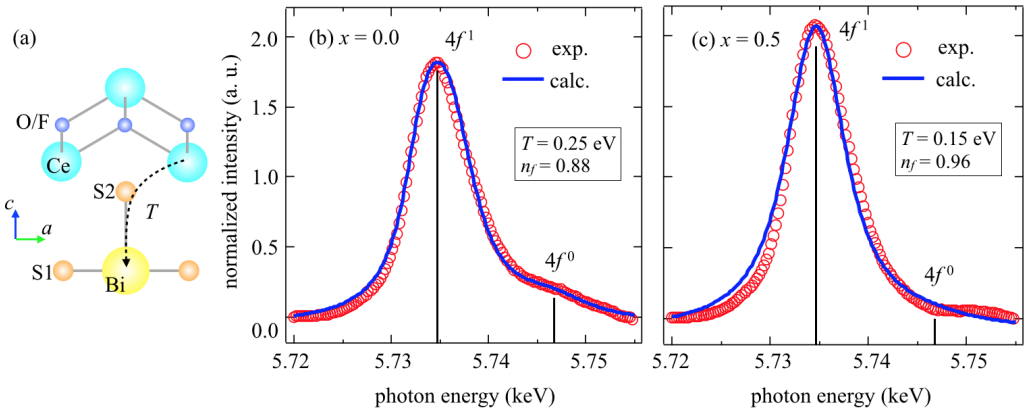

Figure 7.14: (a) Schematic diagram of the effective transfer integral T. Ce L_3-edge XAS experimental results on single crystal $CeO_{1-x}F_xBiS_2$ and corresponding impurity model calculations at (b) $x = 0.0$ and (c) $x = 0.5$. The energy positions of $4f^1$ and $4f^0$ are shown by vertical lines. The effective transfer integral (T) and number of Ce $4f$ electrons (n_f) estimated by Anderson's impurity-model calculation are also shown here.

The fixed parameters are summarized in Tab. 7.3. Since the Hamiltonian for both initial and final states are determined, the eigen states and corresponding coefficients can be obtained by numerically diagonalizing the Hamiltonian, *i.e.*, one can calculate the Ce L_3-edge XAS spectra and expectation value of number of Ce $4f$ electrons (n_f) within the scheme of Anderson Hamiltonian. The parameter n_f can be calculated using the coefficients of initial state as

$$n_f = 0 \times \sum_{i=1}^{1} |\alpha_i|^2 + 1 \times \sum_{i=2}^{11} |\beta_i|^2 + 2 \times \sum_{i=12}^{56} |\gamma_i|^2. \tag{7.18}$$

Considering the local structural changes of Ce, S2 (see Fig. 7.14(a)), and Bi due to the F-doping [100], the parameter T should be the only adjustable parameter to reproduce the XAS spectra. Therefore, the parameter U_f is fixed at 7.8 eV for all the calculations. We have succeeded in reproducing the $4f^1$ and $4f^0$ structures of the XAS spectra, indicating that the scenario above could be possible. The results are shown in Figs. 7.14(b) and 7.14(c) for $x = 0.0$ and 0.5, respectively, and the

Table 7.3: Summary of the electronic-structure parameters for Anderson's impurity model calculation.

$\varepsilon_{pz} - \varepsilon_f$	0.8 eV
$4f$-$4f$ Coulomb interaction U	7.8 eV
$\underline{2p}$-$4f$ Coulomb interaction Q	-9.8 eV
Band width of $4f$	4.0 eV

energy positions of the $4f^1$ and $4f^0$ structures are also shown here. The circles and solid lines are respectively experimental and calculated results, and the evaluated T and n_f are also shown in Fig. 7.14. The parameter T changes from 0.25 eV to 0.15 eV when the F concentration x goes from 0.0 to 0.5. The number n_f is calculated as 0.88 and 0.96 for $x = 0.0$ and 0.5, respectively. Present results are consistent with the thermodynamical quantities since Higashinaka *et al.* reported that the amount of Ce^{3+} ($4f^1$ state) in $CeOBiS_2$ is 10 % lower than expected [93] whereas the AIM calculation gives $n_f = 0.88$.

Our scenarios of both (i) and (ii) could explain the XAS and resonant ARPES results naturally with a support of AIM calculation; (i) the unoccupied Bi $6p_z$ states partially trap Ce $4f$ electrons and form a sort of charge glass state due to the strong atomic disorder of BiS plane. It is expected that the electrons in the Bi $6p_z$ state are randomly distributed in real space and appear as a broad feature in the ARPES spectra. Therefore, it would rather difficult to identify the Bi $6p_z$ state from the comparison between the photoemission results and some calculations considering the atomic disorder in the BiS plane. As for the (ii) scenario, we speculate that the system shows the metallic and insulating phase separation due to the Ce $4f$ self-doping. In future, the theoretical and experimental efforts should be done to confirm the present scenario.

Although it is difficult to estimate the exact value of x of the superconducting sample, it can be safely concluded that we observed the unusual valence state of Ce $4f$ electrons in the $x = 0.0$ system, and it disappears in the superconducting phase.

7.3.3 Conclusion

In summary, we have combined Ce L_3-edge XAS, Ce $4d$-$4f$ resonant PES, and Anderson's impurity model (AIM) calculation on single crystals of $CeO_{1-x}F_xBiS_2$ for $x = 0.0$ and 0.5 in order to investigate the electronic states of Ce $4f$ electrons. As for the XAS, mixed valence state was found in $x = 0.0$ sample and the F-doping suppresses it, which is consistent with those of polycrystalline samples as in the previous section. As for the resonant PES, we found that the Ce $4f$ electrons in both $x = 0.0$ and 0.5 systems are essentially localized and there is no contribution to the Fermi surfaces. We assume that the localized Ce $4f$ in $CeOBiS_2$ is mixed with the unoccupied Bi $6p_z$ instead of Bi $6p_x/6p_y$. This scenario is consistent with the previous local structural study. As for the AIM calculation, the results not only support the scenario, but also are consistent with the thermodynamical experiments [93]. The hybridization of Ce $4f$ and Bi $6p_z$ may impede the ferromagnetic order in the Ce(O,F) layer.

7.4 Eu mixed valence and phase separation in EuFBiS$_2$ probed by XAS and PES

We have investigated the electronic structure of a new member of BiS$_2$-based family EuFBiS$_2$ by means of Eu L_3-edge XAS, Eu $4d$-$4f$ resonant PES, ARPES, and space-resolved PES. The XAS shows that Eu is in the Eu^{2+}/Eu^{3+} mixed valence state, indicating part of electron in Eu is doped in the BiS plane. Using the Eu $4d$-$4f$ resonant PES, we have identified the contribution of Eu^{2+} and Eu^{3+} states in the total DOS. From the ARPES study, there is no electron-like band around X point near Fermi level, which is expected to appear due to the possible self-doped mechanism by Eu. However, we have detect a possible band splitting in in-plane S bands. In order to confirm the cause of this split, we performed space-resolved photoemission experiment. Surprisingly the system shows a mesoscopic electronic phase separation; metallic and insulating phases. We apply the same speculation of Ce(O,F)BiS$_2$ system that in the insulating phase the self-doped electrons are trapped in Bi $6p_z$ orbital due to strong atomic disorder.

7.4.1 Experimental condition

High quality single crystals of EuFBiS$_2$ have been prepared by CsCl method provided by Aoki group of the Tokyo Metropolitan University.

Temperature dependent x-ray absorption spectroscopy was performed at BM25 of ESRF as known as SpLine. All the spectra were taken with transmission mode.

Resonant photoemission spectroscopy was performed at the beamline BL-28A of Photon Factory, KEK. Photon energies are set to be 120 eV - 156 eV. Endstation is equipped with Scienta SES 2002. All the spectra were taken at 20 K.

Polarization dependent ARPES was performed at multi-mode undulator beamline BL-9A of Hiroshima Synchrotron Radiation Center, Hiroshima University. Circularly and linearly polarized photons at 23 eV were employed to excite the photoelectrons that were collected with VG Scienta R4000 analyzer. The total energy resolution including both monochromator and electron energy analyzer was measured to be about 40 meV.

Space-resolved photoemission experiment was performed at Spectromicroscopy beamline, Elettra Syncrotrone Trieste. The incident photon energy tuned at 27 eV was focused down to 600×600 nm^2. The temperature was fixed at 50 K for all the measurements. The total energy resolution including both monochromator and electron energy analyzer was measured to be about 100 meV.

In all the photoemission experiment, single crystalline samples were cleaved *in situ* in ultrahigh vacuum (10^{-10} Pa range) at measurement temperature in order to obtain a clean (001) surface.

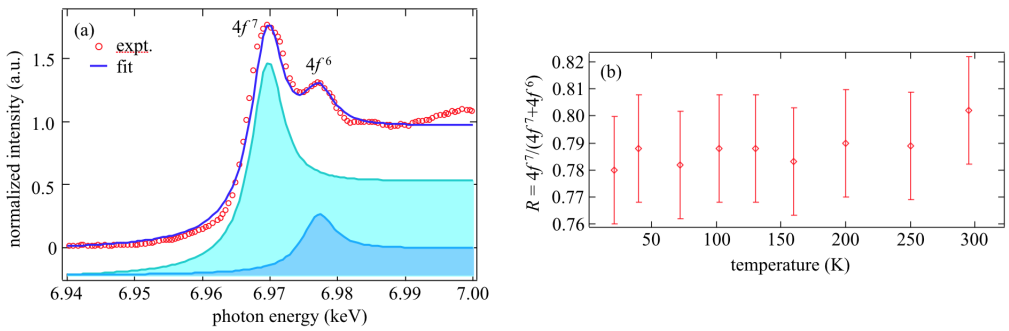

Figure 7.15: (Color online) (a) Eu L_3-edge XAS spectrum taken at 21 K (circles) and its fit (solid line) using $\rho^{\text{fit}}_{\text{XAS}}$. Superposition of two arctangent backgrounds are also shown here. (b) Temperature dependence of the ratio Eu^{2+}/(Eu^{2+}+Eu^{3+}) estimated by the fit.

7.4.2 Results and Discussion

Eu L_3-edge XAS

We have performed Eu L_3-edge XAS measurement at various temperature, and Fig. 7.15(a) shows the Eu L_3-edge XAS spectrum taken at 21 K. All the spectra are normalized with respect to the atomic absorption estimated by a linear fit to the high energy part of the spectra. One can see the structures around 6,969 eV and 6,977 eV, and the first one (second one) is the absorption corresponding to transition from Eu $2p$ core level to unoccupied Eu $5d$ orbitals mixed with $4f^7$ ($4f^6$) final state [112–114]. Coexistence of $4f^7$ and $4f^6$ indicates the mixed valence states of Eu^{2+} and Eu^{3+}. We estimate the ratio of $4f^7$ and $4f^6$ using the fitting function $\rho^{\text{fit}}_{\text{XAS}}$ as follows:

$$\rho^{\text{fit}}_{\text{XAS}} = R \cdot \rho[f^7] + (1 - R) \cdot \rho[f^6]$$
$$\rho[f^n] = A(E_0^{fn}, \Gamma) + L(E_0^{fn}, \gamma)$$

where R stands for the spectral weight ratio $4f^7$/($4f^7$+ $4f^6$), E_0^{fn} is the peak position of $4f^n$, A is the arctangent function for background, and L denotes the Lorentz function. They have the form of

$$A(E_0, \Gamma) = \frac{1}{\pi} \arctan(\frac{E - E_0}{\Gamma}) + \frac{1}{2}$$
$$L(E_0, \gamma) = \frac{c}{\pi} \frac{\gamma}{(E - E_0)^2 + \gamma^2}$$

where $\Gamma = 3.7$ eV is the intrinsic broadening of Eu L_3-edge XAS due to the core hole lifetime [115], c is the amplitude of the Lorentz function, and γ is the broadening width of white line. Therefore, the spectral weight ratio R is the only adjustable

parameter for this fit. The temperature dependence of the R is shown in Fig. 7.15(b), and one can see that $R \sim 80\%$ is mostly fixed value for all the temperature.

Eu $4d$-$4f$ resonant photoemission study

In order to determine the partial DOS of Eu $4f$, we have performed angle-integrated Eu $4d$-$4f$ resonant photoemission spectroscopy. The temperature was fixed at 50 K because the Eu L_3-edge XAS was temperature-independent. Figures 7.16(a) and 7.16(b) show the photoemission spectra taken with $h\nu = 120$ eV up to 156 eV. All the spectra were normalized using photon flux. One can see from Fig. 7.16(a) that there are two enhancements; one is a strong enhancement at $(h\nu, E - E_F)$=(140 eV,-1.3 eV), and the other is relatively weak at $(h\nu, E - E_F)$=(143 eV,-8.3 eV). They can be respectively assigned to the Eu^{2+} and Eu^{3+}, which have the consistent energy positions as previous resonant experiment on a different Eu mixed valence system [116]. Figure 7.16(c) is the constant initial state (CIS) plot at $E = -1.3$ eV (Eu^{2+}) and -8.3 eV (Eu^{3+}). One can see from the CIS plot that there is a pre-edge around $h\nu = 135$ eV in both Eu^{2+} and Eu^{3+}. This type of pre-edge appears often in CIS plot of $4d$-$4f$ resonance and disappears in that of $3d$-$4f$ resonance and/or $3d$-$4f$ XAS [117]. This indicates that this pre-edge is due to the surface state. Indeed, in the present EuFBiS$_2$ system, it was confirmed by Eu $3d$-$4f$ resonant PES and Eu $3d$-$4f$ XAS that this pre-edge was actually disappeared [118]. Therefore, we assign this pre-edge as a surface state. In the Fig. 7.16(c), the CIS plot of Eu^{2+} has one peak while that of Eu^{3+} has two peaks besides the pre-edge. The former can be understood as a standard Fano profile, which consists of one discrete and one continuum. The latter may be due to the two discrete states; one is spin-up hole, and the others are spin-down holes as schematically shown in the inset of Fig. 7.16(c). In order to perform the fit, first of all one has to derive a model.

Here we derive a two discrete with one continuum model using section 5 of Ref. [52]. The Hamiltonian is similar to Eq. (4.68) but with two discrete states as

$$\langle \phi_m | \mathscr{H} | \phi_n \rangle = E_n \delta_{mn}, \;\; \langle \psi_{E'} | \mathscr{H} | \psi_E \rangle = E\delta(E' - E), \;\; \langle \psi_E | \mathscr{H} | \phi_n \rangle = V_{En} \tag{7.19}$$

where m and n denotes the label for discrete states, and corresponding eigenstate can be similarly derived using perturbation theory as

$$\Psi'_E = a_1\phi_1 + a_2\phi_2 + \int dE' b(E')\psi_{E'} \tag{7.20}$$

where ϕ_1 and ϕ_2 are the spin-up and spin-down states, respectively. Then the tran-

sition matrix element of initial state $|i\rangle$ to perturbed state $|\Psi'_E\rangle$ is

$$\begin{aligned}\langle\Psi'_E|\hat{T}|i\rangle &= \cos\Delta[\{\sum_\nu \frac{\tan\Delta_\nu}{\pi V^*_{\nu E}}\langle\tilde{\phi}_\nu|\hat{T}|i\rangle + \frac{\tan\Delta_\nu}{\pi V^*_{\nu E}}\mathcal{P}\int dE'\frac{V_{\nu E'}\langle\psi_{E'}|\hat{T}|i\rangle}{E-E'}\} \\ &\quad - \langle\psi_E|\hat{T}|i\rangle] \\ &= \cos\Delta[\sum_\nu \frac{\tan\Delta_\nu}{\pi V^*_{\nu E}}\langle\tilde{\Phi}'_\nu|\hat{T}|i\rangle - \langle\psi_E|\hat{T}|i\rangle] \\ &= \cos\Delta\langle\psi_E|\hat{T}|i\rangle[\sum_\nu q_\nu \tan\Delta_\nu - 1], \end{aligned} \tag{7.21}$$

i.e., the transition matrix element is still the superposition of transition to each discrete state, direct photoemission, and interference between direct PES and each discrete state. The admixture state $\tilde{\Phi}'_\nu$ and phase shift Δ here are given by

$$\tilde{\Phi}'_\nu = \tilde{\phi}_\nu + \mathcal{P}\int dE'\frac{\psi_{E'}V_{E'\nu}}{E-E'} \tag{7.22}$$

$$-\tan\Delta = \sum_\nu \frac{\pi|V_{E\nu}|^2}{E-E_\nu} = -\sum_\nu \tan\Delta_\nu. \tag{7.23}$$

Therefore, the transition probability is given by

$$\frac{|\langle\Psi'_E|\hat{T}|i\rangle|^2}{|\langle\psi_E|\hat{T}|i\rangle|^2} = \frac{1}{1+(\frac{1}{\varepsilon_1}+\frac{1}{\varepsilon_2})^2}\cdot(\frac{q_1}{\varepsilon_1}+\frac{q_2}{\varepsilon_2}+1)^2 \tag{7.24}$$

where the parameters q_ν and ε_ν are defined similarly by

$$q_\nu = \frac{\langle\tilde{\Phi}'|\hat{T}|i\rangle}{\pi V_{E\nu}\langle\psi_E|\hat{T}|i\rangle}, \quad \varepsilon_\nu = -\cot\Delta_\nu \tag{7.25}$$

and we use this function for the fit on Eu^{3+}, the two discrete states may be taken into account.

The results of the fit are shown in Fig. 7.16(c) denoted by solid lines. The overall agreement is good in Eu^{2+} whereas the agreement is poor in Eu^{3+}. This indicates that in Eu^{2+}, the one discrete and one continuum model works well; the unoccupied Eu $4f$ states are relatively well-defined by one discrete state with degeneracy. As for the Eu^{3+}, the poor agreement can especially be seen around $h\nu = 147$ eV; the finite experimental intensity around $h\nu = 147$ eV exists while the fit does not. This indicates that the present model requires more discrete states, probably because the Eu^{3+} does not have the 'well-defined' energy level as Eu^{2+} but has rather energy distribution considering the fact that the enhancement is about 53 times weaker than Eu^{2+} [see the intensity scale in Fig. 7.16(c)]. The cause of the energy distribution only seen in Eu^{3+} could be due to a real-space-dependence of the self-doped amount.

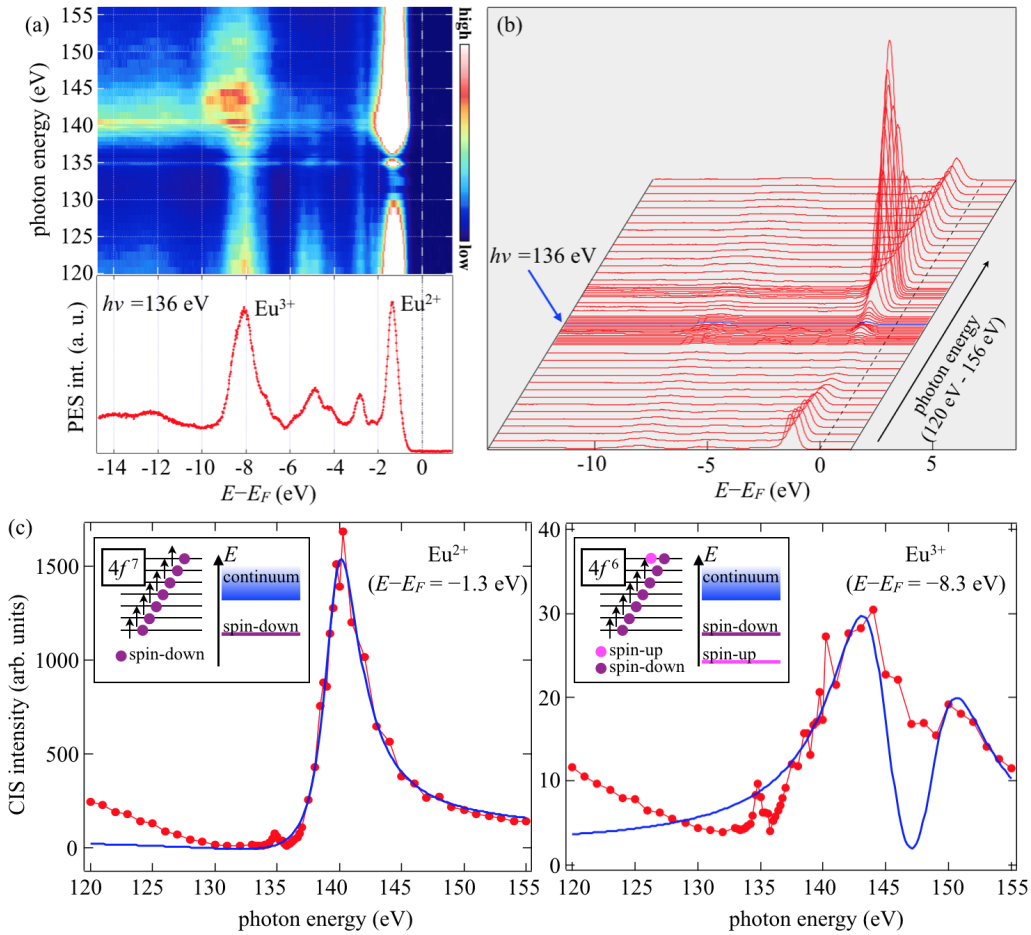

Figure 7.16: (Color online) (a) Eu $4d$-$4f$ resonant photoemission spectral image taken at 50 K from 120 eV up to 156 eV and (b) each PES speactrum of (a). Typical PES spectrum at $h\nu = 136$ eV is also shown in the bottom of (a). (c) CIS plot at $E = -1.3$ eV (Eu^{2+}) and $E = -8.3$ eV (Eu^{3+}) and corresponding Fano profile fit. Inset shows the schematics of the $4f^7$ (Eu^{2+}) and $4f^6$ (Eu^{3+}) states including holes. Light (dark) purple denotes the hole that will have the excited state with $E_0 + J$ ($E_0 + U$) when an electron occupies where E_0 denotes the ground state energy. Schematic energy levels of discrete states and continuum for the each model of Fano profile fit are also shown.

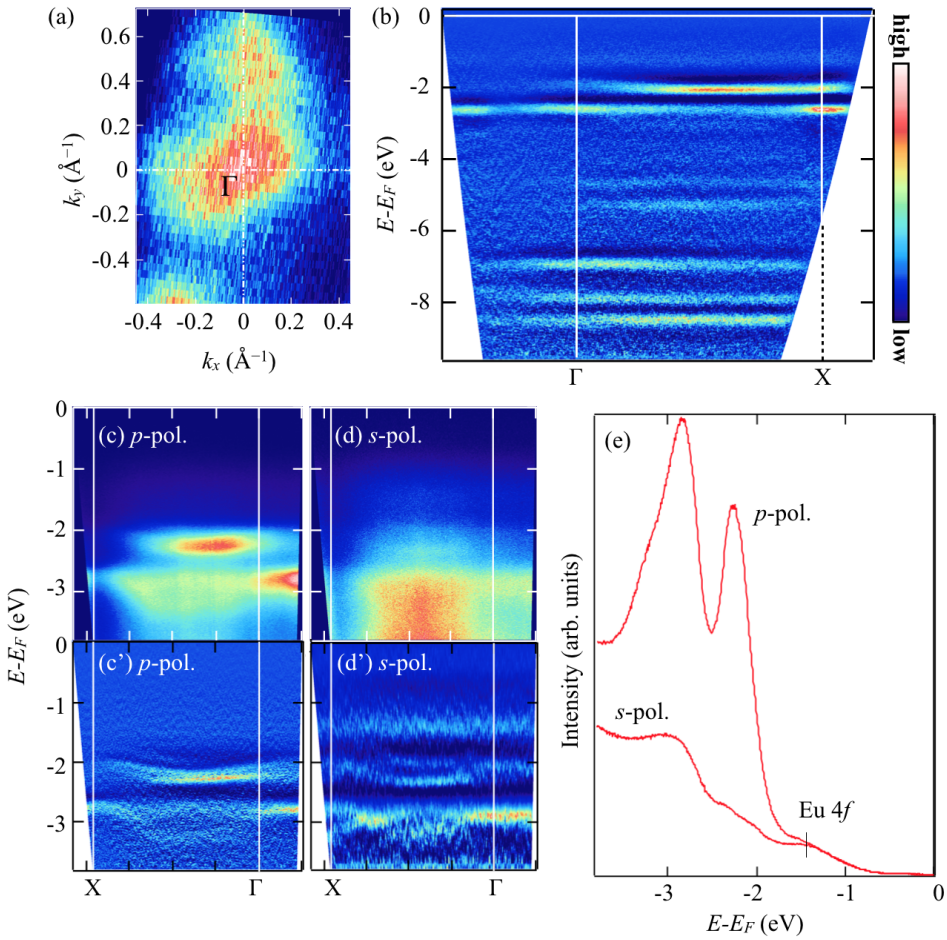

Figure 7.17: (a) Photoemission intensity map taken at $E = -2.0$ eV. (b) Second derivative plot of valence band along Γ-X line. (c) Valence band dispersion along Γ-X near E_F taken with p-polarization setup and (c') its second derivative. (d) and (d') are the same as (c) and (c') but with s-polarization setup. (e) EDCs of (c) and (d).

Moreover, it is confirmed that there is no hybridization between the Eu $4f$ electrons and the conduction band because none of the photoemission spectra from 120 eV to 156 eV has strong enhancement near Fermi level (E_F). In other words, the system is not in valence fluctuating state, but rather in a static mixed valence state. Besides the valence state, all the photoemission spectra show the very weak intensity near E_F.

Angle-resolved photoemission study

In order to examine if the Bi $6p$ orbitals are occupied or not since the angle-integrated PES intensity at E_F was very weak as seen in Fig. 7.16(b), we have performed

angle-resolved photoemission spectroscopy. Figure 7.17(a) is a photoemission intensity map at $E = -2.0$ eV integrated within ± 5 meV. The band dispersion along Γ-X in a wide energy range is shown in Fig. 7.17(b), and band dispersions in a narrow energy range taken with p- and s-polarization are shown in Figs. 7.17(c) and 7.17(d), respectively. Corresponding second derivatives are also shown in Figs. 7.17(c') and 7.17(d'), and EDCs integrated along Γ-X are shown in Fig. 7.17(e). From the band dispersion, it is most likely confirmed that there is no electron band around X point near E_F, indicating that the electrons coming from Eu^{3+} are trapped somewhere and/or disturbed or smeared out by a strong atomic disorder [119–121]. However, there is still a possibility that the system has a sort of electronic phase separation and/or distribution of self-doped electron due to the strong atomic disorder, which is higher than other RE(O,F)BiS$_2$ members [122].

Space-resolved photoemission study

In order to reveal the detailed space-resolved information and confirm whether the Bi $6p_{x/y}$ orbitals exist or not in the space-resolved electronic structure, we have performed space-resolved photoemission spectroscopy. Besides, in the present system, our Eu L_3-edge XAS results, a bulk sensitive valence probe, revealed Eu to be in mixed valence state and hence a self-doping mechanism can be a plausible scenario to describe the properties of this material, as well as proposed by Mössbauer study [92]. Considering the current state and open issues it is a reasonable approach to use space-resolved ARPES to explore any possible chemical/electronic segregations and to study the intrinsic electronic structure.

Space-resolved photoemission intensity map integrated within -3.5 eV $\leq E \leq 0.15$ eV is shown in Fig. 7.18(a). The image covers the whole sample, and the spatial resolution is 15×15 μm^2 per pixel. Figure 7.18(b) is the same as Fig. 7.18(a) but integrated within -0.5 eV $\leq E \leq 0.15$ eV, which should cover the electron-like band originated by Bi $6p_{x/y}$. One can see a much clear contrast in Fig. 7.18(b) than Fig. 7.18(a), indicating that the present EuFBiS$_2$ system shows a electronic phase separation in mesoscopic scale. Figures 7.18(c) and 7.18(d) are the expanded view of the squared region in Figs. 7.18(a) and 7.18(b) with a 3×3 μm^2 per pixel resolution. Again, one can see the clear contrast with a higher spatial resolution.

Figure 7.18(e) shows angle-integrated spectra in the bright and dark regions in Fig. 7.18(d). The spectrum of the bright region shows strong intensity near E_F while that of the dark region has very weak intensity. Even though the structures of Eu $4f$ and S1 $3p_z$ are almost the same, there is a considerable difference in the S1 $3p_{x/y}$ feature [see Fig. 7.18(f) for the definition of S1 and S2 in EuFBiS$_2$].

In order to see how the structures of Bi $6p_{x/y}$ and S1 $3p_{x/y}$ changes from the bright to dark region, we have performed sequent scan from the bright to dark re-

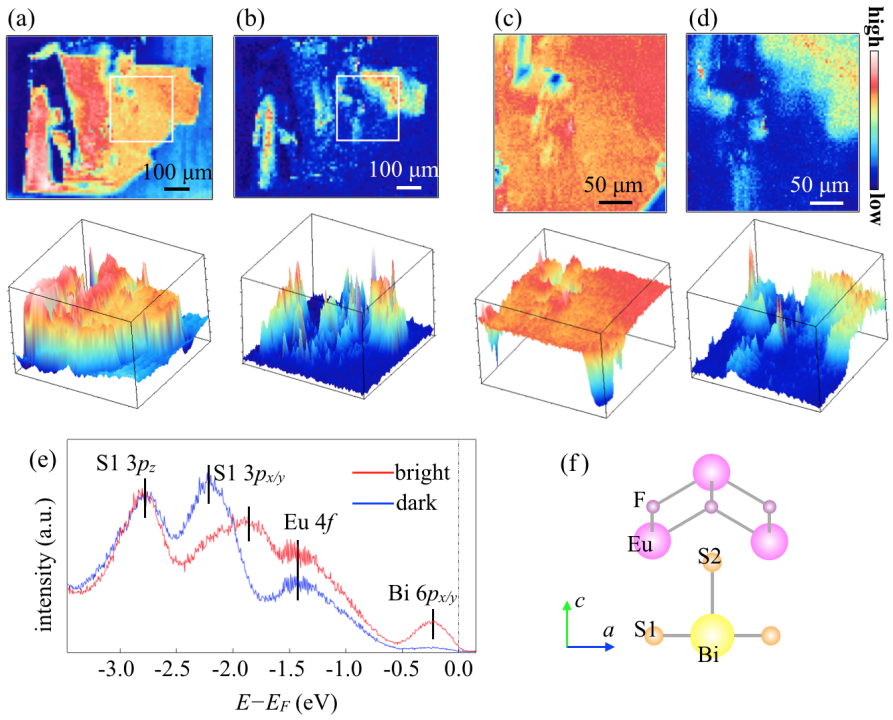

Figure 7.18: Real-space photoemission intensity map of the whole EuFBiS$_2$ sample integrated within (a) -3.5 eV $\leq E \leq 0.15$ eV and (b) -0.5 eV $\leq E \leq 0.15$ eV with a space resolution of 15×15 μm^2 per pixel. (c) and (d) are the expansion of the squared region in (a) and (b) but with a 3×3 μm^2 per pixel resolution. The 3D images of (a) - (d) are shown below as well. (e) Representative photoemission spectra of bright and dark region in (d). (f) Local structure of EuFBiS$_2$, and the definition of S1 (in-plane S) and S2 (apical S),

gions as denoted by A to F in Fig. 7.19(a), which is the same as Figs. 7.18(c) and 7.18(d) but with the notations for the sequent scan. The sequent PES spectra taken from A to F are shown in Fig. 7.18(b). One can see that the energy positions of both Bi $6p_{x/y}$ and S1 $3p_{x/y}$ continuously change from bright to dark region. This indicates that the Bi $6p_{x/y}$ and S1 $3p_{x/y}$ have some correlation and/or hybridization, and the local structure may also continuously changes from A to F region. Besides the energy position, the spectral weight of Bi $6p_{x/y}$ also gradually decreases when the scan goes from A to F as shown in 7.19(d).

In order to confirm whether the metallic phase has the electron-like band around X point as often seen in a typical BiS$_2$-based systems, we have performed angle-resolved photoemission experiment on both metallic and insulating phases, A and F regions of Fig. 7.19(a). Figure 7.20(a) shows the Fermi surface mapping in A, and corresponding band dispersion along X-M is shown in Fig. 7.20(b). One

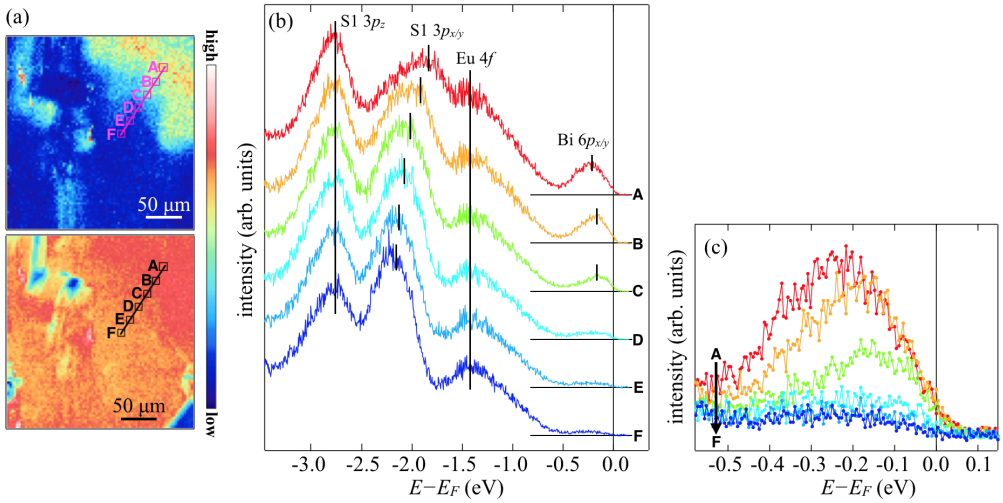

Figure 7.19: (a) is the repost of Figs. 7.18(c) and 7.18(d) but with notations where the PES spectra were taken. (b) Space-dependent photoemission spectra, and corresponding spaces are denoted from A to F in (a). (c) The expanded view of Bi $6p_{x/y}$ structures of A - F in (a).

can see a clear Fermi surface around X point, which is typical for the BiS$_2$-based systems. As for the insulating phase in F region, the Fermi surface can hardly be seen as displayed in Fig. 7.20(c). However, as for the band dispersion shown in Fig. 7.20(d), one can see a weak intensity around X point near E_F. Comparing the band dispersion with metallic phase besides the spectral weight of Bi $6p_{x/y}$ bands, one of the most outstanding differences is the band width of S1 $3p_{x/y}$ orbitals. In the metallic phase with a clear electron band by Bi $6p_{x/y}$ around X point, the S1 $3p_{x/y}$ shows wider band widths whereas in the insulating phase with a weak Bi $6p_{x/y}$ contribution, the S1 $3p_{x/y}$ shows narrower band widths.

Finally , we speculate the mechanism of the phase separation observed by space-resolve PES so far. We apply the similar speculation of Ce(O,F)BiS$_2$ system to the present EuFBiS$_2$ system as follows. When the system is in a metallic phase, BiS plane is decoupled from S2 and block layer, resulting in a stabilized BiS conducting plane. As for the insulating phase, the S2 atoms and block layer are coupled with BiS plane, and self-doped electron could be trapped in the middle of the Eu-S2-Bi exchange pathway. Considering the fact that S2 is almost fully occupied, the possible orbital is unoccupied Bi $6p_z$. Schematic diagrams of this speculation is shown in Fig. 7.21.

The strong atomic disorder observed in various BiS$_2$ systems [100, 123] may be able to trap the electrons in the Bi $6p_z$ in other BiS$_2$-based materials as well. Moreover, recent finding of the superconductivity in CeOBiS$_2$ [124] can be explained by this scenario.

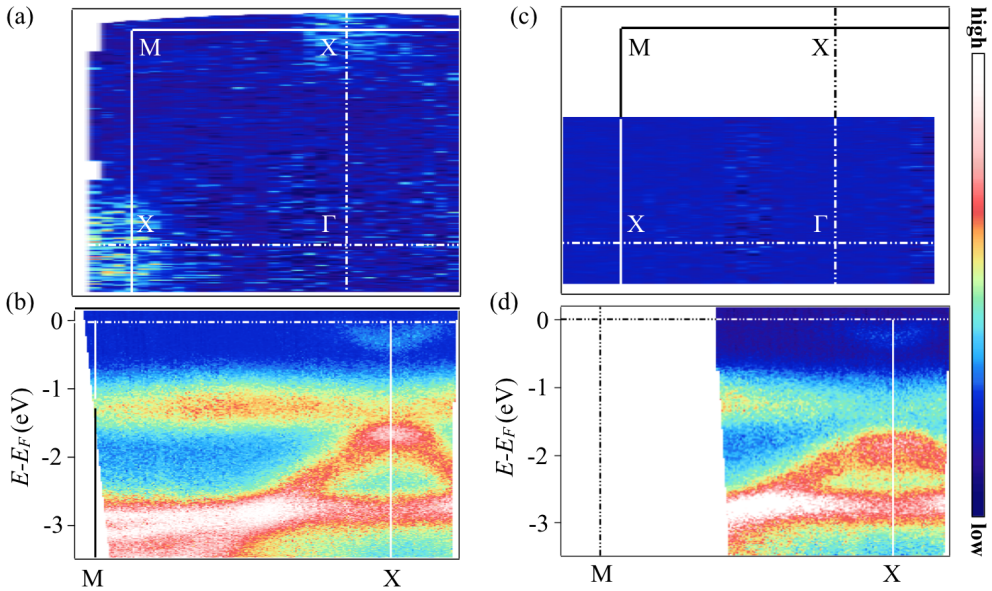

Figure 7.20: (a) Fermi surface taken at A region in Fig. 7.19(a) and (b) corresponding band dispersion taken along X-M line. (c) Fermi surface taken at F region in Fig. 7.19(a) and (d) corresponding band dispersion taken along X-M line.

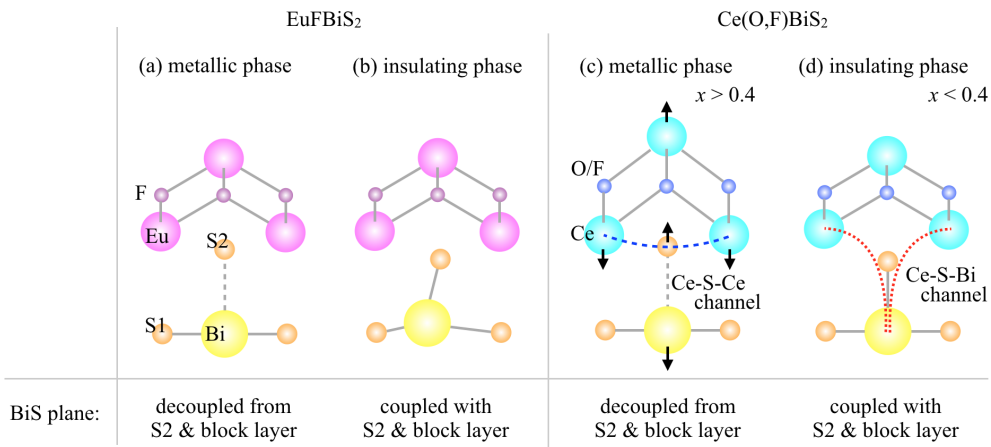

Figure 7.21: Schematic diagram of the possible local structures (a) in metallic and (b) in insulating phase of $EuFBiS_2$ system. The local structures of (c) metallic and (d) insulating $Ce(O,F)BiS_2$ are reposted as a reference.

7.4.3 Conclusion

In summary, we have investigated the electronic structure of EuFBiS$_2$ by means of Eu L_3-edge XAS, Eu $4d$-$4f$ resonant PES, ARPES, and space-resolved PES. The XAS revealed that Eu is in the mixed valence state with coexistence of Eu^{2+} and Eu^{3+}, indicating part of electron in Eu is doped in the BiS plane. Using the Eu $4d$-$4f$ resonant PES, we have identified the partial DOS of Eu^{2+} and Eu^{3+} states. From the ARPES study, there is no electron-like band around X point near Fermi level, which is expected to appear due to the possible self-doped mechanism by Eu. It is possible that the electron-like band is smeared out by the local atomic disorder, which is especially strong in the present system compared with other BiS$_2$-based materials. In order to confirm whether the system has some chemical segregation or phase separation, we performed space-resolved photoemission experiment. Surprisingly the system showed a mesoscopic electronic phase separation; metallic and insulating phases. The similar speculation of Ce(O,F)BiS$_2$ system was applied for the local environment of the system; in the metallic phase the BiS plane is decoupled with S2 atoms and block layer while in the insulating phase BiS is coupled with block layer though the S2 atoms, and the self-doped electrons are trapped in Bi $6p_z$ orbital due to strong atomic disorder.

7.5 Orbital states of CeO$_{0.5}$F$_{0.5}$BiS$_2$ revealed by polarization-dependent ARPES

We have investigated the electronic structure of BiS$_2$-based CeO$_{0.5}$F$_{0.5}$BiS$_2$ superconductor using polarization-dependent angle-resolved photoemission spectroscopy (ARPES), and succeeded in elucidating the orbital characters on the Fermi surfaces. In the rectangular Fermi pockets around X point, the straight portion parallel to the k_y direction is dominated by Bi $6p_x$ character. The orbital polarization indicates the underlying quasi-one-dimensional electronic structure of the BiS$_2$ system. Moreover, distortions on tetragonally aligned Bi could give rise to the band Jahn-Teller effect.

7.5.1 Experimental condition

A high-quality single crystal of CeO$_{0.5}$F$_{0.5}$BiS$_2$ with $c = 13.443$ Åhas been prepared by CsCl flux method provided by Aoki group , Tokyo Metropolitan University, and its details are given elsewhere [93]. The polarization-dependent ARPES measurements with linearly/circularly polarized photons have been performed at the undulator beamlines BL-1/BL-9A of the Hiroshima Synchrotron Radiation Center, Hiroshima University. The photon energy was set to be 30 eV for all the polarizations. We cleaved the single crystalline sample *in situ* in ultrahigh vacuum

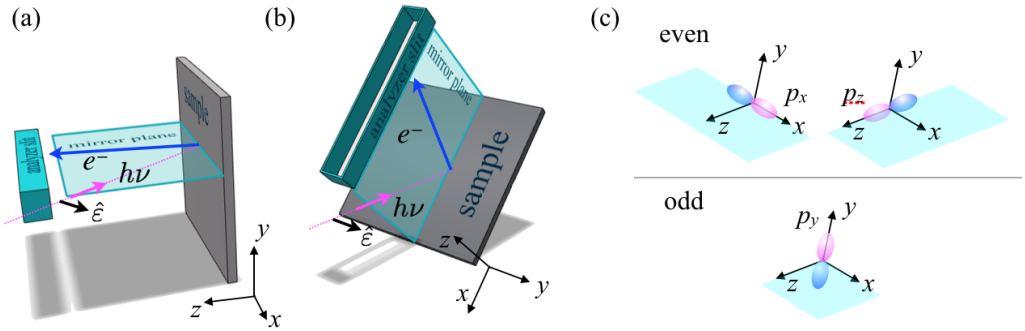

Figure 7.22: Schematic diagram of the measurement geometries with linearly polarized photons that give us (a) p-polarization and (b) s-polarization. The polarization vector of photons are denoted by ε. (c) The p orbitals with even and odd symmetries with respect to the mirror plane.

($\leq 1 \times 10^{10}$ Torr) in order to obtain a clean (001) surface. The total energy resolution including both monochromator and electron energy analyzer was measured to be 21 meV. All the measurements were taken at 50 K. The experimental p- and s-polarization setups at BL-1 are shown in Fig. 7.22. When changing the polarization, the main chamber including the sample and the analyzer rotates with respect to the light axis. In the case of $CeO_{0.5}F_{0.5}BiS_2$, the p_x and p_z orbitals are observable for the p-polarization setup, while the p_y orbital is observable for the s-polarization setup. Unlike the linear polarization at BL-1, the dipole selection rule does not hold for circularly polarized photons at BL-9A giving nonzero transition matrix element for all the orbitals.

7.5.2 Results and discussion

Fermi surfaces and electron concentration estimated by Luttinger volume

The Fermi surface map of $CeO_{0.5}F_{0.5}BiS_2$ was taken by changing the tilt angle with circularly polarized light as shown in Fig. 7.23(a), whereas that with the p-polarized light was taken by changing the azimuthal angle as shown in Fig. 7.23(b). Intensities of the Fermi surface maps were integrated within ± 40 meV above and below E_F. In the rectangular Fermi pockets with p-polarized light [Fig. 7.23(b)], the straight portion parallel to the k_y direction is much more enhanced than that parallel to the k_x direction. This observation may indicate that the straight portion parallel to the k_y direction is derived from Bi $6p_x$ and that the other straight portion parallel to the k_x direction has more Bi $6p_y$ character. However, since the Fermi surface was measured by changing the azimuthal angle, the orbital selectivity is not exact for the straight portion parallel to thek_x direction. Figures 7.23(c) - 7.23(d) show detailed

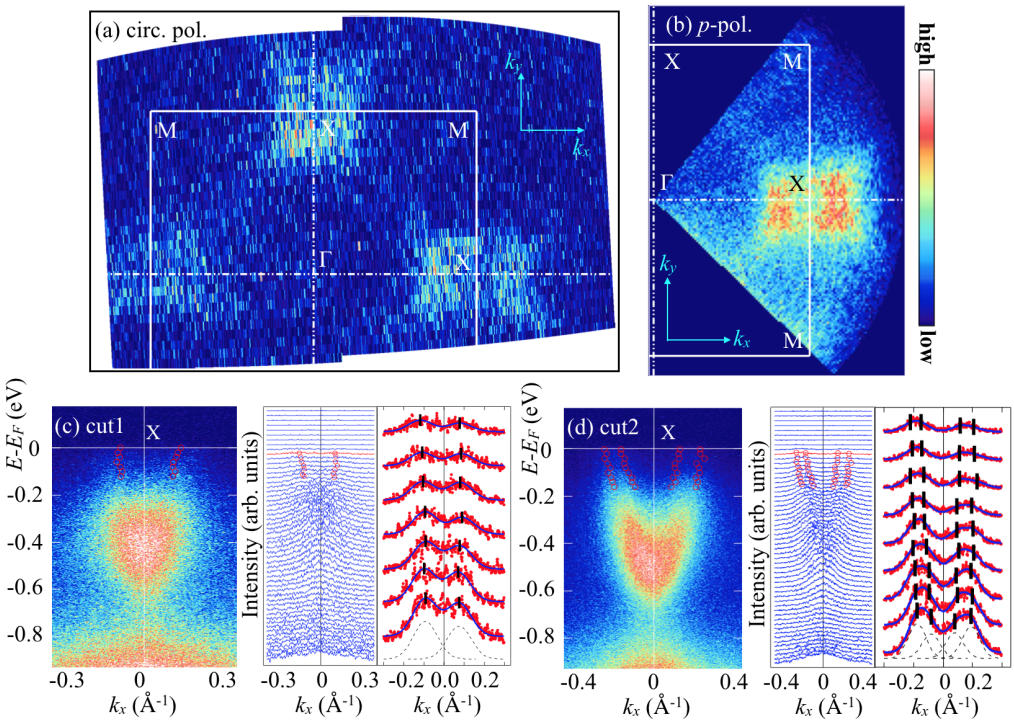

[t]

Figure 7.23: (a) Fermi surface maps of $CeO_{0.5}F_{0.5}BiS_2$ taken with circularly polarized light and (b) with p-polarization geometry, integrated within ± 40 meV. (c) Cut denoted by cut 1 in (a), MDCs, and fit on MDCs from $E = -0.12$ eV up to E_F for the extraction of peak positions. (d) Cut denoted by cut2 in (a), MDCs, and fit on MDCs from $E = -0.16$ eV up to E_F for the extraction of peak positions. Gaussian functions giving the best fit to the bottommost MDCs are also displayed in (c) and (d).

analyses on the electronic states forming the Fermi surfaces around X point. Figures 7.23(c) and 7.23(d) show the band dispersion of cut1 and cut2 denoted in Fig. 7.23(a), and corresponding momentum distribution curves (MDCs) are displayed as well. In order to estimate the peak positions, multi-peak fit using two or four Gaussian functions has been done, and the results are shown in Figs. 7.23(c) and (d) (in the present system with strong atomic disorder [100], the MDC width may have rather Gaussian character). The Gaussian functions giving the best fit to the bottommost MDCs are displayed in the figures. The peak positions identified by this fit are denoted by circles and by vertical bars in Figs. 7.23(c), 7.23(d). The results clearly indicate that there exist two electron-like Fermi surfaces around X point. Full-width-half-maximum was fixed for all the fits. The Fermi wave numbers are estimated as $k_{F1} \sim 0.1$Å^{-1}, $k_{F2} \sim 0.12$Å^{-1}, and $k_{F3} \sim 0.22$Å^{-1}. These labels are indicated in the Figs. 2(e) and 2(h). Identifying the Fermi wave numbers

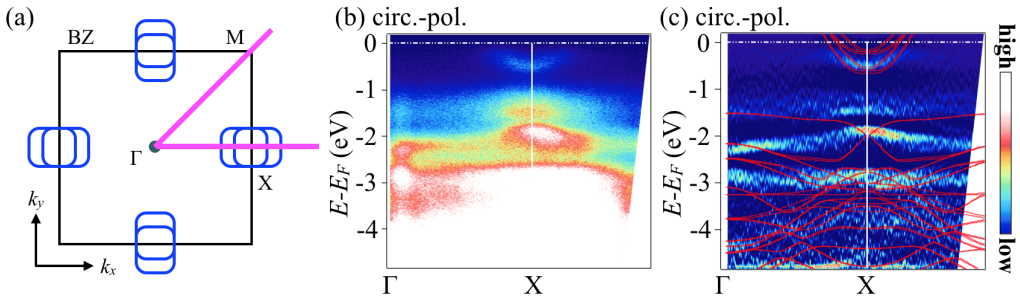

Figure 7.24: (a) Schematic diagram of the Fermi surfaces, and the ARPES data was taken along the solid lines. ARPES spectra of (a) Raw data and (b) EDC curvature with circularly polarized photons.

enables us to estimate the approximate amount of electron in the system; the inner and outer electron pockets respectively enclose 3.9% and 7.2% of the Brillouin zone. Counting the Luttinger volume of the Fermi surfaces as

$$n = 2\int_{G(\omega=0,k)>0} \frac{d^D k}{(2\pi)^D} = 0.22, \tag{7.26}$$

i.e., we estimate the amount of electron to be 0.22 electron per Bi in $CeO_{0.5}F_{0.5}BiS_2$, that is much smaller than the nominal value. Moreover, the topology of the Fermi surface at x ∼0.5 predicted by LDA calculation is different from our results, and likely to be closer to the Fermi surface at x ∼0.25.

Here, reminding us of the length of the c-axis as 13.443 Åand comparing this value with Tab. 7.1, one can roughly estimate that actual F concentration can be more than 0.16 but less than 0.24 since the c-axis is widely used as a correlated parameter of F concentration. Therefore, we conclude that there is no difference between doped F and effective carrier concentration in the $CeO_{0.5}F_{0.5}BiS_2$ system. If the actual F amount is higher than 0.22 (over the error bars), Bi defects on BiS plane can trap some electrons reported by scanning tunneling microscopy study [125], yet further investigations are needed for the precise F characterization.

polarization-dependent band dispersions

Figure 7.24(a) shows the schematic Fermi surface, and we measured ARPES data along M-Γ-X line as depicted by the bold line. Raw data and EDC curvatures of the valence band (here, EDC stands for energy distribution curve) taken with circularly polarized photons are shown in Figs. 7.24(b) and 7.24(c), respectively. Figures 7.25(a) - 7.25(c) and 7.25(d) - 7.25(f) show the band dispersions along M-Γ-X taken with p- and s-polarization setup, respectively. Raw data are displayed in Figs. 7.25(a) and 7.25(d), corresponding EDC curvatures are shown in Figs. 7.25(b)

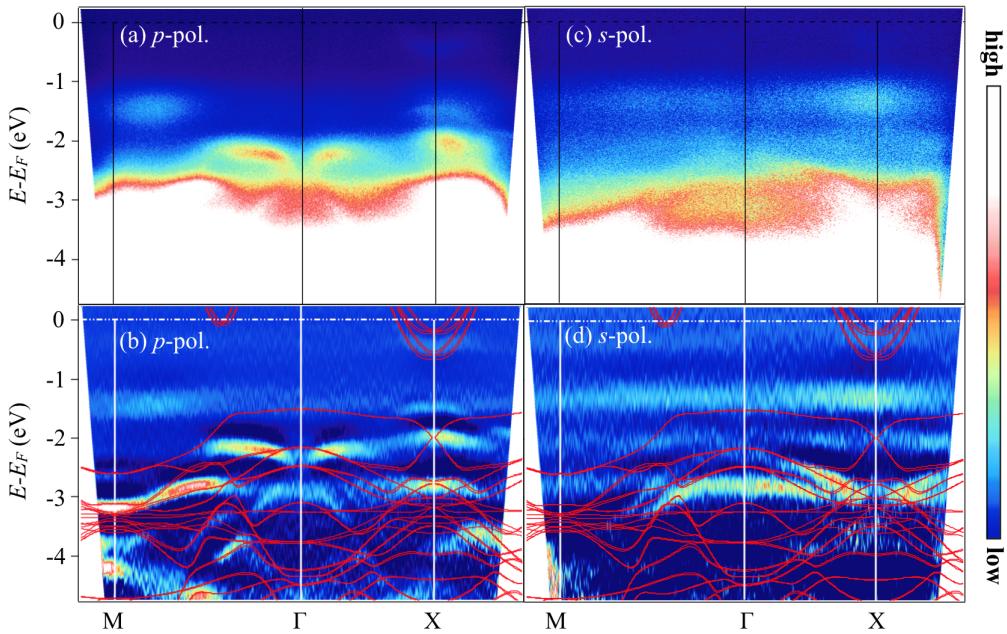

Figure 7.25: Polarization dependence of the band dispersions of $CeO_{0.5}F_{0.5}BiS_2$. (a) Raw data, (b) EDC curvature, and (c) EDCs along M-Γ-X with p-polarized light. (d) Raw data, (e) EDC curvature, and (f) EDCs along M-Γ-X with s-polarized light. The ab initio calculation for the $CeO_{0.5}F_{0.5}BiS_2$ system is overlaid on each curvature as well.

and 7.25(e), EDCs are in Figs. 7.25(c) and 7.25(f). The *ab initio* calculation is overlaid on each curvature plots. One can see a flat band located about $E = -1.4$ eV (between Bi $6p$ conduction band and valence bands) due to localized Ce $4f$ electrons for both polarizations in Figs. 7.24(d) and 7.24(g) as discussed in the chapter of Ce $4d$-$4f$ resonance experiment on Ce(O,F)BiS$_2$.

Comparing the band dispersion taken with s- and p-polarizations, spectral features are clearly observed with p-polarization whereas they are hardly seen with s-polarization as shown in Figs. 7.26(a) and 7.26(b). The EDCs integrated within $k_x = \pm 0.4$ Å^{-1} along Γ-X direction are also displayed in Fig. 7.26(c), and one can see that the spectral weights of p- and s-polarizations are drastically changed. Considering that the cuts along Γ-X were taken in the direction of k_x, the results suggest us that the electron-like band near X point in the k_x direction (*i.e.*, the Fermi surface is parallel to the k_y direction) is dominantly derived from Bi $6p_x$ orbital. In other words, the system has quasi-one-dimensional property in at least Γ-X cut.

Here, there are two possibilities that have quasi-one-dimensional Fermi surfaces in high symmetry lines; one is that the Fermi surfaces consist of p_x pockets and p_y pockets in the k_x and k_y direction, respectively (scenario A), and the other is that

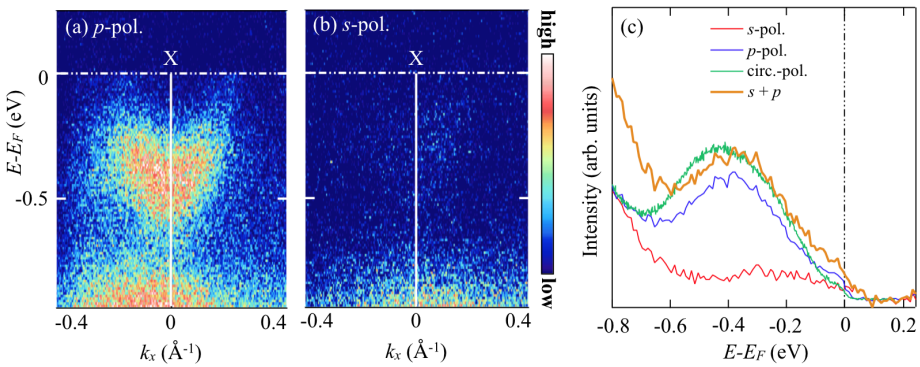

Figure 7.26: Detailed electronlike band of $CeO_{0.5}F_{0.5}BiS_2$ around X point in the k_x direction with (a) p-polarization and (b) s-polarization. (c) Comparison of EDCs of the electronlike band around X with p-, s-, circular, and the sum of s and p polarization integrated in the range of $k_x = \pm 0.4$Å^{-1} in the k_x direction.

Fermi surfaces parallel to the k_x (k_y) direction are dominated by p_x (p_y) orbital (scenario B). In the former case, pockets can be interpreted as a inter-chain hopping of Bi sites whereas in the latter case it can be due to strong orbital polarization (orbitals are polarized in the entire Brillouin zone). These two scenarios are schematically described in Fig. 7.27.

One can exclude the possibility of scenario B by comparing the ARPES intensity of the bottom of the electron-like band ($E = -0.4$ eV) around X point. If scenario B is correct, then stronger intensity at the band bottom than that near E_F should appear using s-polarization setup since this part consists of both p_x and p_y under the assumption of scenario B. However, in Fig. 7.26, there is no feature around the bottom of the electron-like band, which contradicts the scenario B but is consistent with scenario A.

Comparison with theoretical studies

According to the minimal model calculation by Usui, Suzuki, and Kuroki [84], the band along Γ-X consists of well-hybridized Bi p_X and p_Y (namely, close to pure Bi p_x or Bi p_x) whereas that along Γ-M is derived from pure Bi p_X or p_Y as in Figs. 7.28(a) and 7.28(b). Here, the X- and Y-axes can be obtained by rotating the x- and y-axes by 45 degrees with respect to z-axis. Fig. 7.28(c) shows the proposed orbital distribution and schematic Fermi surfaces. The basis can be transformed by their linear combinations as

$$|p_X\rangle = \frac{1}{\sqrt{2}}\{|p_x\rangle + |p_y\rangle\},\ |p_Y\rangle = \frac{1}{\sqrt{2}}\{|p_x\rangle - |p_y\rangle\}. \tag{7.27}$$

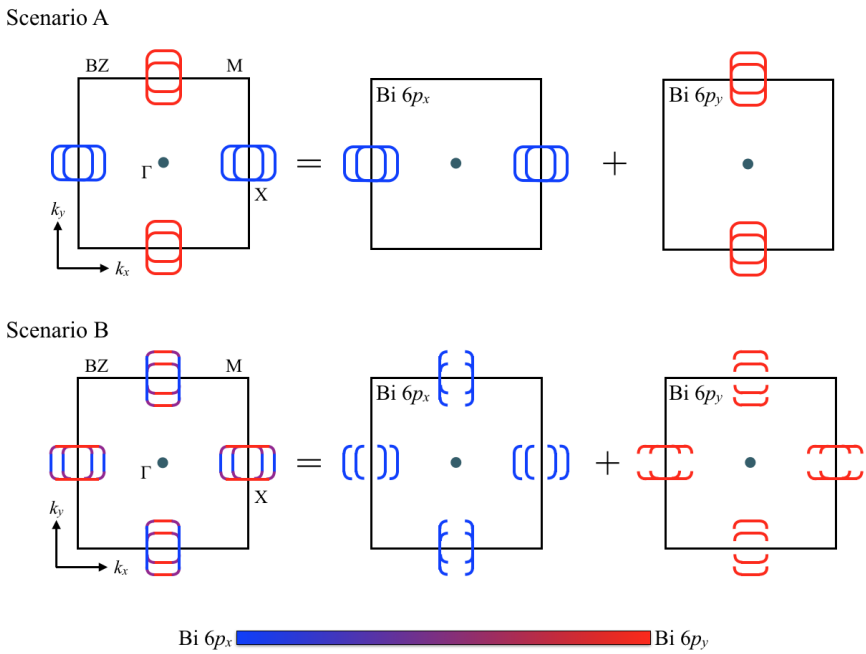

Figure 7.27: Possible scenarios for the orbitally-polarized Fermi surfaces; scenario A describes that the Fermi surfaces consist of p_x pockets and p_y pockets in the k_x and k_y direction, respectively, whereas scenario B speculates that Fermi surfaces parallel to the k_x (k_y) direction are dominated by p_x (p_y) orbital.

At the doping level of $x = 0.5$, the band along Γ-M crosses E_F and forms almost strait Fermi surfaces with p_X (or p_Y) character. Usui, Suzuki, and Kuroki proposed the Fermi surface nesting between the p_X Fermi surfaces or between the p_Y Fermi surfaces can enhance the spin fluctuations for the superconductivity [84]. On the other hand, at the doping level of x = 0.25, the band along Γ-M does not cross E_F and only the band along the Γ-X forms Fermi pockets (disconnected Fermi surfaces) around X point with almost pure p_x or p_y character. In this sense, our results are partly consistent with the previous calculation for x=0.25. Considering the fact that the observed Fermi surfaces of the superconducting samples are similar to those predicted for x=0.25, the mechanism of the superconductivity should be discussed based on the disconnected Fermi surfaces.

As for the orbital states of the Fermi surface, calculated results in the underdoped region by Usui, Suzuki, and Kuroki [126] are shown in Fig. 7.28(c) where the doping level is denoted by n and the colored parts are dominated by Bi $6p_x$ orbital. This is consistent with our scenario A in Fig. 7.27.

With these theoretical supports, we would conclude the detailed orbital characterization; in the rectangular Fermi surface around $(\pi, 0)$, the straight portion parallel to the k_y-axis is dominated by Bi $6p_x$ as schematically shown in Fig. 7.29(a).

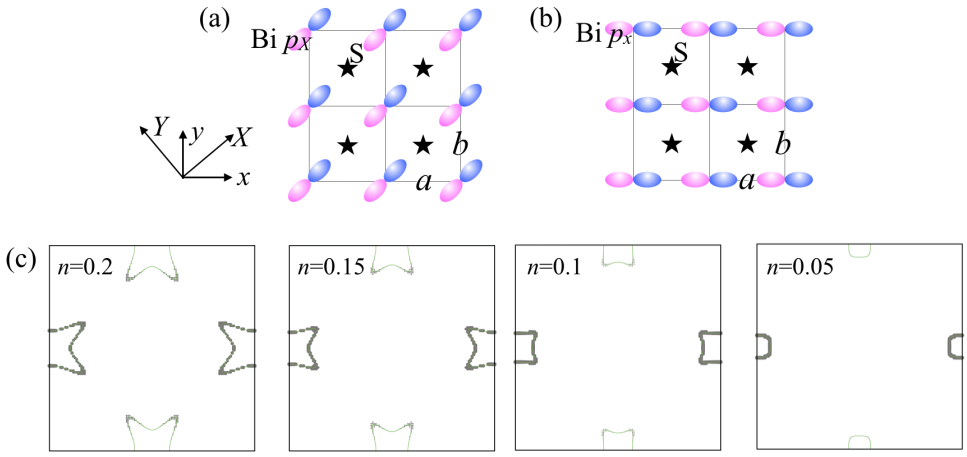

Figure 7.28: Schematic diagrams of the orbital polarization in real space along Γ-M predicted by Usui, Suzuki, and Kuroki [84] and (b) observed orbital polarization along Γ-X. They can be transformed back and forth each other by their linear combination. (c) A schematic diagram of the orbital distribution at underdoped region proposed by Usui, Suzuki, and Kuroki [126] with various doping level (n). Colored region denotes the Bi $6p_x$ components.

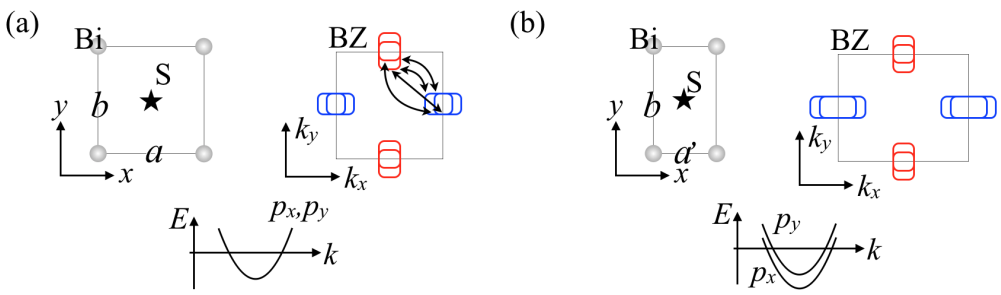

Figure 7.29: (a) Schematic diagrams of the Fermi surface and corresponding band dispersion of Bi $6p_x$/$6p_y$. Nesting vectors are also shown here. (b) Schematic diagrams of orthorhombically distorted Bi sites with $a' < a$, Fermi surface, and band Jahn-Teller effect on Bi $6p_x$/$6p_y$.

On the other hand, the straight portion parallel to the k_x-axis has more Bi $6p_y$ character as suggested by the Fermi surface map in Fig. 7.23(b) although the orbital selectivity is not exact in this region. The rectangular Fermi pockets around X point keeps a peculiar quasi-one-dimensionality due to the orbital polarization. This situation is partly similar to the quasi-one-dimensional Fermi surfaces with the orbital polarization for $x = 0.5$ [84]. However, as indicated by the arrows in Fig. 7.29(a), possible nesting channels between the straight portions of the rectangular Fermi pockets may have different orbital character, indicating spin and orbital fluctuations. In addition, the Fermi surface nesting may enhance the electron-lattice interaction. The electron-electron interaction (spin and orbital fluctuations) and the electron-lattice interaction would be one of the reasons that the band dispersions obtained by ARPES showed poor agreements with the *ab initio* calculation. Interestingly, the orbitally-polarized rectangular Fermi surfaces can give the system a possibility of band Jahn-Teller effect. If the Bi lattice is distorted from tetragonal to orthorhombic, for example, the degeneracy of Bi p_x/p_y will be split as schematically depicted in Figs. 7.29(a) and 4(b) (where $a' < a$), resulting in the distorted Fermi surface with C_2 symmetry. As a result of the band Jahn-Teller effect, the system has a better nesting condition than the tetragonal symmetry, which further enhances the one-dimensionality. The one dimensional Fermi surfaces may provide Peierls instability to the system. The combination of band Jahn-Teller distortion and Peierls instability would be responsible for the monoclinic distortion under high pressure.

Tight-binding analysis

Even though the shape of the Fermi surfaces predicted by the minimal model calculation are close to observed one, there is no inner Fermi surface by the calculation in the under-doped region [84]. According to the previous study, both bi-layer coupling and spin-orbit interaction can resolve the degenerate Bi $6p_x$ orbitals of upper and lower layer [89]. We extend the same minimal two-orbital model to the bilayer four-orbital model with the Hamiltonian of Eq. (7.1), performed the tight-binding calculation, and compare the results with the Fermi surfaces observed by ARPES.

First of all, we have confirmed that the results produced by Usui *et al.* were perfectly reproducible when the bilayer coupling (BLC) nor spin-orbit coupling (SOC) is not taken into account as shown in the upper panel of Fig. 7.30. When the BLC is taken into account, the degeneracy of Bi $6p_x$ orbitals were resolved in the Γ-X direction while the degeneracy was kept in X-M direction, resulting in the outer and inner Fermi surfaces as shown in the lower panel of Fig. 7.30.

7.5.3 Conclusion

In summary, we have studied the electronic structure of $CeO_{0.5}F_{0.5}BiS_2$ by means of polarization dependent ARPES. From the circularly polarized photon, the doped

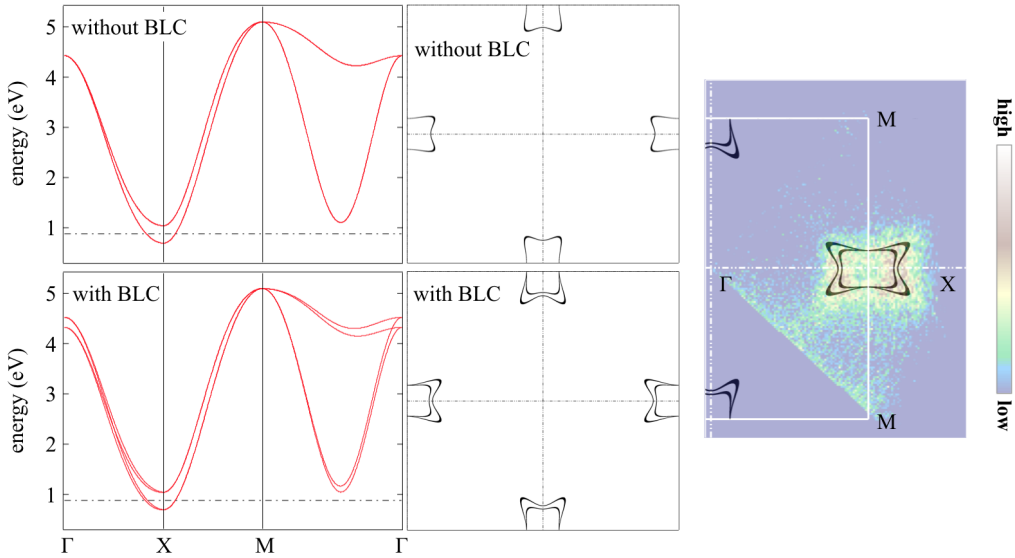

Figure 7.30: The band dispersions and Fermi surfaces of bilayer four-orbital model using tight-binding approximation. When the BLC is not taken into account, the model is reduced into the minimal two-orbital model proposed by Usui, Suzuki, and Kuroki [84] as shown in the upper panels. All the values of the parameters were used as the same with them. The results with the BLC is shown in the lower panel, and the experimental Fermi surfaces are semi-transparently underlaid on the calculated Fermi surfaces in the right.

electron has been estimated using Fermi surface as 0.22 electron per Bi in $CeO_{0.5}F_{0.5}BiS_2$, that is much smaller than the nominal value of 0.5 while from the value of c-axis the F concentration and effective carrier concentration could be the same. From the linearly polarized photons, we have succeeded in the observation of orbitally polarized Fermi surface. It indicates that the system has quasi-one-dimensional property, that could enhance the electronic correlation and/or electron-phonon coupling. This might be why the band dispersion obtained by ARPES has poor agreements with the *ab initio* calculation.

8

CONCLUDING REMARKS

In this chapter, results of the Fe-based and BiS_2-based superconductors are summarized so far. General role of the orbital instability to those layered chalcogenide superconductors is also discussed.

We have identify the orbital states and character of $FeSe_{0.4}Te_{0.6}$ and BiS_2-based materials so far as well as their electronic structures in detail.

As for the $FeSe_{0.4}Te_{0.6}$ system, we invesitigated the system using laser-ARPES, first-principles, and unrestricted HF calculation. The laser-ARPES sucessfully resolved the yz/zx orbital degeneracy at Γ point, and found that xy orbital is hybridized with yz orbital near Γ, resulting in a butterfly-like Fermi surface. Using the first-principles band structure calculation, the xy/yz hybridization is most likely due to the spin-orbit interaction. Moreover, the band dependent renormalization was realized; xy orbital has strong renormalization. After multiplying the renormalization factor and shifting the energy, the xy orbital still has a larget disagreement among t_{2g} orbitals, especially near the Γ point where the electron-like band is hybridized. This can be due to another possible scattering with yz orbitals, which may cause the yz/zx orbital degeneracy at Γ point under the spin-orbit interactive environment. Another interesting finding was the different renormalization strength between yz and zx orbitals even in a tetragonal symmetry. Different strength of renormalization indicates that there may exist a nematic tendency, namely, the yz/zx orbital instability. Strongly renormalized xy orbital and yz/zx orbital instability may play important role for the superconductivity.

Unrestricted HF study using multi-orbital d-p type Hamiltonian revealed that the system has the Kugel-Khomskii tendency with AFM and ferro-orbital metal-insulator transition. However, the present mean-field treatment ignores the fluctuation term, which may play important role.

As for the BiS_2-based systems, we have investigated the mixed valence Ce(O,F)BiS_2 and $EuFBiS_2$ systems. The Ce mixed valence was confirmed by Ce L_3-edge XAS, appears when there is no F-doping, and it gradually disappears when the F-doping takes place. The valence state of the Ce seems rather static since there was no considerable enhancement at Fermi level when the Ce $4d$-$4f$ resonant PES was performed. Combining the information of continuum resonance which is related to the Ce-Bi bondlength, we speculate that Ce-S2-Bi exchange pathway may impede both FM and SC states. When the F is doped to the system. local structure accordingly changes and as a result, new exchange pathway of Ce-S2-Ce will be effective rather than Ce-S2-Bi exchange pathway. The extra electrons coming from Ce can be trapped somewhere in the middle of the Ce-S2-Bi exchange pathway. Considering the fact that the orbitals of S are fully occupied and the Ce already ejected electrons, the only possible orbital is the unoccupied Bi $6p_z$. The possibility of this scenario was further confirmed by Anderson's impurity model analysis.

Another mixed valent candidate $EuFBiS_2$ showed some similarity. The Eu L_3-edge XAS revealed that Eu is in the mixed valence state with coexistence of Eu^{2+} and Eu^{3+}, indicating part of electron in Eu is doped in the BiS plane. Using the Eu $4d$-$4f$ resonant PES, we have identified the partial DOS of Eu^{2+} and Eu^{3+} states. From the ARPES study, there is no electron-like band around X point near Fermi

level, which is expected to appear due to the possible self-doped mechanism by Eu. However, we have detect a possible band splitting in in-plane S1 $3p_{x/y}$ bands. In order to confirm the cause of this split, we performed space-resolved photoemission experiment. Surprisingly the sytem showed a mesoscopic electronic phase separation; metallic and insulating phases. The similar speculation of Ce(O,F)BiS_2 system was applied for the local environment of the system; in the metallic phase the BiS plane is decoupled with S2 atoms and block layer while in the insulating phase BiS is coupled with block layer though the S2 atoms, and the self-doped electrons are trapped in Bi $6p_z$ orbital due to strong atomic disorder.

The Fermi surfaces of the $CeO_{0.5}F_{0.5}BiS_2$ were orbitally polarized. It is known that the sytem shows higher superconducting transition temperature when a certain amount of pressure is applied, and the symmetry becomes from tetragonal to monoclinic. When the system is in monoclinic symmetry, the Bi $6p_x$ and $6p_y$ orbitals are no longer equivalent. Therefore, once one of the Bi $6p_{x/y}$ orbitals lowers the energy (possibly a sort of band Jahn-Teller effect), the system is in energetically more stable states and shows the higher transition temperature. This fact indicates the system has the orbital instability in Bi $6p_{x/y}$, and this instability is clearly related to the superconducting transition temperature; orbital fluctuation may impede the superconducting state.

In summary, we have revealed that the orbital instability plays important role in the layered chalcogenide superconductors $FeSe_{0.4}Te_{0.6}$ and BiS_2-based materials.

PUBLICATIONS AND AWARDS

List of publications

1. *Electronic phase separation in $EuFBiS_2$*
   T. Sugimoto, E. Paris, A. Barinov, V. Kandyba, J. Kajitani, R. Higashinaka, T. D. Matsuda, Y. Aoki, N. L. Saini, and T. Mizokawa
   to be submitted.

2. *Coexistence of semiconducting and mechanical-induced metallic phases in $CeOBiS_2$ revealed by space-resolved photoemission spectroscopy*
   T. Sugimoto, E. Paris, A. Barinov, V. Kandyba, R. Higashinaka, T. D. Matsuda, Y. Aoki, N. L. Saini, and T. Mizokawa
   to be submitted.

3. *Orbital states and spin-orbit interaction in $FeSe_{0.4}Te_{0.6}$ revealed by angle-resolved photoemission spectroscopy and first-princiles calculation*
   T. Sugimoto, E. F. Schwier, H. Iwasawa, K. Shimada, T. Noji, Y. Koike, N. L. Saini, and T. Mizokawa
   to be submitted.

4. *Orbital-dependent band renormalization in $BaNi_2(As_{1-x}P_x)_2$ ($x = 0.00$ and 0.092)*
   T. Noda, K. Kudo, M. Takasuga, M. Nohara, T. Sugimoto, D. Ootsuki, M. Kobayashi, K. Horiba, K. Ono, H. Kumigashira, A. Fujimori, N. L. Saini, T Mizokawa,
   submitted to Journal of the Phyiscal Society of Japan.

5. *Electronic structure of self-doped layered $Eu_3F_4Bi_2S_4$ material revealed by x-ray absorption spectroscopy and photoelectron spectromicroscopy*
   E. Paris, T. Sugimoto, T. Wakita, A. Barinov, K. Terashima, V. Kandyba, O. Proux, J. Kajitani, R. Higashinaka, T. D. Matsuda, Y. Aoki, T. Yokoya, T. Mizokawa, and N. L. Saini
   Physical Review B **95**, 035152 (2017).

6. *Localized and mixed valence state of Ce $4f$ in superconducting and ferromagnetic $CeO_{1-x}F_xBiS_2$ revealed by x-ray absorption and photoemission spectroscopy*
   T. Sugimoto, D. Ootsuki, E. Paris, A. Iadecola, M. Salome, E. F. Schwier, H. Iwasawa, K. Shimada, T. Asano, R. Higashinaka, T. D. Matsuda, Y. Aoki, N. L. Saini, and T. Mizokawa
   Physical Review B **94**, 081106(R) (2016).

7. *The effect of RE substitution in layered $REO_{0.5}F_{0.5}BiS_2$: chemical pressure, local disorder and superconductivity*
   Y. Mizuguchi, E. Paris, T. Sugimoto, A. Iadecola, J. Kajitani, O. Miura, T. Mizokawa, N. L. Saini
   Physical Chemsitry Chemical Physics **17**, 22090 (2015).

8. *Electronic structure of $Li_{1+x}[Mn_{0.5}Ni_{0.5}]_{1-x}O_2$ studied by photoemission and x-ray absorption spectroscopy*
   Y. Yokoyama, D. Ootsuki, T. Sugimoto, H. Wadati, J. Okabayashi, X. Yang, F. Du, G. Chen, and T. Mizokawa
   Applied Physical Letters **107**, 033903 (2015).

9. *Fermi surfaces and orbital polarization in superconducting $CeO_{0.5}F_{0.5}BiS_2$ revealed by angle-resolved photoemission spectroscopy*
   T. Sugimoto, D. Ootsuki, C. Morice, E. Artacho, S. S. Saxena, E. F. Schwier, M. Zheng, Y. Kojima, H. Iwasawa, K. Shimada, M. Arita, H. Namatame, M. Taniguchi, M. Takahashi, N. L. Saini, T. Asano, R. Higashinaka, T. D. Matsuda, Y. Aoki, and T. Mizokawa
   Physical Review B **92**, 041113(R) (2015).

10. *Andersons impurity-model analysis on $CeO_{1-x}F_xBiS_2$*
    T. Sugimoto, B. Joseph, E. Paris, A. Iadecola, S. Demura, Y. Mizuguchi, Y. Takano,T. Mizokawa, and Naurang L. Saini
    Jounal of Physics: Proceeding Series **592**, 012073 (2015).

11. *Determination of local atomic displacements in $CeO_{1-x}F_xBiS_2$ system*
    E. Paris, B. Joseph, A. Iadecola, T. Sugimoto, L. Olivi, S. Demura, Y. Mizuguchi, Y. Takano, T. Mizokawa, and N. L. Saini
    Journal of Physics: Condensed Matter **26**, 435701 (2014).

12. *Role of the Ce valence in the coexistence of superconductivity and ferromagnetism of $CeO_{1-x}F_xBiS_2$ revealed by Ce L_3-edge x-ray absorption spectroscopy*
    T. Sugimoto, B. Joseph, E. Paris, A. Iadecola, T. Mizokawa, S. Demura, Y. Mizuguchi, Y. Takano, and N. L. Saini
    Physical Review B **89**, 201117(R) (2014).

13. *Important Roles of Te 5p and Ir 5d SpinOrbit Interactions on the Multi-band Electronic Structure of Triangular Lattice Superconductor* $Ir_{1-x}Pt_xTe_2$
D. Ootsuki, T. Toriyama, M. Kobayashi, S. Pyon, K. Kudo, M. Nohara, T. Sugimoto, T. Yoshida, M. Horio, A. Fujimori, M. Arita, H. Anzai, H. Namatame, M. Taniguchi, N. L. Saini, T. Konishi, Y. Ohta, and T. Mizokawa
Journal of the Physical Society of Japan **83**, 033704 (2014).

14. *Te 5p orbitals bring three-dimensional electronic structure to two-dimensional* $Ir_{0.95}Pt_{0.05}Te_2$
D. Ootsuki, T. Toriyama, S. Pyon, K. Kudo, M. Nohara, K. Horiba, M. Kobayashi, K. Ono, H. Kumigashira, T. Noda, T. Sugimoto, A. Fujimori, N. L. Saini, T. Konishi, Y. Ohta, and T. Mizokawa
Physical Review B **89**, 104506 (2014).

15. *Electronic Structure of Quantum Spin-liquid Coupound* $Ba_3CuSb_2O_9$
T. Sugimoto,T. Mizokawa, H. Wadati, K. Takubo, A. Damascelli, T. Z. Regier, G. A. Sawatzky, N Katayama, H. Sawa, K. Kimura, and S. Nakatsuji
JPS Conference Proceedings **3**, 014007 (2014).

16. *X-ray Photoemission and X-ray Absorption Spectroscopy of Hexagonal* $Ba_3CuSb_2O_9$
T. Sugimoto,T. Mizokawa, H. Wadati, K. Takubo, A. Damascelli, T. Z. Regier, G. A. Sawatzky, N Katayama, H. Sawa, K. Kimura, and S. Nakatsuji
JPS Conference Proceedings **1**, 012122 (2014).

17. *Impact of local lattice disorder on spin and orbital orders in* $Ca_{2-x}Sr_xRuO_4$
T. Sugimoto, D. Ootsuki, and T. Mizokawa
Journal of the Physical Society of Japan **82**, 104714 (2013).

Awards

1. Best Presentation Award
Role of the local structure and electronic states in superconductivity of BiS_2*-based materials*,
T. Sugimoto
Symposium X, European Material Research Society Fall meeting 2016, Politechnika Warszawska, Warsaw, Poland.

REFERENCES

[1] A. W. Wilson, Proc. Roy. Soc. A **133**, 458 (1931).

[2] F. Bloch, Z. Phys **52**, 555 (1986).

[3] J. H. de Boer and E. J. W. Verway, Proc. Roy. Soc. London, Sect. A **42**, 59 (1937).

[4] H. K. Onnes, Commun. Leiden **12**, 120 (1911).

[5] J. Bardeen, L. N. Cooper, and J. R. Schrieffer, Phys. Rev. **108**, 1175 (1957).

[6] N. F. Mott, Proc. Roy. Soc. **62**, 416 (1986).

[7] J. Hubbard, Proc. Roy. Soc. **277**, 277 (1964).

[8] P. W. Anderson, Phys. Rev. **115**, 2 (1959).

[9] P. W. Anderson, Solid State Physics **14**, 99 (1963).

[10] J. G. Bednorz and K. A. Müller, Z. Phys. B **64**, 189 (1986).

[11] P. W. Anderson, Science **235**, 1196 (1987).

[12] T. Moriya, Y. Takahashi, and K. Ueda, J. Phys. Soc. Jpn. **59**, 2905 (1990).

[13] P. Monthoux, A. V. Balatsky, and D. Pines, Phys. Rev. Lett. **67**, 3448 (1991).

[14] F. C. Zhang and T. M. Rice, Phys. Rev. B **37**, 3759 (1988).

[15] M. Ogata and H. Fukuyama, Rep. Prog. Phys. **71**, 036501 (2008).

[16] Y. Kamihara, T. Watanabe, M. Hirano, and H. Hosono, J. Am. Chem. Soc. **130**, 3296 (2008).

[17] C. Wang, L. Li, S. Chi, Z. Zhu, Z. Ren, Y. Li, Y. Wang, X. Lin, Y. Luo, S. Jiang, X. Xu, G. Cao, and Z. Xu, Europhys. Lett. **83**, 67006 (2008).

[18] J.-F. Ge, Z.-L. Liu, C. Liu, C.-L. Gao, D. Qian, Q.-K. Xue, Y. Liu, and J.-F. Jia, Nature Materials **14**, 285 (2014).

[19] Y. Mizuguchi, H. Fujihisa, Y. Gotoh, K. Suzuki, H. Usui, K. Kuroki, S. Demura, Y. Takano, H. Izawa, and O. Miura, Phys. Rev. B **86**, 220510 (2012).

[20] Y. Mizuguchi, S. Demura, K. Deguchi, Y. Takano, H. Fujihisa, Y. Gotoh, H. Izawa, and O. Miura, J. Phys. Soc. Jpn. **81**, 114725 (2012).

[21] K. Kugel and D. I. Khomskii, Zh. Eksp. Teor. Fiz. **15**, 1492 (1973).

[22] R. M. Fernandes, A. V. Chubukov, and J. Schmalian, Nature Physics **10**, 97 (2014).

[23] J. Bardeen, Rev. Mod. Phys. **23**, 261 (1951).

[24] P. A. M. Dirac, Roy. Soc. Proc. A **117**, 610 (1928).

[25] P. A. M. Dirac, Roy. Soc. Proc. A **126**, 360 (1930).

[26] L. Fu, C. L. Kane, and E. J. Mele, Phys. Rev. Lett. **98**, 106803 (2007).

[27] L. Fu and C. L. Kane, Phys. Rev. B **76**, 045302 (2007).

[28] J. E. Moore, and L. Balents, Phys. Rev. B **75**, 121306(R) (2007).

[29] S. Pyon, K. Kudo, and M. Nohara, J. Phys. Soc. Jpn. **81**, 053701(2012).

[30] J. J. Yang, Y. J. Choi, Y. S. Oh, A. Hogan, Y. Horibe, K. Kim, B. I. Min, and S.-W. Cheong, Phys. Rev. Lett. **108**, 116402 (2012).

[31] S. Nakatsuji and Y. Maeno, Phys. Rev. Lett. **84**, 2666 2000Ł.

[32] W. A. Harrison, *Electronic Stucture and Physical Properties of Solids* (Freeman, San Fransisco, 1980).

[33] J. Kanamori, Prog. Theoret. Phys. **30**, 275 (1963).

[34] T. Mizokawa and A. Fujimori, Phys. Rev. B **54**, (1996) 5368.

[35] J. Kondo, Prog. Theoret. Phys. **28**, 846 (1962).

[36] J. Kondo, Prog. Theoret. Phys. **32**, 37 (1964).

[37] J. Kondo, Prog. Theoret. Phys. **28**, 34 (1965).

[38] P. W. Anderson, Phys. Rev. **124**, 41 (1961).

[39] J. R. Schreffer and P. A. Wolff, Phys. Rev. **144**, 491 (1966).

[40] P. Horhenberg and W. Kohn, Phys. Rev. B **136**, 864 (1964).

[41] L. H. Thomas, Proc. Cambridge Phil. Soc. **23**, 542 (1927).

[42] E. Fermi, Z. Physik **48**, 73 (1928).

[43] W. Kohn and L. Sham, Phys. Rev. **140**, A1133 (1965).

[44] J. F. Janak, Phys. Rev. B **18**, 7165 (1978).

[45] A. Einstein, Ann. Phys. (Leipzig) **17**, 132 (1905).

[46] S. Hüfner, *Photoelectron Spectroscopy* (Springer, Berlin, 2003) third ed.

[47] T. A. Koopmans, Physica **1**, 104 (1933).

[48] for instance, R. D. Mattuck, *A Guide to Feynman Diagrams in the Many-Body Problem* (McGraw-Hill, New York, 1974) second ed.

[49] J. M. Luttinger and J. C. Ward, Phys. Rev. **118**, 1417 (1960).

[50] J. M. Luttinger, Phys. Rev. **119**, 1153 (1960).

[51] U. Fano, Nuovo Cim **12**, 154 (1935).

[52] U. Fano, Phys. Rev. **124**, 1866 (1961).

[53] M. P. Seah and W. A. Dench, Surf. Int. Anal. **1**, 2 (1979).

[54] R. Nakajima, J. Stöhr, and Y. U. Idzerda, Phys, Rev. B **59**, 6421 (1999).

[55] A. Thompson, D. Attwood, E. Gullikson, M. Howells, K.-J. Kim, J. Kirz, J. Kortright, I. Lindau, P. Pianetta, A. Robinson, J. Scofield, J. Underwood, D. Vaughan, G. Williams, and H. Winick, *X-ray Data Booklet* (Lawrence Berkeley National Laboratory, 2001) second ed.

[56] L. Tröger, D. Arvanitis, K. Baberschke, H. Michaelis, U. Grimm, and E. Zschech, Phys. Rev. B **46**, 3283 (1992).

[57] Website of Photon Factory (http://pfwww.kek.jp/users_info/station_spec/bl28/bl28a.html).

[58] Website of HiSOR (http://www.hsrc.hiroshima-u.ac.jp/english/bl1.htm and http://www.hsrc.hiroshima-u.ac.jp/english/bl9.htm).

[59] Website of Elettra (https://www.elettra.trieste.it/lightsources/elettra/elettra-beamlines/xafs/specifications/page-2.html?showall=).

[60] P. Dudin, P. Lacovig, C. Fava, E. Nicolini, A. Bianco, G. Cautero and A. Barinov, J. Synchrotron Rad. **17**, 445 (2010).

[61] Website of ESRF (http://www.esrf.eu).

[62] F. C. Hsu, J. Y. Luo, K. W. The, T. K. Chen, T. W. Huang, P. M. Wu, Y. C., Lee, Y. L. Huang, Y. Y. Chu, D. C. Yan, M. K. Wu, Proc. Natl. Acad. Sci. U.S.A. **105**, 14262 (2008).

[63] T. M. McQueen, A. J. Williams, P. W. Stephens, J. Tao, Y. Zhu, V. Ksenofontov, F. Casper, C. Felser, and R. J. Cava, Phys. Rev. Lett. **103**, 057002 (2009).

[64] H. Kontani and S. Onari, Phys. Rev. Lett. **104**, 157001 (2010).

[65] S. Onari and H. Kontani, Phys. Rev. Lett. **109**, 137001 (2012).

[66] T. Noji, T. Suzuki, H. Abe, T. Adachi, M. Kato, Y. Koike, J. Phys.Soc. Jpn. **79**, 084711 (2010).

[67] S-H. Baek, D. V. Efremov, J. M. Ok, J. S. Kim, Jeroen van den Brink, and B. Büchner, Nature Mater. doi:10.1038/nmat4138 (2014).

[68] K. Nakayama, Y. Miyata, G. N. Phan, T. Sato, Y. Tanabe, T. Urata, K. Tanigaki, and T. Takahashi, Phys. Rev. Lett. **113**, 237001 (2014).

[69] T. Shimojima, Y. Suzuki, T. Sonobe, A. Nakamura, M. Sakano, J. Omachi, K. Yoshioka, M. Kuwata-Gonokami, K. Ono, H. Kumigashira, A. E. Böhmer, F. Hardy, T. Wolf, C. Meingast, H. v. Löhneysen, H. Ikeda, and K. Ishizaka, Phys. Rev. B **90**, 121111 (2014).

[70] J. Maletz, V. B. Zabolotnyy, D. V. Evtushinsky, S. Thirupathaiah, A. U. B. Wolter, L. Harnagea, A. N.Yaresko, A. N. Vasiliev, D. A. Chareev, A. E. Böhmer, F. Hardy, T. Wolf, C. Meingast, E. D. L. Rienks, B. Büchner, and S. V. Borisenko, Phys. Rev. B **89**, 220506(R) (2014).

[71] J-F. Ge, Z-L. Liu, C. Liu, C-L. Gao, D. Qian, Q-K. Xue, Y. Liu, and J-F. Jia, Nature Mater. **14**, 285 (2015).

[72] J. J. Lee, F. T. Schmitt, R. G. Moore, S. Johnston, Y.-T. Cui, W. Li, M. Yi, Z. K. Liu, M. Hashimoto, Y. Zhang, D. H. Lu, T. P. Devereaux, D.-H. Lee, and Z.-X. Shen, Nature **515**, 245 (2014).

[73] A. Subedi, L. Zhang, D. Singh, and M. Du, Phys. Rev. B **78**, 134514 (2008).

[74] F. Chen, B. Zhou, Y. Zhang, J. Wei, H. W. Ou, J. F. Zhao, C. He, Q. Q. Ge, M. Arita, K. Shimada, H. Namatame, M. Taniguchi, Z. Y. Lu, J. P. Hu, X. Y. Cui, and D. L. Feng, Phys. Rev. B **81**, 014526 (2010).

[75] K. Nakayama, T. Sato, P. Richard, T. Kawahara, Y. Sekiba, T. Qian, G. F. Chen, J. L. Luo, N. L. Wang, H. Ding, T. Takahashi, Phys. Rev. Lett. **105**, 197001 (2010).

[76] T. Sudayama, D. Ootsuki, Y. Wakisaka, T. Mizokawa, N. L. Saini, M. Arita, H. Namatame, M. Taniguchi, T. Noji, and Y. Koike, J. Phys. Soc. Jpn. **82**, 053705 (2013).

[77] A. Tamai, A. Y. Ganin, E. Rozbicki, J. Bacsa, W. Meevasana, P. D. C. King, M. Caffio, R. Schaub, S. Margadonna, K. Prassides, M. J. Rosseinsky, F. Baumberger, Phys. Rev. Lett. **104**, 097002 (2010).

[78] K. Okazaki, Y. Ito, Y. Ota, Y. Kotani, T. Shimojima, T. Kiss, S. Watanabe, C.-T. Chen, S. Niitaka, T. Hanaguri, H. Takagi, A. Chainani, and S. Shin, Sci. Rep. **4**, 4109 (2013).

[79] P. D. Johnson, H. B. Yang, J. D. Rameau, G. D. Gu, Z. H. Pan, T. Valla, M. Weinert, and A. V. Fedorov, Phys. Rev. Lett. **114**, 167001 (2015).

[80] S. Kasahara, H. J. Shi, K. Hashimoto, S. Tonegawa, Y. Mizukami, T. Shibauchi, K. Sugimoto, T. Fukuda, T. Terashima, and A. H. Nevidomskyy, and Y. Matsuda, Nature **486**, 382 (2012).

[81] H. Miao, L.-M. Wang, P. Richard, S.-F. Wu, J. Ma, T. Qian, L.-Y. Xing, X.-C. Wang, C.-Q. Jin, C.-P. Chou, Z. Wang, W. Ku, and H. Ding, Phys. Rev. B **89**, 220503(R) (2014).

[82] P. Giannozzi et al., J. Phys.:Condens. Matter **21**, 395502 (2009).

[83] K. Okazaki, Y. Ito, Y. Ota, Y. Kotani, T. Shimojima, T. Kiss, S. Watanabe, C.-T. Chen, S. Niitaka, T. Hanaguri, H. Takagi, A. Chainani, and S. Shin, Phys. Rev. Lett. **109**, 237011 (2012).

[84] H. Usui, K. Suzuki, and K. Kuroki, Phys. Rev. B **86**, 220501(R) (2012).

[85] T. Yildirim, Phys. Rev. B **87**, 020506(R) (2013).

[86] G. B. Martins, A. Moreo, and E. Dagotto, Phys. Rev. B **87**, 081102(R) (2013).

[87] A. Miura, M. Nagao, T. Takei, S. Watauchi, Y. Mizuguchi, Y. Takano, I. Tanaka, and N. Kumada, Cryst. Growth Des. **15**, 39 (2015) and its correction by Miura *et al.*, Cryst. Growth Des. **16**, 2459 (2016).

[88] M. Nagao, A. Miura, S. Demura, K. Deguchi, S. Watauchi, T. Takei, Y. Takano, N. Kumada, and I. Tanaka, Solid State Commun. **178**, 33 (2014).

[89] L. K. Zeng, X. B. Wang, J. Ma, P. Richard, S. M. Nie, H. M. Weng, N. L. Wang, Z. Wang, T. Qian, and H. Ding, Phys. Rev. B **90**, 054512 (2014).

[90] Z. R. Ye, H. F. Yang, D. W. Shen, J. Jiang, X. H. Niu, D. L. Feng, Y. P. Du, X. G. Wan, J. Z. Liu, X. Y. Zhu, H. H. Wen, and M. H. Jiang, Phys. Rev. B **90**, 045116 (2014).

[91] S. Demura, K. Deguchi, Y. Mizuguchi, K. Sato, R. Honjyo, A. Yamashita, T. Yamaki, H. Hara, T. Watanabe, S. J. Denholme, M. Fujioka, H. Okazaki, T. Ozaki, O. Miura, T. Yamaguchi, H. Takeya, and Y. Takano, J. Phys. Soc. Jpn. **84**, 024709 (2015).

[92] H.-F. Zhai, Z.-T. Tang, H. Jiang, K. Xu, K. Zhang, P. Zhang, J.-K. Bao, Y.-L. Sun, W.-H. Jiao, I. Nowik, I. Felner, Y.-K. Li, X.-F. Xu, Q. Tao, C.-M. Feng, Z.-A. Xu, and G.-H. Cao, Phys. Rev. B **90**, 064518 (2014).

[93] R. Higashinaka, T. Asano, T. Nakashima, K. Fushiya, Y. Mizuguchi, O. Miura, T. D. Matsuda, and Y. Aoki, J. Phys. Soc. Jpn. **84**, 023702 (2015).

[94] A. Bianconi, M. Dell'Ariccia, A. Gargano and C.R. Natoli in EXAFS and Near Edge Structure, Editors. A. Bianconi, L. Incoccia, S. Stipcich, Springer-Verlag (Berlin, 1983) pp. 57; A. Bianconi, E. Fritsch, G. Calas, and J. Petiau, Phys. Rev. B **32**, 4292 (1985).

[95] B. T. Thole, G. van der Laan, J. C. Fuggle, G. A. Sawatzky, R. C. Karnatak, and J. -M. Esteva, Phys. Rev. B **32**, 5107 (1985).

[96] H. Matsuyama, I. Harada, and A. Kotani, J. Phys. Soc. Jpn. **66**, 337 (1997).

[97] A. Kotani, K. O. Kvashnina, P. Glatzel, J. C. Parlebas, and G. Schmerber, Phys. Rev. Lett. **108**, 036403 (2012).

[98] T. Kroll, F Roth, A. Koitzsch, R. Kraus, D. R. Batchelor, J. Werner, G. Behr, B. Büchner and M. Knupfer, New Journal of Physics **11**, 025019 (2009).

[99] F. Bondino, E. Magnano, C. H. Booth, F. Offi, G. Panaccione, M. Malvestuto, G. Paolicelli, L. Simonelli, F. Parmigiani, M. A. McGuire, A. S. Sefat, B. C. Sales, R. Jin, P. Vilmercati, D. Mandrus, D. J. Singh, and N. Mannella, Phys. Rev. B **82**, 014529 (2010).

[100] E. Paris, B. Joseph, A. Iadecola, T. Sugimoto, L. Olivi, S. Demura, Y. Mizuguchi, Y. Takano, T. Mizokawa, and N. L. Saini, J. Phys.: Condens. Matter **26**, 435701 (2014).

[101] H. J. Van Daal and K. H. J. Buschow: Phys. Lett. A **31**, 103 (1970).

[102] R. Takke, N. Dolezal, W. Assmus, and B. Lüthi: J. Magn. Magn. Mater. **23**, 247 (1981).

[103] S. K. Dhar, S. K. Malik, and R. Vijayaraghavan: J. Phys. C **14**, L321 (1981).

[104] M. Jerjini, M. Bonnet, P. Burlet, G. Lapertot, J. Rossat-Mignod, J. Y. Henry, and D. Gignoux: J. Magn. Magn. Mater. **76**&**77**, 405 (1988).

[105] K. Abe, J. Kitagawa, N. Takeda, and M. Ishikawa: Phys. Rev. Lett. **83**, 5366 (1999).

[106] S. Raymond, P. Haen, R. Calemczuk, S. Kambe, B. Fk, P. Lejay, T. Fukuhara, and J. Flouquet: J. Phys.: Condens. Matter **11**, 5547 (1999).

[107] P. Manfrinetti, S. Dhar, R. Kulkarni, and A. Morozkin, Solid State Commun. **135**, 444 (2005).

[108] O. Gunnarsson and K. Schönhammer, Phys. Rev. Lett. **50**, 604 (1983).

[109] C. Morice, E. Artacho, S. E. Dutton, H.-J. Kim, and S. S. Saxena, J. Phys.: Condens. Matter **28**, 345504 (2016).

[110] K. Okada and A. Kotani, J. Phys. Soc. Jpn. **58**, 2578 (1989).

[111] A. E. Bocquet, T. Mizokawa, T. Saitoh, H. Namatame, and A. Fujimori, Phys. Rev. B **46**, 3771 (1992).

[112] V. V. Krishnamurthy, J. C. Lang, D. Haskel, D. J. Keavney, G. Srajer, J. L. Robertson, B. C. Sales, D. G. Mandrus, D. J. Singh, and D. I. Bilc, Phys. Rev. Lett. **98**, 126403 (2007).

[113] V. V. Krishnamurthy, D. J. Keavney, D. Haskel, J. C. Lang, G. Srajer, B. C. Sales, D. G. Mandrus, and J. L. Robertson, Phys. Rev. B **79**, 014426 (2009).

[114] K. Matsubayashi, K. Munakata, M. Isobe, N. Katayama, K. Ohgushi, Y. Ueda, N. Kawamura, M. Mizumaki, N. Ishimatsu, M. Hedo, I. Umehara, and Y. Uwatoko, Phys. Rev. B **84**, 024502 (2011).

[115] M. O. Krause and J. H. Oliver, J. Phys. Chem. Ref. Data **8**, 329 (1979).

[116] W. D. Schneider, C. Laubschat, G. Kalkowski, J. Haase, and A. Puschmann, Phys. Rev. B **28**, 2017 (1983).

[117] M. Fernández-Perea, M. Vidal-Dasilva, J. A. Aznárez, J. I. Larruquert, J. A. Méndez, L. Poletto, D. Garoli, A. M. Malvezzi, A. Giglia, and S. Nannarone, J. Appl. Phys. **104**, 123527 (2008).

[118] T. Yakita, K. Terashima, and N. L. Saini, private communications.

[119] A. Athauda, J. Yang, S. Lee, Y. Mizuguchi, K. Deguchi, Y. Takano, O. Miura, and D. Louca, Phys. Rev. B **91**, 144112 (2015).

[120] Q. Liu, X. Zhang, and A. Zunger, Phys. Rev. B **93**, 174119 (2016).

[121] X. Zhou, Q. Liu, J. A. Waugh, H. Li, T. Nummy, X. Zhang, X. Zhu, G. Cao, A. Zunger, D. S. Dessau, arXiv:1607.02796

[122] E. Paris and N. L. Saini, private communications.

[123] Y. Mizuguchi, E. Paris, T. Sugimoto, A. Iadecola, J. Kajitani, O. Miura, T. Mizokawa, and N. L. Saini, Phys. Chem. Chem. Phys. **17**, 1 (2015).

[124] M. Nagao, A. Miura, I. Ueta, S. Watauchi, and I. Tanaka, Solid State Commun. **245**, 11 (2016).

[125] T. Machida, Y. Fujisawa, M. Nagao, S. Demura, K. Deguchi, Y. Mizuguchi, Y. Takano, and H. Sakata, J. Phys. Soc. Jpn. **83**, 113701 (2014).

[126] H. Usui and K. Kuroki, private communications.

[127] K. Kuroki, S. Onari, R. Arita, H. Usui, Y. Tanaka, H. Kontani, and H. Aoki, Phys. Rev. Lett. **101**, 087004 (2008).